Master's thesis

NTNU
Norwegian University of Science and Technology
Faculty of Natural Sciences
Department of Materials Science and Engineering

Tuva Jevnaker Bjaanes

Application of Graphene and Graphene Oxide as Antifouling Agents in Epoxy-Based Coatings

Master's thesis in Chemical Engineering and Biotechnology
Supervisor: Hilde Lea Lein
Co-supervisor: Ingrid Hallsteinsen, Michael Robert Kelly and Anh Hoang Dam

June 2022

NTNU
Norwegian University of Science and Technology

Tuva Jevnaker Bjaanes

Application of Graphene and Graphene Oxide as Antifouling Agents in Epoxy-Based Coatings

Master's thesis in Chemical Engineering and Biotechnology
Supervisor: Hilde Lea Lein
Co-supervisor: Ingrid Hallsteinsen, Michael Robert Kelly and Anh Hoang Dam
June 2022

Norwegian University of Science and Technology
Faculty of Natural Sciences
Department of Materials Science and Engineering

NTNU
Norwegian University of
Science and Technology

Preface

This master's thesis was written by Tuva Jevnaker Bjaanes and submitted in the course "TMT4900 Materials Chemistry and Energy Technology, Master's thesis" in spring 2022. The thesis was a part of the final assessment of the master's degree program in Chemical Engineering and Biotechnology at the Norwegian University of Science and Technology (NTNU).

The work of this master's thesis was carried out from January 2022 to June 2022 at NTNU Gløshaugen campus, Trondheim. Supervision was given by Professor Hilde Lea Lein as head supervisor, with additional support from my co-supervisors, Associate Professor Ingrid Hallsteinsen and Ph.D. candidate Michael Robert Kelly from NTNU and Senior Material Chemist Anh Hoang Dam from CealTech AS. Kjell Inge Reitan from NTNU Sealab and the Functional Materials and Materials Chemistry (FACET) research group at NTNU have also supported my thesis. The experimental work was conducted by the author and carried out at the Department of Material Science and Technology, NTNU Nanolab, Department of Mechanical and Industrial Engineering, Department of Physics, and Department of Chemical Engineering.

CealTech AS delivered graphene dispersion, graphene oxide paste and epoxy resin (Epikote 828) with the support of Anh Hoang Dam. Algae culture and naturally filtered seawater were provided by NTNU Sealab with the support of Kjell Inge Reitan.

Trondheim, 12/06/2022
Tuva J. Bjaanes

Acknowledgement

The work of this master's thesis would not have been possible without the great support of my supervisors, fellow students, friends, and family. My supervisor Hilde Lea Lein deserves special thanks for always bringing engagement to my work and for sharing valuable insight and knowledge. The guidance from my co-supervisors Ingrid Hallsteinsen and Michael Robert Kelly has also been highly appreciated. Our weekly meetings have given me inspiration and encouraged new ideas. I would also like to express my gratitude to the professors, Ph.D. candidates, and the master's students of the FACET group for giving me constructive feedback throughout the semester.

The technical staff at NTNU deserves attention for their continuous guidance and help during the semester. Thanks to Senior Engineer Anita Storsve for always being available and for helping me with issues in the lab. I also want to thank Senior Engineer Johannes Ofstad and Senior Engineer Astrid Bjørkøy for sharing your expertise, and for providing me with essential instrument training. Senior Engineer Cristian Rodriguez deserves special thanks for patiently helping and guiding me in the Nanomechanical lab.

Finally, I want to thank family, friends, and fellow students for your unlimited support and for always sharing encouraging words.

Thank you all!

Abstract

Biofouling defines the undesired accumulation of marine biological matter, like diatoms and bacteria, onto submerged surfaces. Marine industries have traditionally fought biofouling through the application of coatings with antifouling agents. The main challenge with today's commercial antifouling coatings is the use of toxic compounds, such as cuprous oxide, that target innocent species and promote environmental issues. Graphene materials have shown promising antifouling properties with low toxicity to non-target species, making them an appealing alternative to conventional agents. In addition, graphene (G) and graphene oxide (GO) have been proven to increase mechanical performance of coatings.

The main objective of this master's thesis was to develop epoxy-based coatings with well-dispersed G and GO nanoparticles, to investigate their antifouling and mechanical properties suitable for marine applications. Surface characteristics relevant for antifouling performance, including sheet distribution, wetting properties and surface roughness, were considered with respect to G and GO content. The coating performance was evaluated by nanoindentation measurements, to estimate coating's hardness, Young's modulus and scratch resistance. Furthermore, the growth inhibitory properties of G and GO were assessed by measuring algae growth on coatings after two weeks of submersion in seawater. The first experiment utilized a mixed algae culture to simulate a realistic marine environment. The second experiment used an algae culture of a single fouling specie to make the subsequent characterization easier.

The sol-gel process was used to make epoxy nanocomposite coatings with evenly distributed G and GO sheets. Stable G slurries were achieved presumably as a result of electrostatic stabilization. GO slurries experienced sedimentation after one week, but easy re-dispersion of GO sheets appeared due to repulsion forces from their surface functional groups. An enhanced hardness and elastic behavior appeared for GO coatings compared to G coatings. Most likely, the large basal planes and oxygenated functional groups of GO sheets ensured mechanical interlocking and chemical coupling within the epoxy network, facilitating stress transfers and an increasing cross-linked density.

The antifouling assessment indicated that G and GO coatings had less marine growth compared to pure epoxy coatings, with no consistent trend with increasing G and GO content. G coatings expressed the strongest antifouling behavior, with 50% less fouling compared to pure epoxy coatings. Preliminary measures of surface characteristics, relevant to antifouling performance, did not substantiate the observed antifouling behavior of G and GO coatings. Indeed, oxidative stress was believed to be the dominant antifouling mechanism. In future research, it would be beneficial to examine larger areas of the samples to reduce measurement uncertainty. Performing biofilm thickness measurement by staining the marine growth, with e.g. crystal violet, could extend the understanding of the antifouling performance of G and GO.

Sammendrag

Biologisk begroing definerer uønsket vekst av marine organismer, bl.a. kiselalger, på overflaten av marine konstruksjoner. Maritim industri har tradisjonelt sett bekjempet begroing ved belegg som inneholder tilsetningsstoffer med gro-hindrende egenskaper, kalt bunnstoff. Problemet med kommersielle bunnstoff er bruk av stoffer som er skadelige mot miljøet og ikke-groende arter, f.eks. kobberoksid. Grafen (G) og Grafen Oksid (GO) er ansett som interessante erstatninger, med lovende gro-hindrende egenskaper og lav toksisitet mot ikke-groende arter, og med mulighet til å forbedre mekaniske egenskaper til epoxy-baserte belegg.

Det overordnede målet i denne masteroppgaven har vært å produsere epoxy-baserte belegg med tilsetning av G og GO, for å undersøke gro-hindrende og mekaniske egenskaper egnet for marine anvendelser. Overflateegenskaper relevant for gro-hindrende ytelse som partikkelfordeling, kontaktvinkel, overflateenergi og ruhet ble vurdert med hensyn til G- og GO-innhold. Mekanisk ytelse ble evaluert ved nanoindentasjonsmålinger, ved å måle beleggenes hardhet, Youngs modul og ripemotstand. Videre ble den gro-hindrende oppførselen til G og GO undersøkt ved å kvantifisere algevekst på beleggenes overflate etter to ukers nedsenkning i maritimt miljø. Dette eksperimentet ble utført to ganger, ved bruk av en blandingskultur av marine organismer som representerte et realistisk maritimt miljø, og ved bruk av en algekultur av én begroingsart for enklere karakterisering.

Sol-gel metoden ble brukt til å fremstille epoxy-baserte belegg med jevnt fordelte G- og GO-flak. Stabile G-dispersjoner ble trolig oppnådd som resultat av elektrostatisk stabilisering. GO-dispersjoner viste tegn til sedimentering etter én uke, men enkel re-separering av GO-flak var mulig som følge av frastøtende krefter fra funksjonelle overflategrupper av GO. Store basalplan og funksjonelle grupper av GO sørget trolig for mekaniske sammenlåsninger og kjemiske bindinger i epoxy-nettverket, som tilførte spenningsoverføringer og økt tverrbunnethet. Som følger av dette, ble hardhet og elastisk oppførsel av GO-belegg forbedret sammenlignet med G-belegg.

Evalueringen av gro-hindrede egenskaper indikerte at G- og GO-belegg opplevde redusert begroing sammenlignet med rene epoxy-belegg, men det ble ikke funnet en konsistent trend i gro-hindrede egenskaper med økende G- og GO-innhold. G-belegg fremsto 50% mindre begrodd enn rene epoxy-belegg, og viste dermed best ytelse til å hindre begroing. Målte overflateegenskaper underbygget ikke den observerte oppførselen til G- og GO-belegg. Derfor ble den dominerende gro-hindrende mekanismen for G og GO antatt å være generering av oksidativt stress. Med hensyn til videre arbeid vil det være fordelaktig å undersøke større areal av prøvene for å minimere måleusikkerhet. Tykkelsen av den produserte biofilmen kan med fordel måles ved å farge microorganismer med f.eks. krystallfiolett for å videre underbygge den gro-hindrede oppførselen til G og GO.

List of abbreviations

AFM	Atomic Force Microscope
ATR	Attenuated Total Reflectance
CA	Contact Angle
CAH	Contact Angle Hysteresis
CCAP	Culture Collection of Algae and Protozoa
COF	Coefficient of Friction
CuO	Cuprous Oxide
CVD	Chemical Vapor Phase Deposition
DMF	N,N-dimethylformamide
DMSO	Dimethyl Sulfoxide
EDS	Energy-Dispersive Spectroscopy
EG	Exfoliated Graphene
EtOH	Ethanol
FACET	Functional Materials and Materials Chemistry
FTIR	Fourier-Transform Infrared Spectroscopy
G	Graphene
GM	Graphene Material
GO	Graphene Oxide
IMA	Department of Material Science and Engineering
IMO	International Maritime Organisation
IR	Infrared
LPE	Liquid-phase Exfoliation
MIC	Microbiologically Influenced Corrosion
MTP	Department of Mechanical and Industrial Engineering
NMP	N-Methyl-2-Pyrroline
NTNU	Norwegian University of Science and Technology
OWRK	Owens-Wendt-Rabel-Kaelble
PE	Poly-Ethylene
PPGBAE	Poly(Propylene Glycol) Bis(2-Aminopropyl Ether)

rGO	Reduced Graphene Oxide
rpm	rounds per minute
ROS	Reactive Oxygen Specie
SEM	Scanning Electron Microscopy
SFE	Surface Free Energy
TBT	Tributylin
TBTF	Tributyltin Fluoride
TBTO	Tributyltin Oxide
THF	Tetrahydrofuran
TPT	Triphenyltin
VdW	Van der Waals
VOC	Volatile Organic Compound

Table of Contents

1 Background

1.1 Motivation

The world oceans represent over 70% of the Earth's surface [1] and is considered a major contribution to the global economy [2]. Numerous industries rely on the many attributes of the oceans, including the shipping industry, the fish-farm industry, the petroleum industry, and the renewable energy industry [3, 4]. These industries are operating in harsh environments, exposing themselves to a range of challenges. The marine industry has for decades been suffering from the effects of biofouling. Within hours of submerging artificial constructions, the accumulation and growth of micro-organisms develop onto the exposed surfaces, encouraging further adhesion of macro-organisms [5]. Some consequences of biofouling concern the reduction of nutrition supply to fish in the fish-farm industry [6], increasing drag resistance of ships in the shipping industry [5], and corrosion on offshore constructions in the energy industry [7, 8]. These incidents will undeniably lead to great economic losses and environmental issues. Worldwide, the economic cost of biofouling in the marine industry is estimated to a value of one billion dollars annually [9].

Humankind has actively attempted to prevent biofouling for decades. The first evidence of antifouling is found in the histories of the Romans and Greeks, where documentation shows that copper and lead were used to protect wooden boats from biofouling [10, 11]. In more recent years, antifouling strategies have primarily been based on the use of coatings with antifouling properties, including coatings incorporated with biocides, self-polishing coatings, and foul release coatings [12]. Some industries have implemented the use of energy for antifouling purposes, including ultrasonic cleaning, pulsed laser irradiation, and ultraviolet light treatment [13, 14]. Traditionally, coatings containing tributyltin (TBT) biocides have efficiently fought biofouling. However, the additive raised an environmental concern when it revealed toxic behavior towards non-target marine organisms, for instance generating imposex on crustaceans [15]. The complete ban of TBT in 2008 [16] made it necessary to find environmentally friendly replacements. Today, copper-based coatings are applied as the main replacements for TBT coatings, but with lower efficiency towards antifouling [17]. Copper-based coatings were introduced as environmentally friendly coatings, being less harmful towards non-target species. However, heavy metal contamination of copper compounds has been observed in harbors and marinas, raising concerns regarding environmental issues [18].

An ideal antifouling coating should exhibit the following properties: high antifouling performance, harmless towards non-target organisms, optimal viscosity for easy application, high durability, resistance to damage, and fixable [17]. Researchers are continuously reaching to discover new additives optimal for this purpose. Graphene (G) and Graphene Oxide (GO)

are two substances that have shown promising antifouling behavior [19–21]. Studies indicate that the development of microbial films on submerged surfaces has been directly inhibited by G and GO, while simultaneously expressing low toxic behavior towards non-target marine species [22]. These substances have also been shown to enhance mechanical properties when dispersed in epoxy matrices [23, 24]. Hence, G and GO are propitious candidates for the development of sustainable antifouling coatings suitable for marine applications.

1.2 Aim of work

The aim of this master's thesis is to investigate the antifouling behavior of graphene (G) and graphene oxide (GO) in epoxy-based coatings suitable for marine applications. G and GO will be dispersed in epoxy slurries at different concentrations, from 0 - 0.500 wt%, followed by spray coating onto Poly-Ethylene (PE) and steel substrates. G and GO slurries will be prepared based on a G-Epikote dispersion (0.06 wt%) and a GO paste (10 wt% GO) supplied by CealTech AS. The chosen experimental procedures and characterization techniques are adapted from work conducted by the author in the previous specialization project [25].

The primary objective of this thesis is to develop a biofilm reactor experiment to quantify biofouling on the prepared coatings in the means of algae growth. The coatings will be submerged in bioreactors for two weeks, followed by visual inspection under an optical microscope. The effect of utilizing a mixed algae culture, from NTNU Sealab, as opposed to a clean algae culture of a single fouling species will be evaluated. To improve the accuracy of the data, two different techniques for quantifying algae growth will be developed. The antifouling properties of epoxy-based coatings containing G and GO will be evaluated with respect to pure epoxy coatings and uncoated PE substrates.

The secondary objective includes the evaluation of cured coating properties relevant to antifouling and marine applications. The influence of G and GO on the mechanical characteristics will be examined. Hardness, Young's modulus, and scratch resistance will be measured using a nanoindenter at MTP. Surface properties like wetting properties, surface free energy, and surface roughness have been demonstrated to influence the antifouling behavior of epoxy-based coatings. The aim will be to investigate these properties with respect to the G/GO weight ratio, to assess potential antifouling mechanisms.

The final objective of this thesis concerns an analysis of the epoxy sols and slurries. The aim is to prepare stable and well-dispersed G and GO slurries with appropriate solvents. Their stability and composition in terms of functional groups will be investigated with respect to time and G/GO weight ratio. The viscosities of the prepared sols and slurries will be evaluated with respect to the applied coating deposition technique.

2 Introduction

The following chapter will elaborate on the different aspects of marine antifouling. Biofouling will be addressed, followed by the subject of antifouling coatings, including conventional and emerging approaches. The phenomenon of using G and GO as antifouling agents will be elaborated on. Further, characteristics of coating dispersion, including stability and rheology properties, will be addressed to enlighten the importance of high-quality coatings. Subsequently, characteristics of cured coatings relevant for mechanical robustness and antifouling purposes will be presented. Eventually, the concept of investigating and determining the antifouling behavior of coatings will be introduced.

2.1 Marine biofouling

The undesired accumulation and growth of biological matter onto the surface of artificial submerged constructions in the ocean defines the concept of marine biofouling, from now on referred to as biofouling [5]. The sea is the home of over 4000 different organisms responsible for biofouling [26]. Any unprotected surface being submerged in seawater will be prone to fouling almost immediately after immersion. Layers of foulants will develop, leading to immense economical and environmental consequences for marine industries. An example of biofouling is shown in Figure 2.1, showing biofouling on the propeller of a boat.

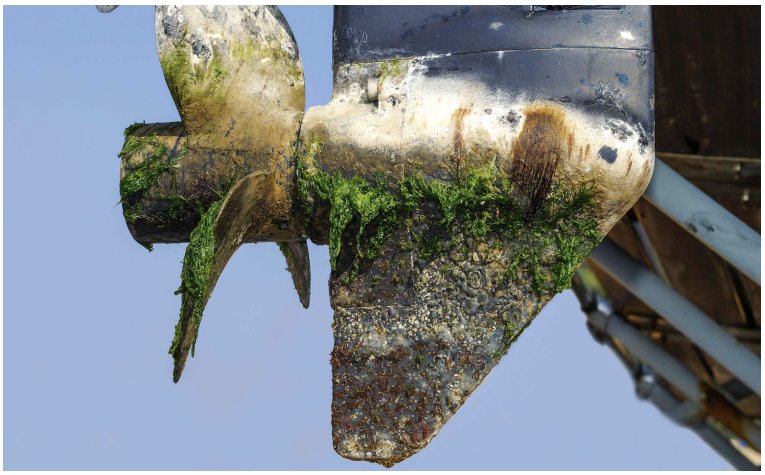

Figure 2.1: Marine biofouling on a boat propeller will affect maneuverability and drag resistance [27].

2.1.1 The concept of biofouling

Microfouling and macrofouling define the two main phases of biofouling. Initially, primary unicellular algae and bacteria will colonize and adhere to the exposed surface, forming a biofilm. This process is the mechanism of microfouling. Macrofouling concerns the further growth of larger organisms, initiated by biofilm formation. Typical species associated with macrofouling are bryozoans, barnacles, mussels, sponges, sea shells, etc. [28].

It is generally understood that biofouling consists of four phases, as illustrated in Figure 2.2 [29]. The first phase considers the adhesion of organic and inorganic macro-molecules, forming a conditioning film on the surface of the immersed article directly after immersion. The second phase develops after minutes to hours and is considered the first phase of microfouling. A microbial biofilm is created by the production of extracellular polymer substances. Unicellular algae, e.g. diatoms, and bacteria colonize and adhere to the conditioning film [30]. Especially, the colonization of diatoms will alter the surface properties of the immersed article and initiate subsequent fouling [31]. The third phase of biofouling, considered the last phase of microfouling, addresses the adhesion of larger organisms, like macroalgae, multicellular organisms, and smaller invertebrates. These substances form a complex colony on the surface of the article days after immersion. Macrofouling is considered the fourth phase of biofouling, occurring a few weeks after immersion. At this point, larger invertebrates, like barnacles, bryozoans, mussels, and hydroids, cause excessive overgrowth as they colonize the biofilm [32].

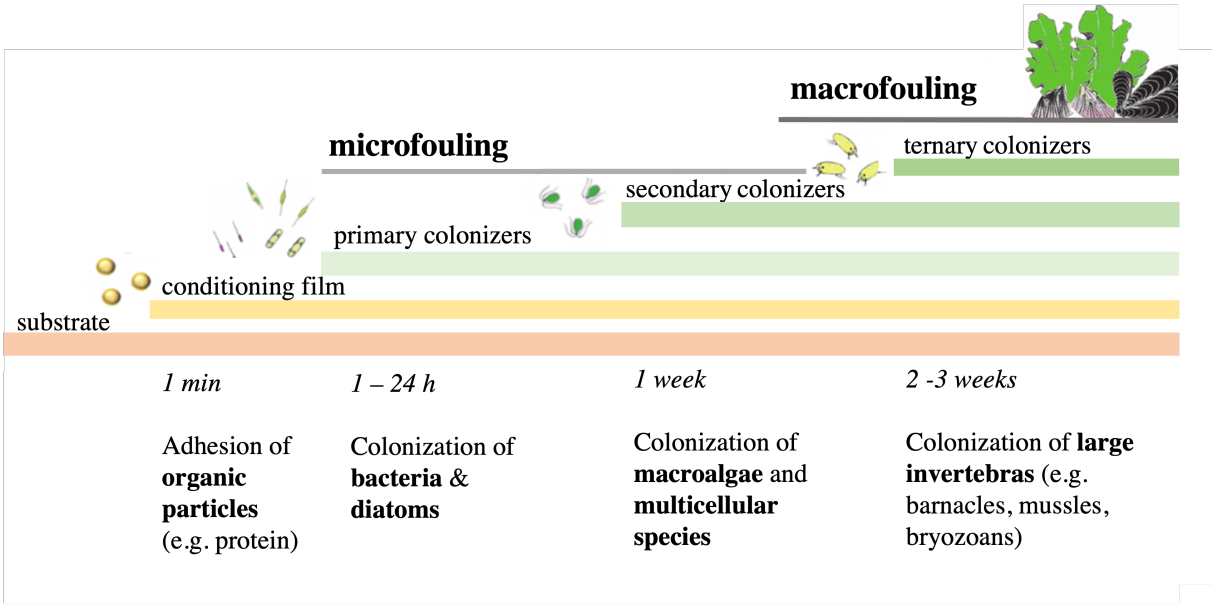

Figure 2.2: Demonstration of the four phases of the biofouling process. The figure is adapted from [29].

2.1.2 Factors affecting biofouling

Biofouling is almost inevitable when unprotected immersed surfaces are exposed to marine environments. However, the degree of biofouling is very much dependent on both physical and biological parameters [33]. These factors are given by the conditions at geographical locations, and cannot be modified to control the biofouling growth. The major biological parameter relates to the impact of predators and competitive species. Most commonly, competitive interactions among fouling organisms lead to the overgrowth of certain species and suppressed the growth of others [34, 35]. Nandakumar *et al.* [36] studied the interspecific competition between common fouling species and found that the hierarchical order followed the sequence ascidians > sponges > bryozoans > brown algae > barnacles > green algae. Other studies show that the presence of protozoans, single-celled eukaryotes, initiates rapid colonization of biofilms on immersed surfaces [37]. The biofilm composition is modified by protozoa grazing on bacteria and microalgae [38, 39].

Physical factors considered essential for biofouling growth concern sunlight, seawater temperature, salinity, and turbidity [40]. Biofouling growth is heavily increased in areas of high seawater temperatures. Areas with significant temperature changes throughout seasons will experience that fouling growth is suppressed in periods with low seawater temperature. In contrast, tropical environments can experience continuous fouling throughout the year [41]. It is found that the majority of fouling species do not thrive in low salinity waters. Yet, fouling species like slime, bryozoa, and algae favor waters of low salinity. Sunlight influences both temperatures and salinity in the top part of the ocean. In addition, it controls the nutrition of fouling species by directly affecting photosynthesis [41].

Other parameters considered relevant for marine biofouling are dependent on the design and surface characteristics of the immersed constructions. These parameters can, contrary to the ones mentioned above, be modified to control biofouling. Studies by Kerr *et al.* [42] showed that biofouling is influenced by surface roughness. His studies indicated that a surface of high roughness was favorable for fouling growth. Wettability concerns the attraction of a liquid phase to a solid surface [43], which has shown to affect the adhesion of fouling species. Contrary findings indicate that both hydrophilic and hydrophobic surfaces can reduce biofouling of certain species based on different mechanisms [44, 45]. This will be further elaborated in Section 2.4.5. Also, the surface free energy of a solid surface has shown to affect the critical pull-off force of marine species. Baier [46] found a minimum of fouling adhesion at surface energies between 20 and 30 mN/m.

2.1.3 Impacts of biofouling

With the extension of international trade throughout the last decade, the shipping industry has experienced unprecedented growth [47]. As a result, a greater threat is built toward the conservation of biodiversity. Ships in the transoceanic maritime industry, covered with biofoulants, introduce new invasive species to local environments. This can potentially result in suppressed growth of native species, whilst dominant species grow into pest proportions. As a consequence, the local economy, public health, and the environment of the affected area can be adversely changed [47]. In addition, biofouling introduces major economical and environmental issues to the shipping industry. The accumulation and growth of marine species on vessel hulls increase ship weight and hull roughness, both affecting the ships' maneuverability and increasing hydrodynamic drag. Consequently, maximum speed decreases so that fuel consumption and greenhouse gas emission increase [48, 49].

The fish farm industry primarily relies on production at sea, using cages and nets to ensure a continuous exchange of seawater with a vital supply of nutrition and oxygen. As for other marine industries, the fish farm industry suffers from the consequences of biofouling. Biofouling on submerged equipment, like fish nets, can cause equipment failure and can reduce the supply of vital nutrition due to overgrowth [50].

All marine industries are prone to corrosion and takes precautionary measures to avoid it. The formation of biofilms on metal surfaces has shown to initiate corrosion, representing an adverse consequence of biofouling in numerous marine industries. The adhered microorganisms change electrochemical conditions at the metal surface by altering the ion concentration, pH, and electrochemical potential [51]. Studies have shown that these changes can result in induction of localized corrosion, change of the general corrosion rate, or even inhibition of corrosion [52]. The suggested mechanism, also referred to as Microbiologically Influenced Corrosion (MIC), is based on a process where fouling species generate acidic metabolites or hydrogen sulfide at the metal-biofilm interface, giving optimal conditions for a corrosive environment. Li *et al.* [53] stated that 20 % of economical losses in marine industries are a result of MIC.

2.1.4 Prevention of biofouling

Antifouling is the process of preventing the adhesion and growth of marine organisms onto submerged constructions [26]. Antifouling has been applied to the marine industry for decades, utilizing various techniques depending on the object to be protected. Coatings with antifouling properties are frequently applied to moving objects, platforms, and objects of complex geometries [54]. Antifouling can also be applied to intake systems, like pipings,

by chemical dosing [55], ultrasonic treatments [56], electrolytic treatments [57], electrochlorination [58], or by introducing biocides to the systems [54].

2.2 Antifouling coatings

Antifouling coatings have been applied to immersed constructions since mid-1800s, with the idea of dispersing toxic components in paints [40]. Today, this is considered the most efficient way to prevent the growth of undesired fouling. There are mainly two approaches for antifouling coatings. One of them is based on impeding fouling adhesion by a biocide-release strategy, while the other one impedes fouling adhesion by utilizing physical-chemical surface properties of insoluble coatings [59, 60]. A biocide is defined as a chemical component or organism with the intention of destroying or expressing a controlling effect towards fouling organisms [61]. In the industry of antifouling, they are often referred to as antifouling agents.

Biocide-release based antifouling coatings are the antifouling technique most commonly applied in the marine coating industry. There exist several approaches for these coatings. In general, the release of biocides can be applied to soluble and insoluble paints and in self-polishing paints [62]. A soluble polymer matrix is the basis of soluble coatings, thus biocides are released as the binder slowly dissolves in seawater. In insoluble coatings, the polymer matrix does not dissolve in seawater. The biocide particles are the soluble components in these coatings and are released as they dissolve in seawater [63]. The self-polishing coatings operate with an acrylic polymer matrix with an ester linkage to an organometallic side group. In seawater, the polymeric backbone and the side group are split by a hydrolysis reaction, releasing biocides at a constant rate. Eventually, the polymeric backbone becomes soluble and dissolves in the seawater. The self-polishing paint is to this day the most efficient antifouling coating as it continuously renews its surface while releasing biocides [64].

Non-biocide-release based antifouling coatings are developed as a "green" alternative to avoid the release of toxic and harmful agents. This approach consists of two main strategies, including easy detachment of settled foulants upon water flow by utilizing slippery surfaces and by preventing the initial attachment of foulants by utilizing physical-chemical surface properties [65]. Section 2.1.2 described the impact that surface design and characteristics could have on antifouling. The strategy of non-biocide-release based antifouling coatings consists of altering these properties to achieve the desired performance. For example, the adhesion strength of biofoulants can be altered by surface energy, surface roughness, and wettability. While preventing the initial attachment of foulants can be achieved by physical constraints on the coating surface. [65]

2.2.1 Antifouling agents

For decades, a variety of antifouling agents have been applied to coatings, including substances like tributyltin (TBT), cuprous oxide (CuO), thiocyanate, and triphenyltin (TPT) [66, 67]. These agents have shown significant efficiency in the prevention of fouling growth, but have also raised concern regarding their influence on marine life [66].

TBT components, such as tributyltin oxide (TBTO) and tributyltin fluoride (TBTF), have shown the greatest antifouling performance. They were first implemented in coating matrices in the 1950s [65] and applied to aquatic vessels worldwide. However, their toxicity has been shown to attack non-target marine species, acting as a strong endocrine disruptor. The most invasive effects included imposex observed in marine species and cardiotoxicity found in mammals [15, 68]. TBT and TPT were banned by the US in the 1980s but were not banned by the International Maritime Organisation (IMO) before 2008. As a consequence, these compounds are still found in harbors and ocean sediment globally [67].

Copper compounds were found valuable as replacements for TBT because of their efficient antifouling performance, lower degree of toxicity, relatively low cost, and availability. It is generally agreed that the antifouling performance of copper compounds mainly arises from the cupric ion, Cu (II). Studies show that Cu (II) only exists on the coating surface, performing its antifouling duty. After release, the compound binds to suspended organic material, deactivating its toxicity [69]. Despite this behavior, heavy metal contamination has been shown to harm marine life. Harbors and marinas have measured copper concentrations of 7 μg Cu L^{-1} [70], which have shown to affect the development and reproduction of marine species like mussels, crustaceans, and others. Consequently, restrictions regarding the use of copper-based antifouling coatings have been made. For instance, the Clean Water Act has set a limit of 3.17 μg Cu L^{-1} in certain harbors [71]. However, the lack of replacements makes copper compounds the main antifouling agent on the market today.

Ideally, antifouling agents should exhibit excellent antifouling behavior, potentially with fouling release properties, while expressing a minimal threat to marine life [40]. Two possible approaches when developing new antifouling coatings include; 1) implementing environmentally friendly antifouling agents in biocide-release coatings, or 2) utilizing surface properties to obtain antifouling and fouling release properties in so-called non-biocide release coatings [72]. Numerous studies investigate different approaches to the development of environmentally friendly antifouling coatings. Hydrophilic surfaces have shown to inhibit protein adsorption and cell adhesion, whilst hydrophobic surfaces show promising fouling release properties as they appear slippery towards fouling species [73]. Grozea *et al.* [74] suggest the design of amphiphilic surfaces, containing a certain pattern of hydrophilic and hydrophobic character, to obtain coatings with combined fouling release and antifouling

properties. Vetere et al. [75] found the non-toxic organic compound, benzoate, to be efficient in inhibiting the settlement of foulants. Other studies have found zosteric acid, a natural compound found in eelgrass, to have promising antifouling behavior towards certain fouling species [76–78]. In 2020, the EU funded the ZABIO project in the development of zosteric acid as the first green, non-toxic antifouling agent for coatings and paints in the marine industries [79]. Bactericidal behaviors have been observed in graphene materials (GMs), mainly in pristine graphene (G), graphene oxide (GO), and reduced graphene oxide (rGO). These compounds are biocompatible with apparently low cytotoxicity, and free from metallic impurities, making them promising candidates in the research of finding environmentally friendly antifouling agents [80]. In addition, they have demonstrated improved mechanical, electrical, and thermal properties [81] and expressed antifouling behaviors [80] when dispersed in polymer matrices.

2.2.2 Application of graphene based materials for antifouling purposes

Graphene based materials

Carbon allotropes, like graphite, fullerene, and diamond, are all based on one basic two-dimensional element, graphene (G), illustrated in Figure 2.3 (a). G is built up of carbon atoms, shaped in a hexagonal lattice structure, stabilized by sp^2 bonds [80, 82]. G is considered an exciting material, being the thinnest known and the strongest material ever measured [83]. It possesses a high surface area of 2630 m^2g^{-1}, a high Young's modulus of 1 TPa, good thermal and, electrical conductivity and low weight [84]. In addition, an intrinsic strength of 130 GPa has been measured for G [85], and the material is generally considered hydrophobic [86] with no water solubility [87]. Thus, G is considered a suitable constituent in a variety of industries; electronics, bio-medicine, energy, membranes, transport, composites, and coatings [88, 89]. Commercially, G is produced by Chemical Vapor Phase Deposition (CVD), Liquid-Phase Exfoliation (LPE), or by epitaxial growth in SiC [90].

In 1859, before G was discovered, Benjamin Brody synthesized graphene oxide (GO). The compound is defined as a single atom carbon layer modified with oxygenated functional groups on both surfaces, with elements of alcohols (-OH), epoxies (C-O-C), and carboxylic acids (-COOH) [91] (see Figure 2.3 (b)). Despite the structural similarities of G and GO, their properties differ significantly. The hydrophilic nature of GOs functional groups makes GO a water-soluble nanomaterial with a hydrophilic nanostructure [87, 92]. It possesses a very low electrical conductivity and significantly higher chemical activity [91]. Studies have also reported GO to exhibit lower mechanical properties, e.g. an intrinsic strength of 130 MPa [93]. Synthesize techniques commonly utilized for GO production include the Staudenmaier method [94], the Hummers method, and the modified Hummers method [95].

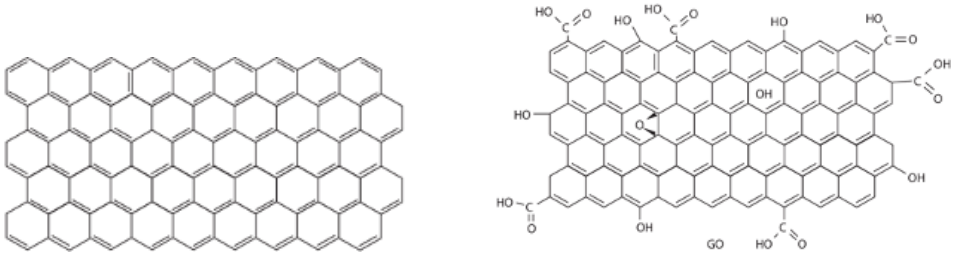

(a) **(b)**

Figure 2.3: Illustration of the structure of (a) graphene and (b) graphene oxide. Adapted from [96].

Antifouling performance of graphene and graphene oxide

Several studies confirm that G and GO exhibit promising antifouling properties in nanocomposites [97, 98]. Jin *et al.* [97] demonstrated excellent antifouling performance of 0.36 wt% GO in a silicon rubber matrix. The predominant mechanisms described today propose that the antifouling activity of GMs originates from physical interactions with microorganisms or from the induction of oxidative stress [99].

Physical interactions of GMs occur as a result of their two-dimensional structure with sharp edges and large basal planes, causing wrapping, trapping, and cell disruption of target species. Hu *et al.* [100] discovered that GOs and rGOs damaged cell integrity by having a nano-knife effect on *E. coli* bacteria. Pham *et al.* [101] described the nano-knife effect as a mechanism where the sharp edges of G nanosheets cause pore formation in the cell wall of bacteria, leading to osmotic imbalance and cell death. His studies also indicated that an increased antifouling activity was observed at higher densities of graphene edges. Zou *et al.* [102] reported a weakened nano-knife effect at an increased GM thickness, as a result of an increased number of GM layers. The large basal planes of GMs have also shown to facilitate their antifouling behavior. The planes wrap around and trap bacteria, preventing access to vital nutrition which leads to bacteria inactivation [103]. Liu *et al.* [21] demonstrated higher activity with a larger lateral size of GO sheets mainly due to easier wrapping and a stronger adsorption ability at a higher surface area. Some studies have also shown that the hydrophobic nature of G sheets can cause membrane disruption by extracting lipids from bacteria due to strong attraction forces [19, 104].

The induction of oxidative stress is reported as a mechanism of the antifouling performance of GMs. Oxidative stress can damage the membrane of fouling species by introducing lipid peroxidation or causing dysfunction of proteins and DNA, potentially causing cell death [99]. Generally, oxidative stress can be generated by the production and accumulation of reactive oxygen species (ROS), like O_2, H_2O_2, and $\cdot OH$, or through simple charge transfers [99]. Several studies have observed an increased ROS activity in bacteria when combined with GMs [105–107]. Generation of $\cdot OH$ was detected in a GO dispersion, which indicated that

the antibacterial behavior of GO can occur through oxidative stress by ROS generation [105]. Castrillón *et al* [108] proved that cell damage by ROS generation is a non-contact interaction. ROS-independent antifouling activity is found for G, where G acts as an electron acceptor, extracting electrons from cell membranes [109].

Toxicity of GMs

The suggestion of applying G and GO as alternatives for new antifouling agents requires the materials to express low toxicity towards non-foulants. In general, graphene and graphene oxide are considered promising for biomedical applications due to their good biocompatibility. However, the toxicity of graphene materials is rather unknown compared to other carbon materials and the available studies are slightly contradicting [110, 111]. The introduction of graphene in various biomedical applications has increased the number of toxicity studies in the last decade. An in vivo study by Gollavelli *et al.* [112] observed that graphene injected into zebrafish embryos did not generate abnormalities. GO has shown indications of chronic toxicity and lung granuloma death in mice. In vitro studies of cell cultures indicated that GMs exhibit overall lower toxicity compared to carbon nanotubes (CNTs) [113]. Generally, studies of G and GO demonstrate that their toxic effect is dose- and shape-dependent, with no significant effect for low and medium concentrations [114].

2.2.3 The principle of epoxy-based coatings

Epoxy-based coatings are commonly applied to the marine industry as it offers properties highly relevant for coating applications. In a coating matrix, epoxy resin functions as the physical backbone. Other important components include appropriate solvents, to achieve desired viscosity, and curing agents, to enhance the curing process of the epoxy. Solvent-based epoxy coatings cure by solidification explained by the sol-gel process. Inorganic additives, with desired properties, are commonly added to coating matrices for various purposes, e.g. colouring, strengthening, or antifouling. Epoxy nanocomposite-based coating is a general term for epoxy coatings with the addition of nanosized additives [115]. G and GO have both been implemented as nanocomposites in epoxy resins with the motivation of increasing antifouling, mechanical and thermo-mechanical performance [98, 116, 117].

The sol-gel process

The sol-gel process is commonly utilized for synthesis of nanocomposite coatings with the ability to produce homogeneous dispersion with chemical linkages between the nanoparticles [118]. The method offers high reproducibility, versatility, easy application to thin films and coatings, low processing temperature and low cost [119]. The final product of the process consist of a three-dimensional oxide network formed by a hydrolysis reaction of epoxy resin, followed by or simultaneously assisted by a condensation reaction [120].

Solution blending and in situ polymerization are two sol-gel methods available for synthesis of nanocomposite epoxy coatings. Solution blending typically consist of mixing the nanoparticles with a compatible solvent, and subsequently mix it with a polymer [121]. The method offers several advantages including easy operation, good particle dispersion due to low viscosity [122] and reduced permeability of gases. Drawbacks associated with solution blending mainly include the concern of re-aggregation of nanoparticles [123]. In in-situ polymerization, the nanoparticles are dispersed directly into a monomer. An appropriate solvent is often added to achieve desired viscosity. Aggregation is of less concern in this process, as the nanoparticles are homogeneously dispersed before the polymerization process starts. Other benefits include controllable particle morphology [124] and high transparency [125]. However, ease of agglomeration has been reported as the main limitation [123]. In both solution blending and in situ polymeriztion, mixing is often assisted by ultrasonic treatments, magnetic stirring or shear mixing [123]. The solidification of these two processes is initiated by solvent evaporation, where formation of covalent bonds will occur between nanoparticles and the epoxy matrix. This process is known as the polymerization process leading to the development of a complete oxide network. Solidification can also be initiated by adding a suitable initiator and by optimizing time and temperature [126].

It has been reported that GO has an excellent interfacial adhesion with epoxy matrices, being beneficial in relation to sheet distributions, cross-linked density and to stress transfer between the epoxy matrix and GO. This is a result of the presence of reactive functional groups, like carboxylic groups, hydroxides and epoxides, on the GO surface reacting with the epoxy precursor, while the wrapped surface of GO sheet ensures good mechanical interlocking [127]. Generally, G is considered less compatible for nanocomposite applications compared to GO. The lack of oxygenated functional groups on the G sheets impedes the formation of strong interfacial bonding within the epoxy matrix and promotes stronger attraction between the sheets, making it difficult to obtain homogeneous nanocomposites [128]. Chemical functionalization of graphene has shown to facilitate dispersion stability to prevent agglomeration of G [129]. Functionalization of G with polyoxyalkyleneamine has also shown to enhance interfacial adhesion to epoxy matrices, enhancing mechanical properties of epoxy nanocomposites [130]. This has previously been achieved by amination, esterification [131] and polymer wrapping [132].

Epoxy resins

The epoxy resin serves as the physical structure of solvent based coatings. It appears thermally stable, electrically insulating, chemically resistant, with high durability and strength, low density and strong adhesion and affinity to heterogeneous materials, making it an excellent constituent in coating applications [133].

Epikote 828 resin is an epoxy resin appropriate for coating production, produced from

bisphenol A and epichlorohydrin [134], as illustrated in Figure 2.4. It is described as an medium viscosity epoxy resin with high chemical and mechanical resistance in cured state. The chemical structure of Epikote 828 is illustrated in Figure 2.4 [134].

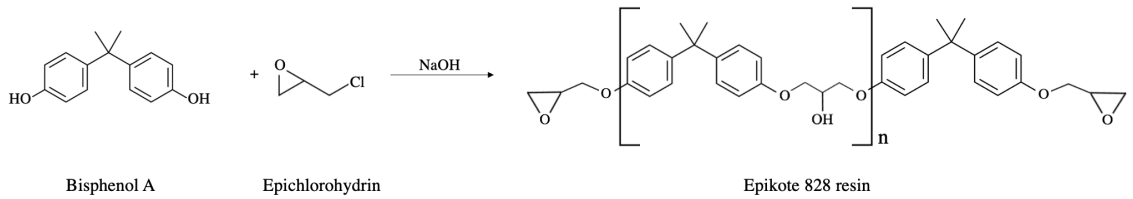

Figure 2.4: The chemical reaction between bisphenol A and epichlorohydrin to form Epikote 828 epoxy resin.

The solidification process is often assisted by a suitable curing agent. The curing agent contain reactive hydrogen groups that react with epoxide and hydroxyl groups of the epoxy resin to form a three-dimensional cross-linked network through a polymerization processes. The poly(propylene glycol) bis(2-aminopropyl ether) (PPGBAE) curing agent, is commonly used in polymerization processes of epoxy resins based on bisphenol A [135]. PPGBAE is a diamine, and its chemical structure is illustrated in Figure 2.5.

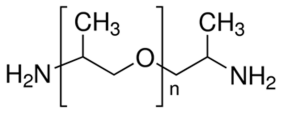

Figure 2.5: The chemical structure of the diamine poly(propylene glycol) bis(2-aminopropyl ether) with n $\approx$ 2.5 [135, 136].

Epikote 828 react with PPGBAE in a polycondensation process, as shown in Figure 2.6. The process consists of three principle reactions; 1) The diepoxide group of Epikote reacting with the primary amine H of PPGBAE to form a secondary amine. A cross-linked polymeric network is subsequently formed by the reaction between 2) secondary amines and epoxides and between 3) hydroxyl groups and epoxides [137].

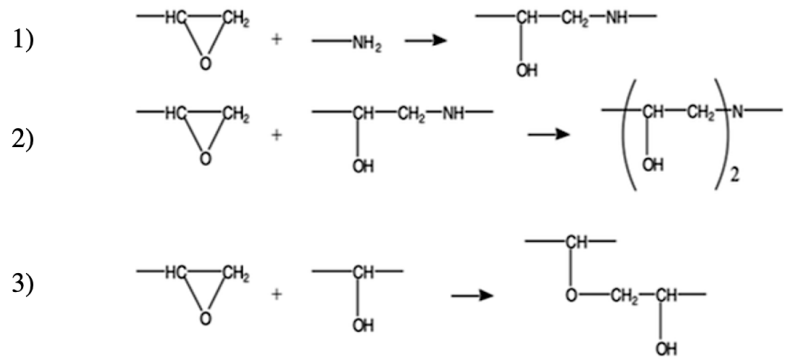

Figure 2.6: The three principle reactions of the polycondensation between an epoxy and diamine; 1) formation of a secondary amine from a reaction between an diepoxide group and a primary amine H, 2) reaction between the secondary amine and epoxides and 3) hydroxyl groups and epoxides [137]. Figure adapted from [138].

Coating applications

In the marine industry, spray coating is used as a standard technique for coating application, concerning coating of vessels and other marine installations. Spray coating comes with the advantages of high efficiency for large-scale production and the ability to coat substrates with large surface areas with controlled thickness [139]. The thickness and surface morphology of coatings can be controlled by regulating the concentration ratio of epoxy and solvent, the particle size of pigments or additives, the rate of deposition, and the number of coating layers [140]. A known disadvantages of spray coaters concern the possibility of uneven coating thicknesses and reduced overspray, due to the suppressed motion control as spray coaters are commonly handheld.

Air sprayers and airless sprayers are both commercially utilized in the coating industry. Air sprayers use compressed air or nitrogen gas to push the coating slurry through a small nozzle at low pressure, generally 1 bar [141]. Air can mix with the coating and potentially cause blemishes and bubbles in the final coating product. 99% of the marine industry utilizes airless sprayers, which use pressure streams (30-400 bar) without the use of compressed air. This eliminates the possibility of bubble or blemish formation and makes it very portable [142, 143]. However, the high pressures require additional safety precautions [141].

The spray coating technique is highly dependent on achieving a low viscous coating slurry, and a solvent content of 70-80% is commonly applied [144]. When the coating cures, volatile organic compounds (VOC) will evaporate and be released into the air, contributing to air pollution [145]. A reduction in solvent content is achieved by utilizing waterborne coatings. However, the wide variation of drying times is a serious complication of waterborne coatings as it varies with relative humidity [146].

Dip coating is another technique commonly applied to coating application. This is considered an easy coating technique with advantages of low cost, coating of complex shapes, and controlled layer thickness and roughness [141, 147]. However, dip coating is limited in relation to substrate size and is normally applied to flat or curved surfaces of relatively small sizes [148].

2.3 Characteristics of sols and slurries

2.3.1 Dispersion stability

In the coating industry, attention is continuously given to the stability of coating dispersions in order to achieve a homogeneous particle or pigment distribution within the coating product. Antifouling coatings contain additives, often presented as nanoparticles, in suspensions. In general, it is understood that nanoparticles have a strong tendency to form large clusters [149]. The nanoparticles tend to form either aggregates, which consist of strong covalent bonds between the nanoparticles, or agglomerates, consisting of weaker forces which are easier to separate [150]. Stabilization techniques are commonly implemented to avoid the generation of clusters. In theory, there exists three of them; electrostatic, steric and electrosteric stabilization [120, 151]. The three mechanisms of colloidal dispersion stability are illustrated in Figure 2.7.

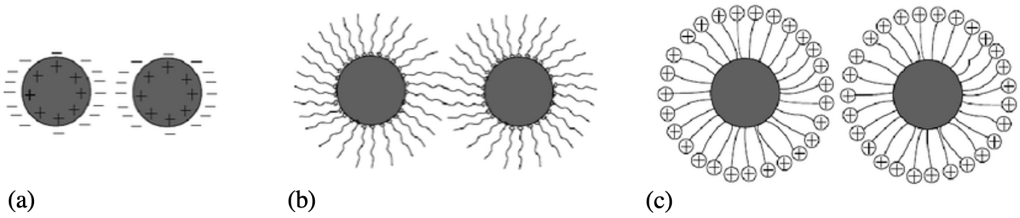

Figure 2.7: A schematic representation of the three stabilization techniques for colloidal dispersion including; (a) electrostatic stabilization, (b) steric stabilization and (c) electrosteric stabilization. Adapted from [152].

Electrostatic stabilization

Stabilization of colloidal suspensions can be obtained by utilizing the development of surface charges of nanoparticles in polar solvents or electrolyte solutions [153]. The introduction of surface charges result in an electrostatic repulsion between the particles which is larger than their attractive forces, so that a stable dispersion with evenly distributed particles is obtained [154]. In general, the total charge of a dispersion will be neutralized by the presence of oppositely charged counter ions. Yet, a heterogeneous distribution of ions and counter ions will develop near the surface of the charged nanoparticle. In this proximity, electrostatic forces,

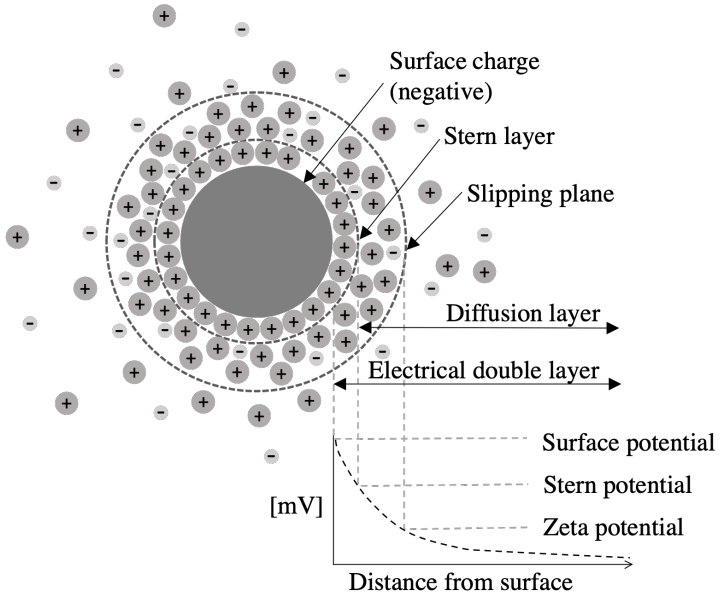

Figure 2.8: An illustration of the formation of a electric double layer in the promixity of a charged nanoparticle, consisting of the Stern layer and the diffusion layer. The zeta potential is given as the difference in potential measured from the slipping plane to the particle surface. The figure is adapted from [159].

entropic forces and Brownian motion act on the charged ions leading to the formation of an electric double layer. The double layer consists of a Stern layer and a Gouy (diffusion) layer, as illustrated in Figure 2.8, and represents a concentration gradient with highest concentration of counter ions near the particle surface, which decreases further away from the surface [153].

The zeta potential can be utilized as a measure of electrostatic dispersion stability, and is defined as the potential difference between the slipping plane, representing the final distance at which charged ions will move with the particle, and the particle surface [155, 156]. Dispersion particles tend to repel each other at large positive or negative zeta potentials. The universal line at which electrostatic stabilization is dominating is found to be at a zera potential outside the limits of +30 or -30 mV [151, 157]. pH, ionic strength, concentration of additives and temperature are found to be influencing factors of the zeta potential [158].

Steric and electrosteric stabilization

Steric stabilization is commonly applied to stabilization of colloidal dispersions. Literature often refers to it as polymeric stabilization as the mechanism consists of absorption of polymers or uncharged molecules on the surface of nanoparticles [153]. These macromolecules are called surfactants and are added to a dispersion to serve as a physical barrier between charged nanoparticles, preventing the formation of VdW attraction forces [160]. Electrosteric stabilization is a stabilization technique that utilized both electrostatic and steric repulsive forces by the means of providing ionic surfactants [161].

Stabilization of G and GO dispersions

It is mutually agreed that it is a challenge to stabilize graphene materials in colloidal dispersions due to their large specific area. This tends to initiate agglomeration of GMs in bulk due to the strong presence of attractive forces, like Van der Waals forces [162]. Consequently, numerous studies investigate and propose techniques for the stabilization of G and GO dispersions.

Liu *et al.* [163] found that G possessed a surface charge when dispersed in various organic solvents by measuring the zeta potential of G. He suggested that the surface charge was a result of electron transfer between G and the solvent molecules, and concluded that electrostatic repulsion was the main contribution to the stable dispersions. G is found stable in non-aqueous solvents including acetone [164], N-Methyl-2-pyrroline (NMP), dimethyl sulfoxide (DMSO), and N,N-dimethylformamide (DMF). G is found poorly dispersed in ethanol, with a zeta potential far off the benchmark ($\pm$ 30 mV) of 2.87 mV [165]. The hydrophobic nature of G makes it difficult to use water in dispersion. Instead, G has been dispersed in aqueous solutions by functionalizing with surfactants [166, 167].

Mehmood *et al.* [168] studied the zeta potential of GO in solvents and found that GO sheets experienced a high degree of repulsion at high zeta potentials. He found that GO sheets were stabilized in ethanol, measuring a zeta potential of 23 mV, and suggested it to be a result of electrostatic stabilization. The same study observed GO sheets to be poorly dispersed in acetone, measuring a zeta potential of 6 mV, concluding that electrostatic stabilization was of no significance in this dispersion. A study by Khan *et al.* [169] reported stable dispersions of GO when using water, tetrahydofuran (THF), DMF, ethylene Glycol, or pyridine. Another study by Paredes *et al.* [170] reported short-time stability of GO in ethanol, acetone, 1-propanol, DMSO, and pyridine. However, long-term stability was achieved with water, ethylene glycol, DMF, NMP and THF.

2.3.2 Rheology behavior of fluids

It is important to understand the behavior of fluids in order to obtain a proper coating finish with desired characteristics. In particular, the fluid properties plays a vital role when considering coating application, dispersion mixing and shelf life. The fluid properties have shown to alter sedimentation of solid particles during storage, e.g. a higher viscosity has shown to reduce sedimentation efficiency of dispersions [171]. Rheology concerns the study of deformation and flow of matter primarily in liquid and gas state [172]. Viscosity (μ) is considered one of the most important rheology properties, defining the ability of a fluid to resist deformation under shear stress [173]. It is defined as the ratio of shear stress, σ [Nm^{-2}], to shear rate, γ [s^{-1}], as expressed in Equation 2.1.

$$\mu = \frac{\sigma}{\gamma} \qquad \text{[Pa s]} \quad (2.1)$$

The shear stress relates to the force acting on the fluid parallel or tangential to the face of a material, while the shear rate corresponds to the rate at which a fluid is sheared during flow [174].

Rheology studies define fluids as either Newtonian or non-Newtonian [175]. When applied shear stress is proportional to shear rate, the viscosity of a fluid is constant, depending only on temperature. This type of fluid is characterized as a Newtonian fluid. Simple liquids of low molecular weight are typically found Newtonian, e.g. water [176]. The converse behavior of a fluid corresponds to a viscosity that depends on either shear stress or shear rate, being a non-Newtonian liquid. It is common to find that polymers and dispersion of solid particles in continuous phase behave as non-Newtonian fluids [175]. Non-Newtonian fluids behave either shear thinning or shear thickening, meaning that the viscosity decreases or increases with increasing shear rate, respectively. A shear thinning behavior is generally found in coatings, which often contain both polymers and small particles. On the contrary, it is more common to observe a shear thickening behavior in liquids with a high concentration of particles. Figure 2.9 illustrates the viscosity as a function of shear rate for Newtonian, shear thinning, and shear thickening fluids. A rheometer is conventionally used to measure rheology properties of fluids, commonly applied with the concentric rotational cylinder method for viscosity measurements of non-Newtonian fluids [177].

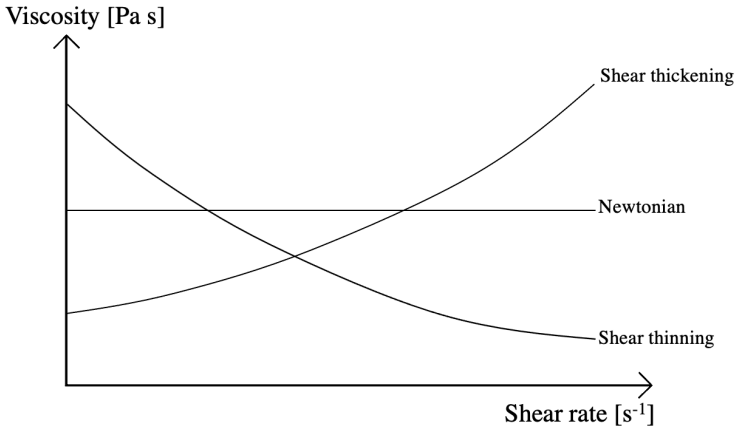

Figure 2.9: Viscosity as a function of shear rate. The graphs represent a Newtonian fluid and non-Newtonian fluids with shear thickening and shear thinning behavior.

Coating applications performed by spray coating requires fluids with appropriate flow, with the ability to maintain its shape immediately after application. In the coating industry, a viscosity in the range of 0.05-0.5 Pa·s is considered optimal for airbrush applications. Typical shear rates given by airbrushes vary from 1000 to 4000 s^{-1} [178]. Relevant values of

viscosity can be found in Table 3.9 including water, ethanol, acetone, Epikote and PPGBAE.

Table 2.1: Viscosity values of relevant components, including water, ethanol, acetone and Epikote at 25 ° [134, 179, 180].

Component	**Viscosity** [mPa · s]
Water	1.002
Ethanol	1.074
Acetone	0.320
Epikote	$32 \cdot 10^3$

2.3.3 Analysis of functional groups

Knowledge about the coating compositions prior to and after coating application is of great importance in relation to understand the coating quality. Determining the coating composition or observing changes in coating composition over time can potentially demonstrate the degree of cross-linking within epoxy coatings and indicate short- or long-term stability of coating slurries.

Infrared (IR) spectroscopy is commonly used for characterization, identification and quantification of a wide range of substances. This method is considered highly reliable with the ability to analyze solids, liquid and gases. In IR spectroscopy measurements, the output value is an IR spectrum where the IR intensity, in mean of either absorbance or transmittance, is plotted as a function of wavenumber, or frequency, of light [181]. To put it briefly, the method measures the vibration of chemical bonds that occurs when molecules absorb IR radiation. These vibrations occur at distinctive frequencies due to the structural differences of the molecules, enabling "fingerprint" characterizations of specific functional groups present in the molecules [181].

The origin of peak positions, wavenumbers, of functional groups in the IR spectrum is explained by the definition of the frequency of vibration, given in Equation 2.2.

$$\nu = \frac{1}{2\pi}(\frac{k}{\mu})^{1/2} \qquad [\text{cm}^{-1}] \quad (2.2)$$

where ν corresponds to the frequency, k is the chemical bond's force contact and μ is the reduced mass of the molecule upon IR absorption. As no chemical substances in the world possess equal force constants or atomic mass, the obtained frequency of a functional group will be unique and define its peak position [182].

Different vibrations express different band intensities in the IR spectra. The origin of these peak intensities is (1) due to difference in bond stretching and (2) due to difference in the

concentration of molecules. Absorptivity, ϵ, is an absolute value of a peak intensity, defined by Beer's law given in Equation 2.3.

$$A = \epsilon l c \tag{2.3}$$

where A is the absorbance, l is the path length and c is the concentration of different molecules [182]. Hence, the peak intensity of IR spectra can be utilized to indicate the concentration of functional groups in a solution. A common name for describing peak intensities in IR spectroscopy, which can span over a range of wavenumbers, is bands, valid both when absorbance or transmittance is used as the measure of intensity.

Attenuated Total Reflectance Fourier Transform Infrared (ATR-FTIR) spectroscopy is developed for the purpose of characterizing functional groups of solid surfaces and in liquid bulks by the principles of IR spectroscopy, and yields the advantages of simple sample preparation and spectral reproducibility [183]. This method is highly applicable for characterization of functional groups in epoxy slurries. In particular, the 914 cm^{-1} is the most important peak in epoxy coating as it corresponds to the epoxide group. Studies suggest to utilize the ratio of the peak intensities at 914 cm^{-1} and 1608 cm^{-1} (C-C stretching) to measure the relative degree of cross-linking, as 1608 cm^{-1} does not participate in the cross-linking process [184]. In addition, the technique has proved useful for studies of the chemical cross-linking between GO sheets and alkyd resin in GO paints [185].

2.4 Characteristics of cured coatings

The marine industry will expose coatings to harsh environments. To ensure good quality and optimal service life, it is important to evaluate mechanical properties applicable for antifouling coating applications. Such properties can include coating hardness, Young's modulus, scratch resistance, and adhesion. Some coating properties have in addition shown to alter antifouling properties of coatings, including surface roughness, wetting properties, and surface free energies.

2.4.1 Hardness and Young's modulus

Hardness and Young's modulus play an important role when evaluating coating durability. The hardness value can indicate the coatings ability to withstand permanent deformation when exposed to a mechanical impact. Hardness is considered a relative value, which means that the measured value will depend on the test technique and vary with loading weight, rate and method [186]. The Young's modulus of a coating reveals the coatings ability to elastically stretch and deform. Unlike hardness, Young's modulus is an intrinsic property which means that it should be independent on test technique and other external conditions [187].

Nanoindentation

Generally, hardness and Young's modulus of thin films and coatings are measured by nanoindentation [187]. This method allows for precise measurements at nanoscale with high control of penetration depth and applied force. The main issue with conventional indentation measurements of coatings and thin films at macroscale is the substrate influence, which can be neglected with nanoindentations. It is found that any influence from the substrate is neglected when the penetration depth of nanoindentation measurements does not exceed 10% of the coating thickness [188].

In a nanoindenter, a diamond tip of known geometry is indented on a material surface at controlled conditions. A typical nanoindentation measurement record applied load and penetration depth from zero to maximum load and then back to zero, as illustrated in the load-displacement curve in Figure 2.10 (a). At macroscale, a visible impression would be observed in a microscope and related to the material hardness [**?**], known as the Vickers test. However, at nanoscale the residual impression is too small to be measured with the conventional technique of the Vickers test. Instead, the hardness and Young's modulus is found by projecting the contact area of the indenter and the sample by utilizing the known tip geometry and extracting the penetration depth at maximum load [187]. An illustration of the projected contact area and penetration depth at maximum load is shown in Figure 2.10 (b).

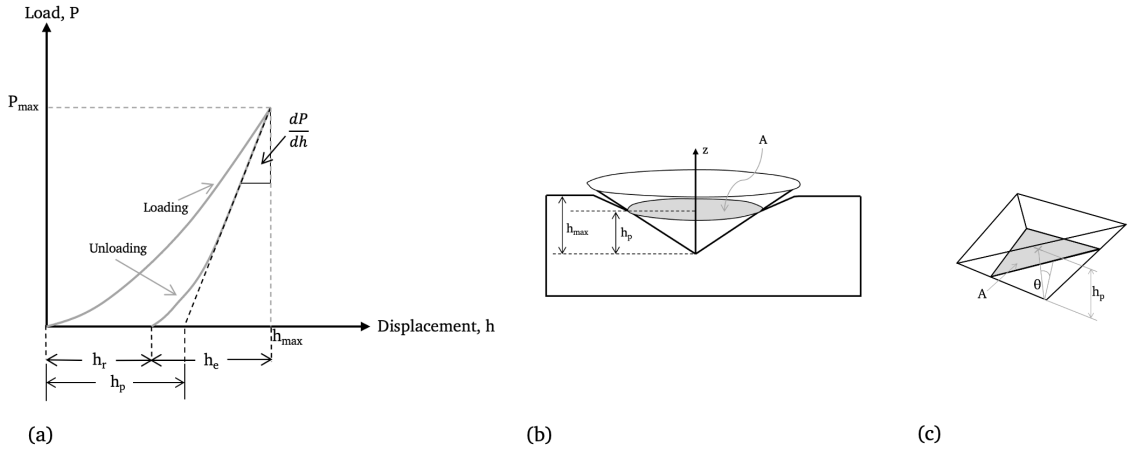

Figure 2.10: Illustration of the (a) load-displacement curve of a nanoindenter experiment with maximum load, P_{max}, maximum displacement, h_{max}, plastic penetration depth, h_p and the slope of the unloading curve at maximum load, dP/dh, (b) nanoindentation with a Berkovich tip showing h_p and projected area of contact, A and (c) geometry of the Berkovich indenter with corresponding face angle, θ. Figures adapted from [187].

The Berkovich indenter is commonly applied to nanoindentation measurements as its geometry yields a sharp point compared to the four-sided geometry of the Vickers indenter [189]. The projected area of contact, A, for the Berkovich indenter is given by Equation 2.4.

$$A = 3\sqrt{3}h_p^2 tan^2\theta \qquad [\text{m}^2] \quad (2.4)$$

h_p corresponds to the plastic depth of penetration and θ corresponds to the face angle with central axis of the indenter. Figure 2.10 (c) illustrates the related indentation parameters for a Berkovich indenter. The Berkovich indenter has a known face angle equal to 65.27°, and the area of contact can be simplified to,

$$A \approx 24.5h_p^2 \quad (2.5)$$

The material hardness can be further expressed in terms of applied load, P_{max}, and projected area,

$$H = \frac{P_{max}}{A} \approx \frac{P_{max}}{24.5h_p^2} \qquad [\text{MPa}] \quad (2.6)$$

The final value of the material hardness is found by combining maximum load and the displacement h_p extracted from the intercept of the linear unloading curve on the displacement axis, as shown in Figure 2.10 (a) [187].

During load removal, the coating will try to recover to its original form. Despite the plastic deformation, some degree of recovery will occur due to the relaxation of elastic strains within the coating. Accordingly, the unloading section of the load-displacement curve can give an estimate of the Young's modulus of the coating [187].

The reduced Young's modulus, E_r, can be extracted from the load-displacement curve, shown in Figure 2.10 (a), by considering the slope of the unloading curve at maximum load, dP/dh, and the projected contact area A at maximum load (see Equation 2.4),

$$E_r = \frac{\sqrt{\pi}}{2\sqrt{A}} \frac{dP}{dh} \qquad \text{[GPa]} \quad (2.7)$$

Further, the real value of Young's modulus can be found by Equation 2.8, considering E_r and the Poisson's ratio of the indenter and the sample [187].

$$\frac{1}{E_r} = (\frac{1-\upsilon^2}{E})_{sample} + (\frac{1-\upsilon^2}{E})_{indenter} \quad (2.8)$$

It is generally agreed that diamond indenters posses an $E_{indenter}$ of 1140 GPa and a Poisson's ratio, $\upsilon_{indenter}$, of 0.07. The Poisson's ratio of the specimen normally varies between 0 to 0.5 [187], and is found to be 0.35 for a bisphenol A type epoxy resin [190].

Ivanov *et al.* [191] performed nanoindentations on Epikote-based nanocomposites with exfoliated graphite (EG) to investigate nanomechanical properties. Hardness and Young's modulus of the nanocomposites with concentration of EG ranging from 0 to 2 wt% were obtained by using a maximum indentation load of 200 mN. The hardness value of pure Epikote coatings were found to be 0.209 $\pm$ 0.011 GPa, with an Young's modulus of 3.365 $\pm$ 0.104 GPa. Generally, an improvement in hardness and modulus was observed in the range of 0.25 to 1 wt% EG. Higher concentrations indicated lower values, assumed to be a result of poor dispersion of the exfoliated graphite.

2.4.2 Scratch resistance

The scratch resistance of coatings is another property relevant for coating durability. Scratch resistance can express a materials ability to withstand abrasion without fracturing. A nanoindenter is commonly used to measure the scratch resistance of thin films and protective coatings [187].

There exists several configurations of scratch tests by nanoindentation. In general, a normal force, F_N, is applied to the indenter, while moving over the specimen surface at a fixed dis-

tance. This force can either be held at a constant level or it can increase or decrease during scratching by a tangential force, F_T. Typically, nanoscratch tests are performed with an increasing normal force. During scratching, lateral force and lateral displacement and vertical force and vertical displacement are measured simultaneously [192]. The scratch resistance is defined as the critical load at which failure in the coating surface occurs. The critical load can be determined by visual inspection in an optical microscope or by observing an abrupt change in the lateral force, penetration depth or friction coefficient. Caution should be made when measuring scratch resistance with the use of critical load as the obtained results relies on a range of parameters including scratch speed, load rate, tip radius and geometry and substrate roughness [193]. However, the method can be utilized for comparative testings. A schematic of the scratch test configuration is shown in Figure 2.11, including the normal force, F_N, the tangential force, F_T and the critical force, F_C.

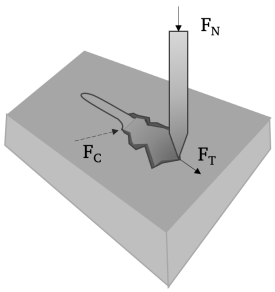

Figure 2.11: The configuration of a nanoscratch test including the normal force, F_N, the tangential force, F_T and the critical force, F_C.

The friction behavior of materials can be deduced from scratch test data and can indicate a materials resistance to scratch. A hard material with high wear-resistance would express a higher scratch resistance, and the measured COF of the nanoscratch test will consequently be higher [194]. The coefficient of friction (COF), μ, is a dimensionless value that describes the amount of friction present between two types of surfaces. As described in Equation 2.9, COF is defined as the ratio of lateral force to normal force [195].

$$\mu = \frac{F_T}{F_N} \tag{2.9}$$

Several studies have reported that the presence and type of fillers and nanoparticles in epoxy matrices have a significant effect on the friction behavior of the material [196–198]. Zhang *et al.* [199] suggested that a lower COF observed for epoxy coatings with carbon nanofiber and MoS_2 nanohybrids was a result of an increase in specific surface area of MoS_2 due to its wrapped structure. The nanocomposite forms a three-dimensional structure in the epoxy matrix, making it possible for the epoxy matrix to transfer stresses to the nanohybrids when subjected to an external force. Few tribological studies investigate the effect of G and

GO in epoxy resins. However, the weak VdW forces of GMs gives them solid lubrication property. These properties makes GMs promising candidates for production of anti-friction epoxy coatings [200]. Some studies have reported a reduction in COF with addition of G/GO nanofillers [200–202] as a result of the lubricity of GMs and a homogeneous sheet distribution within the epoxy matrix. Gafsi *et al.* [201] confirmed the former, but found that the COF increased for higher weight ratio of GO (> 0.5 wt%) due to the formation of nanosheet agglomerates.

2.4.3 Adhesion

Adhesion is a key property in the coating industry, concerning the ability of two dissimilar surfaces to attract each other. Coatings are exposed to aggressive conditions in the marine industry, and it is therefore essential to ensure good adhesion to obtain high coating quality and durability. For antifouling applications, exposure of the protected surface would enhance fouling growth. Adhesion is generally considered a complex phenomenon, relying on the coating chemistry, the chemical and physical contribution of the substrate and on surface pre-treatments.

Factors influencing adhesion

Knudsen *et al.* [203] emphasizes mechanical interlocking, chemical bonds, intermolecular forces and molecular interactions as the contributing adhesion forces between polymers and metals. Intermolecular forces or Van der Waals forces, including dipole-dipole interactions, dispersion and induction forces, have been considered the most important contribution to adhesion strength with a relative long bond range (>10 nm). Bolger [204] explains the importance of chemical bonding when considering coating adhesion with organic resins, like epoxies. Metal surfaces will, with few exceptions, always appear as metal oxide surfaces. A high density of hydroxyl groups will appear on the substrate surface due to hydration of oxygen. These hydroxyl polar groups will enhance chemical bonding to polar functional groups of polymer resins, and increase adhesion strength. Contrary findings question to what degree chemical bonds, covalent or ionic, contribute to adhesion strength due to their short range (<0.1 nm) and the belief of low concentration of functional groups in polymer coatings [203]. Reactive silanes are commonly added as coupling agents in epoxy coatings to promote covalent bonds with the substrate and simultaneously engage in the cross-linking of the coating system [205]. Mechanical interlocking is an essential adhesion force, where mechanical bonds will form as the coating crimp around topographic irregularities of the substrate and anchor beneath them. Mechanical interlocking can be promoted by surface pre-treatments of the substrate, like blast cleaning [203].

Practical studies confirm the influence of surface roughness on coating adhesion [206, 207]. Enhanced adhesion, as an effect of surface roughness, is found to be a result of mechanical interlocking and increased contact area. A higher contact area will increase the bond density between the coating and the substrate, increasing the chemical adhesion. However, this only applies for completely wet surfaces with no air voids [203]. Surface roughness are commonly promoted by surface treatments like etching, polishing and sand- or glass- blasting [208].

The most significant error responsible for poor adhesion and coating failure is poor cleaning [203]. Cleaning of the substrate prior to coating deposition is vital to ensure that the coating adhere well to the substrate without disruption from impurities, e.g. grease, oil, wax. The NORSOK Standard suggests to remove impurities on substrate surfaces by solvent- or alkali- cleaning [209]. Charbonnier *et al.* [210] cleaned polymer substrates by performing an ultrasonic treatment in ethanol.

Characterization of adhesion

Adhesion of epoxy coatings are commonly measured by the tape test (ASTM D3359), also known as the cross hatch test, and the pull-off test (ASTM D4541-02) [211]. The tape test involves the application and removal of a pressure-sensitive tape over a crosshatch pattern made in the coating. During removal, the degree of coating delamination is visually observed. The pull-off test measures the force required to pull off a specific area of coating from its substrate [212]. An advantage of the pull-off test concern its ability to measure both cohesion and adhesion strength; the coatings ability to adhere to itself and to the substrate respectively [213].

2.4.4 Surface roughness

Surface roughness is an essential parameter in the coating industry. As mentioned in Section 2.4.3, increased surface roughness of the substrate has shown to enhance coating adhesion strength. A rougher surface has also shown to promote fouling settlement [214], and is therefore an important consideration regarding antifouling. Scardino *et al.* [215] investigated the fouling behavior of surfaces with nanoscale roughness exposed to various marine environments, and found that a surface roughness at nanoscale experienced remarkably less fouling growth compared to microscale. However, it has been observed that there is no significant correlation between bacterial growth with nanoscale surface roughness [216].

A standard technique for surface roughness measurements include the use of a mechanical profilometer, typically with a resolution of 1 Å [217]. A diamond stylus will trace the material surface lightly and produce a voltage output proportional to the surface roughness. The roughness can be expressed in various parameters, most commonly *Ra* or *Ry*. *Ra* corresponds to the average deviation in peaks and valleys measured from the center axis in the

obtained profile. *Ry* corresponds to the height difference between the lowest valley and the highest peak along the profile [203]. Drawbacks related to profilometer measurements includes (i) the possibility of surface damage during examination and (ii) limited resolution as the stylus tip radius must be small compared to the surface irregularities [217]. Atomic force microscopy (ATM) is also commonly used for surface roughness measurements, with a resolution <0.5 Å [218].

2.4.5 Wettability and surface free energy

Wettability is considered a surface property that plays a vital role in the coating industry. This property has shown to affect the adhesion of coatings to a solid substrate [219]. In addition, studies report that wettability of the coating surface can indicate antifouling behaviour [220]. Wettability is defined as the ability of a liquid to spread over and adhere to a surface. Generally, it is measured by a contact angle which can be directly related to surface energy [221].

Contact angle and surface energy

The contact angle is the angle of a liquid droplet measured where the liquid and a vapor interface meets a solid surface, and defines the wettability of the solid surface. It is found that wetting is favourable at contact angles less than 90°, indicating that a liquid will spread over the surface. A complete wetting is achieved at 0°. Contact angles larger than or equal to 90° indicate poor wetting, and a liquid would typically bead on the solid surface to minimize contact [222]. In theory, a solid surface with a contact angle less than 90° is defined hydrophilic, whilst the surface is defined hydrophobic for surfaces larger than 90°. Superhydrophobic surfaces is a rare phenomenon occurring at high contact angles larger than 150°, which practically indicates that the liquid and the solid surface having barely no contact [223]. Figure 2.12 illustrates the modes of contact angle theory. The contact angle is most commonly measured by the sessile drop mode due to its simplicity. The measurements are performed by depositing a liquid droplet on a horizontal solid surface, and determines the contact angle by image analysis [224]. Generally, an uncertainty of $\pm$1-2° is considered for contact angle measurements [225].

Surface free energy (SFE) is a measure of the surface tension of a solid-vapor interface. Contact angles indicate the wetting of a surface, while SFE give a quantitative measure of the solid-liquid interactions independent of the type of liquid [226]. SFE is described as the excess energy on a solid surface as a result of molecular interactions in the bulk material. The molecular forces in the bulk will influence the SFE; metals typically show high SFE due to strong metallic bonds, while polymers have a tendency of lower SFE due to their weak intermolecular forces [226]. High surface energy is generally associated with high wetting,

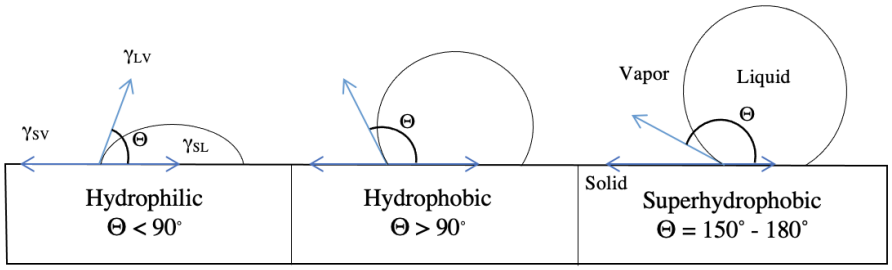

Figure 2.12: Illustration of hydrophilic, hydrophobic and superhydrophobic contact angles formed by the sessile liquid drop mode. The individual interfacial energies, γ, between solid-vapor, liquid-vapor and solid-liquid are illustrated.

hence hydrophilic surfaces. A high surface energy of a solid will pull a liquid down due to strong attractive forces that surpass the surface tension of the liquid droplet, causing high wetting. The opposite phenomenon occur for low surface energies of solids, and is generally associated with hydrophobic surfaces [227].

The relationship between SFE of a solid interface, γ_{sv}, and the contact angle between a three phase boundary between a solid, a liquid and a vapor, θ_Y, can be described by Young's equation,

$$\gamma_{sv} = \gamma_{sl} + \gamma_{lv} \cdot cos\theta_Y \tag{2.10}$$

where γ_{sl} is the interfacial tension between the liquid and the solid, and γ_{lv} is the surface tension of the liquid [228]. It is agreed that γ_{lv} and θ is easily measured. However, several debates concern the determination of γ_{sl}. The Fowkes method shows that γ_{sl} can be calculated as the geometric mean of a dispersive (D) and polar (P) liquid with known surface tension [229],

$$\gamma_{sl} = \gamma_{sv} + \gamma_{lv} - 2(\sqrt{\gamma_{sv}^D \gamma_{lv}^D} + \sqrt{\gamma_{sv}^P \gamma_{lv}^P}) \tag{2.11}$$

The Owens, Wendt, Rabel and Kaelble (OWRK) model can further determine the SFE of a solid by the sessile drop technique. The model uses the contact angle of two liquids with known polar and dispersive components of surface tension, γ_{lv}^P and γ_{lv}^D respectively, to simultaneously solve a set of linear equations. The outcome is a polar and disperse part of the surface energy of the solid, γ_{sv}^P and γ_{sv}^D. The total SFE of the solid is the sum of these two parts [228]. Water is commonly used as the polar liquid in the OWRK method, while both diiodomethane or α-bromonaphthalene have been used as the dispersive liquid [230–232].

The effect of surface roughness and heterogeneities

Young's equation (2.10) determines a unique contact angle θ_Y in static state and does not consider the many metastable states of a droplet on a solid. External factors like surface roughness, surface heterogeneity and physico-chemical interaction between the solid and liquid phase influence the droplet and generate a hysteresis of the contact angle [222]. Contact angle hysteresis can be calculated by measuring the advancing contact angle, θ_a, and the receding contact angle, θ_r, of a droplet under dynamic conditions, and is defined as (2.12):

$$CAH = \theta_a - \theta_r \tag{2.12}$$

Typically, θ_a and θ_r are measured by the needle method by adding water to and withdrawing water from a droplet, respectively. The maximum θ_a and minimum θ_r is obtained when the three-phase contact line is broken [222]. Mcdougall and Ockrent introduced the tilted plate method to measure CAH [233]. The technique is a modification of the needle method, and measures contact angles of the droplet by tilting the solid surface. θ_a and θ_r is defined at the point where the drop just begins to roll. Figure 2.13 shows an schematic of the needle method (a) and the tilted plate method (b) used for CAH measurements.

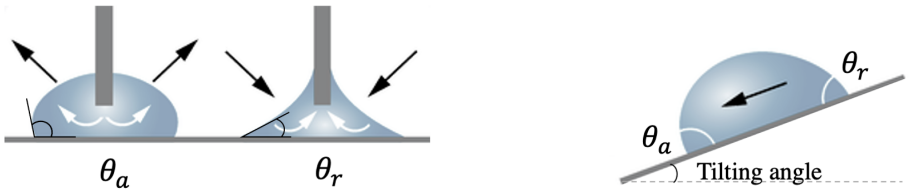

Figure 2.13: Illustration showing the advancing and receding contact angles obtained by (a) the needle method and (b) the tilted plate method for estimation of contact angle hysteresis.

In 1936, Wenzel described the relationship between surface roughness and wettability,

$$cos\theta_m = r\theta_Y \tag{2.13}$$

where r is the roughness ratio between the actual and the projected solid surface area (r>1 for rough surfaces). θ_m is the measured contact angle, while θ_Y is the Young's contact angle (see Equation 2.10) [234]. By this definition, Wenzel states that an increased surface roughness will enhance wettability, implying that an increased surface roughness will make hydrophobic surfaces even more hydrophobic and hydrophilic surfaces even more hydrophilic. However, the surface roughness will have insignificant impact on wettability for roughness values lower than 0.5 μm [234].

Wettability and antifouling

Several studies report that antifouling properties of coatings and membranes can be influenced by their wettability properties. In general, it is believed that surfaces of low surface energy ($\sim$ 25 mN $\cdot$ m) or water contact angles higher than 98° can prevent adhesion of biofouling [235, 236]. However, there are contrary findings on the influence of hydrophilic and hydrophobic surfaces on antifouling performance, and the effect has shown to be complex and highly dependent on the nature of fouling environment and the foulant specie. Polar functional groups, with the ability for strong polar interactions with biomolecules, is absent on low SFE hydrophobic surfaces, resulting in weak adhesion of fouling species. On the contrary, hydrophilic coatings of high SFE (> 70 mN/m) exhibit strong affinity to polar water molecules, and will rather remain in contact with water than biomolecules [60]. Finlay *et al.* [237] showed that low adhesion strength was observed for the fouling algae *Ulva* on substrates of low surface energy, while the diatom *Amphora* was more easily removed on hydrophilic surfaces. Gilron *et al.* [238] confirmed that a modified membrane of lower contact angle, being more hydrophilic, showed higher resistance towards hydrophobic foulants. The same effect was observed in a study performed on a cross-linked polymer film [239]. In a study performed by Ucar *et al.* [240] it was observed that the contact angle hysteresis and antifouling properties were strongly related. The study was performed on hydrophobic surfaces with similar surface energy, and showed that a higher hysteresis favoured easier removal of the green algae *Ulva*.

2.5 Characterization of antifouling properties

This section will address some of the possibilities to investigate antifouling properties of coatings. Previous sections elaborate on the influence of coating properties on antifouling performance of coatings; e.g. antifouling additive distribution within the coating, coating roughness and wettability. This section will present various techniques for evaluating and characterizing the antifouling behavior of coatings by performing antifouling experiments.

2.5.1 Antifouling experiment

Characterization of fouling growth on coating samples are usually performed by exposing the coating to a given marine environment. Commonly, studies are performed by immersing the sample in a marine culture of green algae, single diatoms or bacteria [215, 241]. The system will typically consist of a biofilm reactor with circulating seawater at a salinity of 3.5% and a 12:12 LD light cycle of white fluorescent light [242, 243]. In addition, optimal fouling conditions is normally achieved by adding microalgal culture nutrients or by using a mixed algae culture. A mixed algae culture will simulate a more realistic growth environment,

but the mix of fouling species can complicate the subsequent foulant characterization. Some studies perform antifouling experiments by immersion of samples right into the sea, typically at a depth of three meters [244]. Studies report that immersion periods often range from 4 to 16 days, giving enough growth for primary colonizers to be analyzed [245].

2.5.2 Identifying antifouling

Various techniques exist for characterization of marine growth, like bacteria cells, microalgae and biofilm. The chosen method depends on the selected algae culture; their size, distribution and concentration [246]. Diatoms are commonly studied in relation to antifouling research due to their participation in the initial stage of biofouling [31]. Their adhesion can indicate antifouling in terms of understanding the antifouling performance of specific material surfaces and the adhesion mechanism of certain diatom species [247].

A common approach for diatom characterization concern the use of an optical light microscope where diatoms are directly counted. This technique is considered reliable, with the ability to quantify several diatom species in the same analysis [248, 249]. The appearance of big clusters of algae can generate error as the counted area will not contain a random distribution of algae. In addition, inappropriate counting can occur as the number of algae within each cluster can be difficult to distinguish. Guillard *et al.* [250] estimated that an error of $\pm 20\%$ should be included for a count of 100 cells and $\pm 10\%$ included for 400 counted cells.

The direct count method can also be done by utilizing the fluorescent properties of microalgae, as they contain the autofluorescent pigment chlorophyll. Studies report that bacteria and biofilm can be stained with fluorescent dyes to be better visualized with epifluorescence microscope [246, 251]. A z-stack analysis can be applied in a fluorescence microscope to estimate biofilm thickness [252]. Scanning electron microscope (SEM) is also utilized for direct cell count, with the ability to get detailed information about cell morphology with a resolution at nanometer scale. However, this technique is expensive and not applicable for the count of large numbers of diatoms over a significant large area. In general, SEM is mostly used for qualitative analysis of marine species [253], e.g. by the use of element analysis in an energy-dispersive spectroscopy (EDS) [254].

3 Experimental

The experimental part of this master's thesis was completed by the author, with a schematic overview presented in Figure 3.1. The following sections will thoroughly address the experimental approaches of this thesis, including preparation of epoxy-based coatings with graphene (G) and graphene oxide (GO) as antifouling agents and characterization of relevant coating properties. The practical part is partly inspired by literature, proposals of associate professors and from work of previous master's thesis and from the specialization project conducted by the author [25, 255].

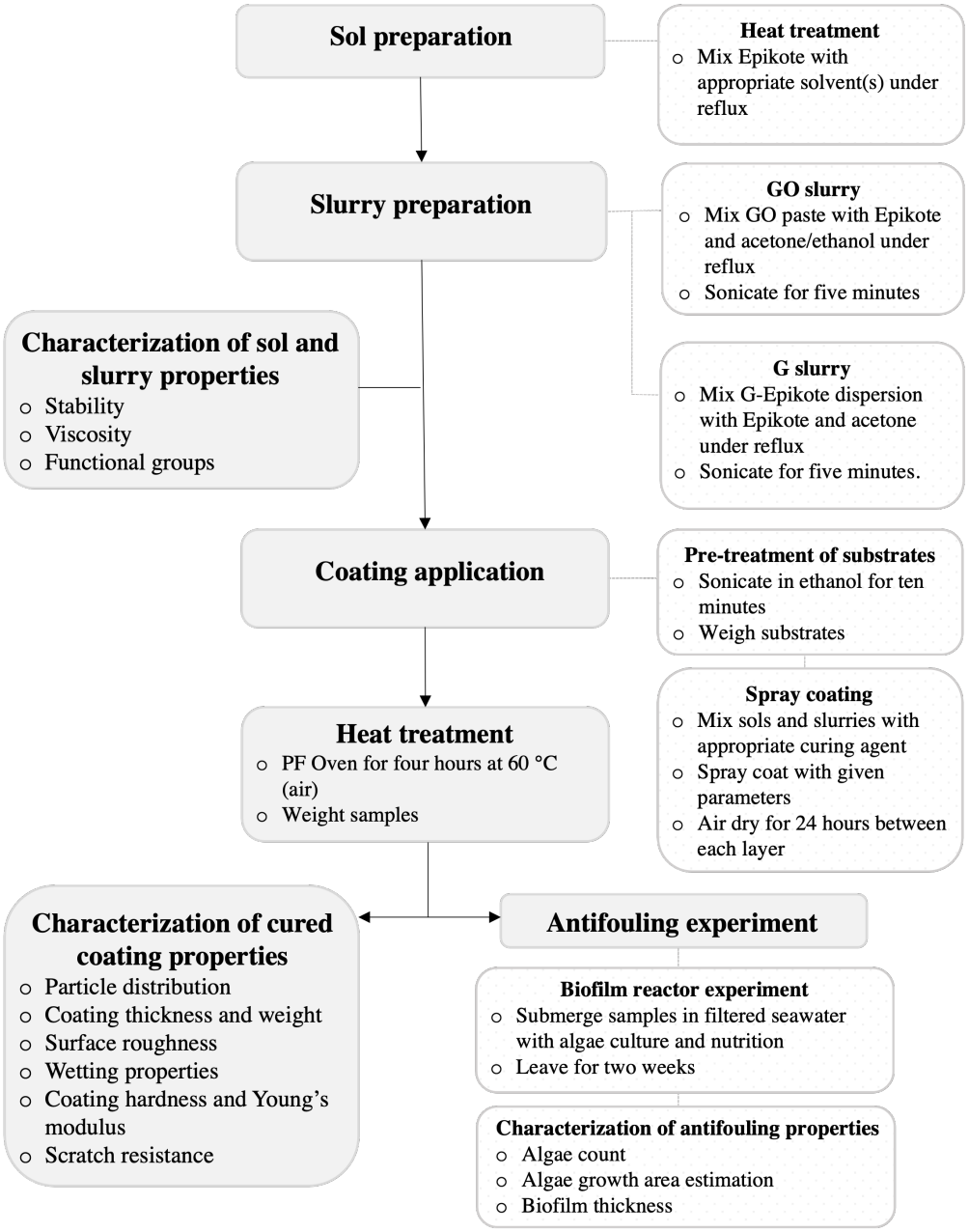

Figure 3.1: Schematic overview of the experimental procedure conducted in this master's thesis.

3.1 Materials and instrumentation

This section presents materials and instrumentation used in the experimental part of this master's thesis. The respective materials are listed in Table 3.1 with relating CAS number, chemical formula, supplier and function.

Table 3.1: Overview of applied chemicals and materials with corresponding CAS number, formula, supplier and a function description.

Chemical	**CAS number**	**Formula**	**Supplier**	**Function**
Acetone (99.00%)	67-64-1	$(CH_3)_2CO$	VWR Chemicals	Solvent
Ethanol (99.97%)	64-17-5	CH_3CH_2OH	VWR Chemicals	Solvent
Epikote Resin 828 (100%)	68038-32-4	$C_{18}H_{12}ClO_3$	CealTech AS	Epoxy resin
Poly(propylene glycol)-bis(2-aminopropyl ether) (100%)	9046-10-0	$CH_3CH(NH_2)CH_2$-$[OCH_2CH(CH_3)]nNH_2$	Sigma-Aldrich	Curing agent
Graphene oxide paste (10 wt% GO)	-	-	CealTech AS	Antifouling agent
Graphene-Epikote dispersion (0.6 wt% G)	-	-	CealTech AS	Antifouling agent
Fragilariopsis (polar diatom)	-	-	CCAP	Algae culture
f/2 + Si Guillard's medium	-	-	CCAP	Nutrition for algae culture
Starter culture (not identified)	-	-	NTNU Sealab	Algae culture
Naturally filtered seawater	-	-	NTNU Sealab	Bioreactor experiment

Table 3.2 gives an overview of the instrumentation and equipment used in the coating preparation and the following characterization techniques.

Table 3.2: Applied instruments with corresponding manufacturer and function description.

Instrument/Equipment	**Manufacturer**	**Function**
Ultrasonic Cleaner USC-TH	VWR	Substrate cleaning and redispersion of slurries
Airbrush Paint Spray	Biltema	Spray coating
Carbolite sol gel furnace	Carbolite Gero	Solvent evaporation of coatings
Bruker Vertex 80v	Bruker	FTIR, ATR analysis
Physica MCR 301 Rheometer	Anton Paar	Viscosity measurements
TI 900 Triboindenter	Hysitron	Hardness and scratch resistance tests
Accutom-5 Cutting machine	Struers	Cutting of coatings on steel substrate
Axio Vert.A1 Inverted light Microscope	Zeiss	Estimation of coating thickness
Drop Shape Analyser DSA100	Krüss	Wettabilily measurements
Dektak 150	Veeco	Estimation of surface roughness
Biofilm reactor	NTNU Workshop	Antifouling experiment
GP-400 Recirculating Waterbath	Neslab	Waterbath for the biofilm reactor experiment
FT 200 Immersion Cooler	Julabo	Cooler for the waterbath
Control device	Heigar	Temperature control of waterbath
Pocket salt meter (PAL SALT)	ATAGO	Seawater salinity measurement
SP8 Confocal Microscope	Leica	Analysis of coating Biofilm thickness estimation
Infinite Focus SL Optical Microscope	Bruker alicona	Characterization of algae culture Estimation of diatom and algae growth Estimation of coating thickness

Table 3.3 gives an overview of the sample abbreviations used in this work. The table lists the weight percentage (wt%) of G and GO and the appropriate solvent(s) associated to each sample. These abbreviations are applied to the description of coating dispersions and cured coating samples. These abbreviations will be consistent throughout the thesis.

Table 3.3: Sample abbreviation of prepared samples with corresponding wt% and solvent. E1: pure epoxy with acetone. E2: pure epoxy with acetone and ethanol. GXXX: samples with 0.XXX wt% G. GOXXX: samples with 0.XXX wt% GO. XXX = 125, 250, 500.

Abbreviation	**wt% Y (Y = G, GO)**	**Solvent**
E1	0 wt% G	acetone
G125	0.125 wt% G	acetone
G250	0.250 wt% G	acetone
G500	0.500 wt% G	acetone
E2	0 wt% GO	acetone, ethanol
GO125	0.125 wt% GO	acetone, ethanol
GO250	0.250 wt% GO	acetone, ethanol
GO500	0.500 wt% GO	acetone, ethanol

3.2 Preparation of epoxy sols

Two epoxy sols (E1, E2) with different combination of solvents were prepared. Table 3.4 lists epoxy sol with appropriate amount of solvent(s), considering a mass ratio of 10:9 epoxy to solvent. Epikote 828 resin, supplied by CealTech AS, was used as epoxy resin. E1 corresponds to epikote sol with acetone, while E2 corresponds to epikote sol with acetone and ethanol (1:1 mass ratio of each solvent in the sol). Calculations are attached in Appendix A. All chemical handling and sol preparations were performed under a fume hood.

Table 3.4: The required mass of respective component in the epoxy sols, with the requirement of a weight ratio of 10:9 mass epoxy compared to mass solvent. E1: pure epoxy with acetone. E2: pure epoxy with acetone and ethanol.

Sol	Chemical	Mass
E1	Epikote	30 g
	Acetone	27 g
E2	Epikote	30 g
	Acetone	13.5 g
	Ethanol	13.5 g

The epoxy sols were prepared by mixing epikote and the appropriate amount of solvent(s) in a beaker. The mixture was stirred by hand for 3 minutes with a metal spatula. Thereafter, the mixture was added to a 250 mL round-bottom flask with a magnet. The flask was placed in a water bath on a heating plate, with a magnetic stirrer, and connected to a condenser. The instrumental set-up is illustrated in Figure 3.2. The epoxy sols were prepared under reflux for 30 minutes with a water bath temperature of 30 °C and a stirring speed of 600 rpm. Subsequently, the sols were transferred to a sealed container and cooled down to room temperature for 10 minutes. The sols were stored in a refrigerator at 4 °C.

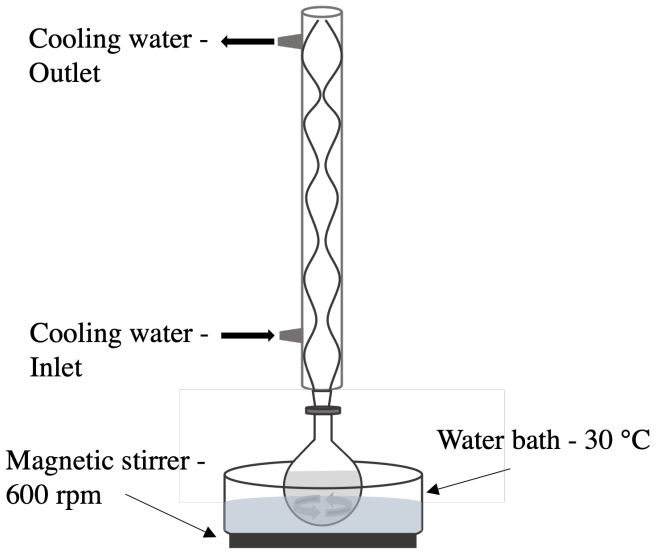

Figure 3.2: Instrument setup for preparation of epoxy sols under reflux.

3.3 Preparation of slurries

This section will in detail describe the procedure for preparing epikote-based slurries with additives of graphene (G) and graphene oxide (GO). G and GO were supplied by CealTech AS in the form of G-Epikote dispersion (0.6 wt% G) and GO paste (10 wt% GO). G and GO slurries were prepared in three concentrations, 0.125 wt%, 0.250 wt% and 0.500 wt% G and GO compared to mass epikote. The slurries were prepared with the required mass listed in Table 3.5, based on calculations found in Appendix A. Acetone was used as solvent in G slurries, while a ratio of 1:1 mass acetone and ethanol was used as solvent in GO slurries. The following procedures and all chemical handling were performed under a fume hood.

Table 3.5: Required mass of each component in preparation of G and GO slurries with 0.125 wt%, 0.250 wt% and 0.500 wt% G and GO compared to mass epikote.

Slurry	**Component**	0.125 wt% [g]	0.250 wt% [g]	0.500 wt% [g]
G slurry	Epikote	20.8662	15.4167	4.5174
	Acetone	23.6842	23.6842	23.6842
	G-Epikote dispersion (0.6 wt% G)	5.4825	10.9649	21.9292
GO slurry	Epikote	26.3150	26.3150	26.3150
	Acetone	11.8421	11.8421	11.8421
	Ethanol	11.8421	11.8421	11.8421
	GO paste (10 wt% GO)	0.3290	0.6579	1.3160

3.3.1 Preparation of GO slurry

The required amounts of GO paste and ethanol were mixed in a beaker. The mixture was stirred by hand with a metal spatula for 5 minutes until only small fragments of GO were visible. Then, acetone and pure epikote were added to the mixture. A magnet was added to the beaker and parafilm was placed on top to prevent solvent evaporation. The dispersion was placed on a magnetic stirrer with a heating function and mixed for 30 minutes at 30 °C with stirring speed on 300 rpm. Subsequently, sonication was performed for 5 minutes in the *Ultrasonic Cleaner USC-TH* to stabilize the dispersion. The slurry was stored in a refrigerator at 4 °C in a airtight bottle.

3.3.2 Preparation of G slurry

The required amounts of 0.6 wt% G-Epikote dispersion and acetone were mixed in a beaker for 2 minutes using a metal spatula. The remaining preparation follows the procedure described in Section 3.3.1 for GO slurries.

3.4 Coating deposition

The prepared sols and slurries were deposited onto two types of substrates; Polyethylene (PE) substrates and DC01 magnetic steel substrates. The following section will in detail describe the coating technique including pre-treatments, preparations and the spray coating procedure.

3.4.1 Pre-treatment of substrate

The fine mechanical workshop of NTNU customized the PE and steel substrates with appropriate specifications, given in Table 3.6. A glass blasting surface treatment was performed on both substrate types by the fine mechanical workshop, with a bead diameter of 0.18-0.30 mm. A pre-treatment of the customized substrates was performed to ensure proper cleaning of the substrate surface prior to coating deposition.

Table 3.6: Specifications of the polyethylene (PE) and steel substrates.

Substrate	Dimensions	Surface treatment
PE	d: 12.6 mm, h: 4 mm	glass-blasted (0.18-0.30 mm)
DC01 steel	10x15x2 cm^2	glass-blasted (0.18-0.30 mm)

PE substrates were cleaned by wiping a duty tissue with ethanol over the substrates. Subsequently, the substrates were put in an airtight bottle containing ethanol. The *Ultrasonic Cleaner USC-TH* was used to sonicate the solution for 10 minutes. After sonication, the substrates were transferred to a clean airtight bottle containing ethanol where they were stored for maximum two days before being coated. Prior to coating deposition, the substrates were left to dry on duty tissues in the fume hood for 10 minutes. A four decimal balance was used to weigh the substrates prior to coating.

The same cleaning procedure was applied for the steel substrates, using acetone as solvent. The cleaned substrates were stored in an airtight bottle containing isopropanol at a maximum of two days before being coated.

3.4.2 Preparation of coating batches

Prior to coating deposition, coating batches with appropriate amount of sol/slurry and curing agent (PPGBAE) were prepared. The molar ratio between epoxy and curing agent was given as 2:1. The corresponding volume of curing agent was found by considering 0.5 g Epikote sol for one coating batch. Table 3.7 lists the appropriate mass of each coating type with

equivalent volume of curing agent, which was found by calculations included in Appendix A.

Table 3.7: Appropriate amount of each component in preparation of one coating batch for application of one layer of coating. E1: pure epoxy with acetone. E2: pure epoxy with acetone and ethanol. GXXX: samples with 0.XXX wt% G. GOXXX: samples with 0.XXX wt% GO. XXX = 125, 250, 500.

Sol/slurry	$\mathbf{m}_{type}$ **[g]**	$\mathbf{V}_{curingagent}$ **[mL]**
E1	0.5000	0.1710
G125	0.5000	0.1710
G250	0.5001	0.1710
G500	0.5001	0.1710
E2	0.5000	0.1710
GO125	0.5003	0.1710
GO250	0.5007	0.1710
GO500	0.5013	0.1710

The sols and slurries were placed in room temperature 30 minutes prior to coating deposition. A four decimal balance was used to measure out appropriate mass of sols and slurries in sample vials. The curing agent was added by using a micro-pipette. Subsequently, the vials were hand-shaken for 10 seconds to ensure proper mixing.

3.4.3 Deposition by spray coating

Coating deposition of prepared sol and slurry batches were performed in a fume hood using a handheld *Airbrush Paint Spray* from Biltema. Table 3.8 lists the relevant coating parameters. The airbrush was connected to a nitrogen gas supply set to 2 bar. A pre-treated substrate was placed in a square of 5x5 cm^2, marked out on an aluminum foil. One coating batch was added to the sample holder of the airbrush. A working distance of 7 cm and working angle of 80 $^\circ$ were applied, and the coating slurry was evenly distributed within the marked square. A demonstration of the coating procedure is illustrated in Figure 3.3. The airbrush was rinsed by filling the sample holder with acetone and spraying it into a beaker for one minute. The rinsing procedure was performed after each coating application. After the final coating deposition, the rinsing procedure was repeated four times.

The coated samples were dried off from underneath with a duty tissue and placed in a sample box with parafilm in the bottom to avoid them from adhering to the sample box. The samples air dried for 24 hours, followed by application of a new coating batch by the procedure described in Section 3.4.3. In total, three coating layers were deposited onto each sample, where one coating batch equals to one layer. After the final application, the samples were air dried for 24 hours and subsequently heat treated.

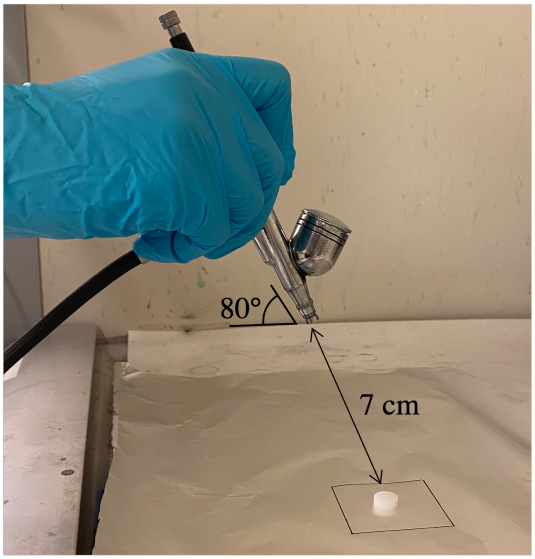

Figure 3.3: Illustration of the spray coating deposition procedure including a working distance of 7 cm and a working angle of 80°.

Table 3.8: Setup parameters for the spray coating procedure.

Parameter	**Description**
Carrier gas	Nitrogen
Gas pressure	2 bar
Working distance	7 cm
Spraying angle	80°
Nozzle diameter	0.3 mm
Area of coating	5x5 cm^2

3.4.4 Heat treatment

All coated samples were heat treated in a *Carbolite Sol Gel Oven* after the final coating batch application to ensure complete solvent evaporation. The samples were placed in alumina boxes with lids partially off. The heat treatment was performed for four hours at 60 °C in air. Subsequently, the samples were left to cool and weighted on a four decimal balance.

3.4.5 Reproduction of G slurry deposition

Qualitative measurements of the surface of cured G250 and G500 coatings, performed by the procedure described in 3.6.1, indicated that their surface appeared non-transparent due to the development of an additional film on the coating surface (see Figure F.2). Therefore, the coating procedure was performed a second time for G slurries, following the procedure in Section 3.4.3.

3.5 Characterization of sol and slurry properties

The following section will describe the procedures for evaluating properties of the prepared epoxy sols and G- and GO- slurries, relevant for antifouling coating applications. Stability, rheology properties and slurry composition were investigated to ensure appropriate coating quality. The characterization techniques were performed on all coating systems prepared, including E1 and E2 sols and on G125, G250, G500, GO125, GO250 and GO500 slurries.

3.5.1 Stability of sols and slurries

The stability of the prepared epoxy sols and G and GO slurries were investigated by image analysis over a specific time span. 10 mL of each sol and slurry were transferred to vials, which were imaged one day, one week and three weeks after preparation. The vials were stored in a refrigerator at 4 °C between each measurement.

3.5.2 Viscosity measurements

Rheology properties of the epoxy sols and G and GO slurries were investigated in an *Anton Paar Physica MCR 301* rheometer with a CC27 geometry and a concentric cylinder attachment. 20 mL of fluid to be analyzed was added to the cylindrical compartment. The measurements were performed at 20 °C with the program presented in Table 3.9, were shear rate was varied from 1 s^{-1} to 500 s^{-1}.

Table 3.9: The measurement program implemented for quantification of rheology properties of prepared sols and slurries performed in the *Anton Paar Physica MCR 301* rheometer.

Step	Shear rate [s^{-1}]	Measurement points	Measurement points duration
1	0	10	30 sec
2	1-500	60	10 sec
3	0	10	30 sec
4	500-1	60	10 sec

The viscosity was estimated by performing a linear regression of decreasing shear rate as a function of shear stress. The uncertainty was extracted from the linear regression, by evaluating the goodness of fit by the R^2 coefficient of determination.

3.5.3 Characterization of functional groups in sols and slurries

A *Bruker Vertex80v* high resolution vacuum FTIR spectrometer with an ATR diamond was used to determine functional groups present in the prepared sols and slurries. Apparatus parameters used for measurements are presented in Table 3.10. Prior to sample measurements, a background scan was run to remove background noise from the obtained spectra. Sample measurements were performed by depositing a droplet of the solution to be measured onto the ATR diamond. A transmittance spectrum of each solution was obtained by running a single line scan. Transmittance spectra of all sols and slurries were obtained one day, one week and three weeks after preparation.

Table 3.10: Apparatus parameters of the *Bruker Vertex 80v* FTIR spectrometer for ATR measurements of prepared sols and slurries.

Parameter	**Description**
Spectrum mode	Transmittance
Wavenumber range	350-4000 cm^{-1}
Scan time	100 s
Vacuum pressure	3.03 hPa
Resolution	4 cm^{-1}
Aperture setting	6 mm
Detector setting	RT-DLaTGS WideRange

3.6 Characterization of surface properties

Surface properties of cured coatings and uncoated substrates were investigated to evaluate the mechanical performance and to investigate surface characteristics relevant for antifouling performance. The properties investigated of each sample type are presented in Table 3.11.

Table 3.11: Investigated properties of all cured coatings and of uncoated polyethylene (PE) and steel substrates. E1: pure epoxy with acetone. E2: pure epoxy with acetone and ethanol. GXXX: samples with 0.XXX wt% G. GOXXX: samples with 0.XXX wt% GO. XXX = 125, 250, 500.

Sample	Substrate	Properties
PE substrate	PE	Roughness, Wettability and SFE
E1, E2	PE	Roughness, Wettability and SFE
G125, G250, G500	PE	Sheet distribution, Roughness, Wettability and SFE
GO125, GO250, GO500	PE	Sheet distribution, Roughness, Thickness, Wettability and SFE
Steel substrate	Steel	Roughness, Wettability and SFE
E1, E2	Steel	Thickness, Hardness, Young's modulus, Scratch Resistance
G125, G250, G500	Steel	Thickness, Hardness, Young's modulus, Scratch Resistance
GO125, GO250, GO500	Steel	Thickness, Hardness, Young's modulus, Scratch Resistance

3.6.1 Sheet distribution

The sheet distribution of G and GO was investigated for all G and GO coatings by the use of the *Alicona Infinite Focus SL* optical microscope. Images were captured with an objective lens of 10x and 50x, at one middle position of each sample.

3.6.2 Coating thickness estimations

The coating thickness of prepared coatings were analyzed by depth range estimations in the *Alicona Infinite Focus SL* optical microscope and by cross-section analysis in the *Zeiss Axio Vert A1* inverted light microscope.

Depth range estimations in optical microscopy

Coating thickness estimations based on depth measurements in the *Alicona Infinite Focus SL* optical microscope were performed for all coatings prepared on PE substrate. The starting point of the depth range measurement was defined at the plane of focus on the interface between the coating and the substrate, while the end point was defined at the plane of focus on the interface between the coating surface and the atmosphere. The depth range measurement was conducted with a 50x objective at five middle positions on each sample. The coating thickness was estimated as an average of the five measurements, and the uncertainty was calculated as a standard deviation of the five measurements.

Cross-section analysis

Coating thickness estimations based on cross-section analysis was performed for all coating systems on steel substrates. Each sample was cut with a *Aluminium Oxide Cut-Off Wheel 40A15* blade in the *Struers Accutom-5* cutting machine. The cut was performed with water cooling and a cutting speed of 0.05 mm/s. The sample was placed in a sample holder and the cross-section was viewed in the *Zeiss Axio Vert A1* inverted light microscope with a 10X/0.25 HD objective. The average coating thickness was estimated by scale measurement at three middle positions of the cross-section. The uncertainty was calculated as a standard deviation of the three scale measurements.

3.6.3 Roughness measurements

Physical surface roughness measurements were conducted on all coating systems and on uncoated PE and steel substrates. The surface roughness measurements were conducted in a *Dektak 150* profilometer. Three measurements were performed on three middle positions of each sample, and the uncertainty was calculated as a standard deviation of the three measurements. Table 3.12 lists the relevant instrument parameters for the profilometer measurements.

Table 3.12: Instrument parameters for surface roughness measurements of a *Dektak 150* profilometer.

Parameter	Description
Scan type	Standard scan
Force	3.0 mg
Sampling duration	60 s
Probe tip radius	12.5 μm
Sampling length	100 μm
Measurement range	524 μm
Resolution	0.056 μm/sample

3.6.4 Wetting properties

Contact angles, surface free energies and water contact angle hysteresis of all coatings and of pure PE and steel substrates were analyzed using sessile drop mode in the *KRÜSS DSA100 Drop Shape Analyzer* with a needle diameter of 0.5 mm. All measurement were conducted in air at room temperature.

Estimation of contact angle and surface free energy

The automation program presented in Table 3.13 was applied to measure the contact angle and surface free energy of all samples. Step four was delayed with 7 seconds to ensure

complete drop formation prior to deposition. The measurements were conducted in three parallels for each sample type, and the uncertainty was calculated as a standard deviation of the three measurements. The baseline was set manually for each measurement.

Table 3.13: The automation program of the Advance software of a *Drop Shape analyzer* utilized for contact angle and surface free energy measurements.

Step	Action	Details
1	Position syringe	Standby | 320 mm/min
2	Position syringe	Dosing | 320 mm/min
3	Dose	5.0 μL | 2.7 μL/s
4	Position syringe	Deposition | 320 mm/min
5	Position syringe	Standby | 320 mm/min
6	Multiple measurements	10 s | 1 fsp

A middle position of each sample was used to measure the contact angle between water and the coating. The water droplet was carefully absorbed with a duty tissue. A new middle position was chosen to measure the contact angle between diiodomethane and the coating. Additional caution was given when using the toxic substance diiodomethane, where an absorption pen was used to remove the chemical quickly after measurements. The surface free energy was measured by applying the measured contact angles in the OWRK model integrated in the Advance software of the DSA instrument. The total surface free energy, and the polar and disperse parts were extracted from the model.

Estimation of contact angle hysteresis

The automation program presented in Table 3.14 was applied to measure the water contact angle hysteresis (CAH) of all coatings and of uncoated PE and steel substrates. The measurements were conducted in three parallels for each sample type, and the uncertainty was calculated as a standard deviation of the three measurements. The CAH was measured at a tilt position of 45° and 90° by computing the difference of the advancing and receding contact angle at the respective tilt positions. The baseline was set automatically for each measurement.

Table 3.14: The automation program of the Advance software of a *Drop Shape Analyzer* utilized for contact angle hysteresis measurements.

Step	Action	Details
1	Position syringe	Standby | 320 mm/min
2	Position syringe	Dosing | 320 mm/min
3	Dose	4.0 μL | 2.7 μL/s
4	Position syringe	Deposition | 320 mm/min
5	Position syringe	Standby | 320 mm/min
6	Tilt	60°/s | 90°
7	Multiple measurements	90 s | 0.5 fsp

3.6.5 Nanoindentation measurements

The nanoindenter of the *Hysitron TI 950 TriboIndenter* was used for estimation of coating hardness, Young's modulus and scratch resistance. The indentations were performed on all coating systems prepared on steel substrates (see Table 3.11), using a Berkovich tip geometry with a tip diameter of 1 μm.

Estimation of coating hardness and Young's modulus

Table 3.15 presents the applied apparatus parameters utilized for hardness and Young's modulus measurements. Six measurements from six middle positions of each sample were performed, with a distance of 5 μm between each position. The output values were obtained by measuring the probe displacement while applying a fixed load. The *Hysitron Triboscan* software of the instrument was used to compute the hardness and reduced elastic modulus of the coatings. The reduced elastic modulus was applied to Equation 2.8, with a Poisson's ratio of 0.35 [190], to extract the Young's modulus. The uncertainty of each sample was calculated as a standard deviation of the six measurements.

Table 3.15: Apparatus parameters applied for hardness and Young's modulus measurements performed in a *Hysitron TI 950 TriboIndenter*.

Parameter	Description
Peak force	4000 μN
Force rate	0.8 mm/s
Hold time	10 sec
No. of parallels	6

Estimation of scratch resistance

A nanoscratch test was performed on all coating systems. Apparatus parameters are listed in Table 3.16. Two measurements were conducted on two middle positions of each sample.

Table 3.16: Apparatus parameters applied for the nano scratch test of prepared coatings performed in a *Hysitron TI 950 TriboIndenter*.

Parameter	Description
Scratch length	10 μm
Peak force	8000 μN
Force rate	160 μN/s
No. of parallels	2

The coefficient of friction (COF) was calculated based on Equation 2.9, and plotted as a function of time (seconds). An average COF for each sample was estimated from the observed steady state of the COF. The uncertainty was estimated as a standard deviation of the average COF obtained from the two measurements of each sample.

3.7 Demonstration of the biofilm production

A biofilm growth demonstration was conducted to evaluate the growth inhibiting properties of G and GO coatings. The following section will explain relevant experimental procedures, including preparation of algae solution and the process description for the biofilm reactor experiment.

3.7.1 Preparation of algae solution

Algae solution was prepared by mixing concentrated algae culture of a given type with sterile f/2 + Si culture medium in a volume ratio of 1:5. The culture medium was made by mixing concentrated medium stocks, supplied by CCAP, with appropriate amount of filtrated, autoclaved sea water, supplied by NTNU Sealab. The relevant amounts of stocks for 1 L of culture medium can be found in Table 3.17.

Table 3.17: The respective stock volumes for preparation of 1 L of culture medium.

Component	Volume [mL]
f/2 + Si culture medium	
Stock 1	1.0
Stock 2	1.0
Stock 3	0.1
Stock 4	1.0
Stock 5	1.0
Natural filtered seawater	995.9

The algae solution was placed in a water bath with a temperature of 14.5 °C and a light cycle of 18 h light and 6 h dark. The water bath contained a *Julabo FT 200 Immersion* cooler, a *Heiger Control unit* thermostat and continuous water flow was used to stabilize the seawater temperature. A *Tetra Whisper 2000* air-pump with an air-stone was connected to the solution. To establish a closed circulation, parafilm was used to cover the opening of the solution container. Culture medium was added to the algae solution in a volume ratio of 1:5 every two months to supply the algae culture with nutrition.

3.7.2 Set-up of the biofilm reactor experiment

The biofilm experiment performed on all prepared coating systems was conducted in a biofilm reactor. The biofilm reactor was prepared by the fine mechanical workshop of NTNU with appropriate dimensions (see Appendix B). The reactor compartment is presented in Figure 3.4 (a), showing the sample holders and the inlet and outlet spouts for the *Iwaki Magnet*

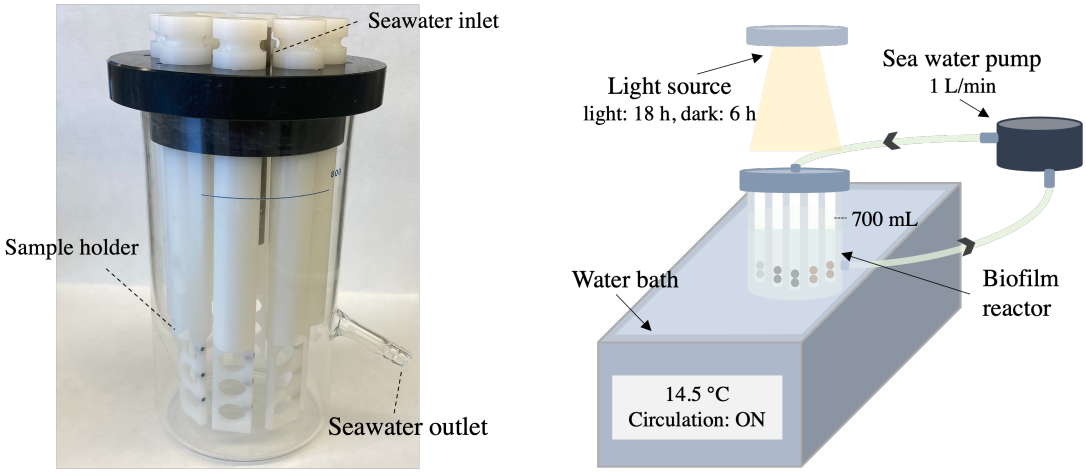

(a) **(b)**

Figure 3.4: Experimental setup for the biofilm reactor experiment showing (a) the bioreactor compartment with sample holders and inlet and outlet spouts for the seawater pump and (b) an illustration of the final set up including the water bath, the biofilm reactor with respective sample holders, the seawater pump and the light source.

Pump MD-6Z sea water pump. The total setup of the biofilm reactor experiment, including the biofilm reactor is presented in Figure 3.4 (b).

Each biofilm reactor experiment required 700 mL fresh algae solution. The respective volumes of algae solution and culture medium for preparation of 700 mL fresh algae solution is given in Table 3.18. The fresh algae solution was prepared on the same day as the start of the biofilm reactor experiment.

Table 3.18: Respective volumes of algae culture and culture medium for preparation of 700 mL algae solution required for each biofilm reactor experiment.

Medium	Volume [mL]
Algae culture	117
Culture medium	583

As displayed in a simplified illustration in Figure 3.4 (b), the bioreactor was submerged in the water bath and connected to the *Iwaki* pump with plastic tubes at a pump speed of 1 L/min. The tubes were tightened with metal clamps around the spout openings. Seawater temperature and light cycles were equal to the one described for the algae solution in Section 3.7.1. Each biofilm experiment was carried out over a period of two weeks. The salinity of the algae solution in the biofilm reactor was measured with a *PAL SALT* refractometer twice a week. At salinity values larger than 4.5 %, distilled fresh water was added to the solution. An overview over the experimental parameters for the biofilm reactor experiment is given in Table 3.19, and a simplified setup is illustrated in Figure 3.4 (b).

Table 3.19: Parameter setup for the biofilm reactor experiment.

Parameter	Description
Algae solution	700 mL
Light cycle	18 h light, 6 h dark
Seawater pump speed	1 L/min
Seawater temperature	14.5 °C
Duration	2 weeks

At completion of the biofilm experiments, the coatings were extracted from the biofilm reactor and moved through fresh sterile water to minimize the occurrence of salt on the coating surface. The coatings were slowly moved over a short distance (2 cm) in the water. Subsequently, the coatings were left to dry in a sample box prior to microscope examination.

3.7.3 Sample overview of the biofilm reactor experiment

The biofilm reactor experiment was performed by placing prepared samples in the sample holders of the biofilm reactor and submersing them into the reactor with the appropriate algae solution. This section will present experimental details regarding the coating systems and algae solutions utilized for each experiment. The biofilm reactor experiments was performed in accordance to the procedure details described in Section 3.7.2.

The biofilm reactor experiment was performed for all coating systems prepared on PE substrates, including E1, E2, G125, G250, G500, GO125, GO250 and GO500 coatings. Uncoated PE substrates were used as reference. One experiment was performed with duplicates of each sample, giving in total 18 samples.

Two experiments were performed, utilizing two different algae cultures. Experiment 1 was run with a mixed algae culture of unknown composition supplied by NTNU Sealab. Experiment 2 was run with the algae culture of Fragilariopsis sp. supplied by CCAP. Correspondence with CCAP implied that the ID of the received culture was wrong. Indeed, the culture was not Fragilariopsis, but possibly a Grammonema specie. Table 3.20 gives an overview of the two biofilm reactor experiments with corresponding coating systems.

Table 3.20: Overview of the experimental set-up of the biofilm reactor experiment. Two samples of all coating types were submerged for two weeks. Uncoated PE substrates were used as reference. Two experiments were performed, using two different algae cultures.

Experiment	Algae culture	Coating type	# samples
1	Mixed culture	Reference	2
		All coating types	2 x 8
2	Single fouling specie	Reference	2
		All coating types	2 x 8

3.8 Characterization of biofilm generation

The following section will explain how the marine growth on samples being immersed in the biofilm reactor was characterized. All samples were characterized in dried condition in a period extending from one day to one month after completion of the biofilm reactor experiment. The marine growth was investigated by estimating the growth of marine species, by considering number of diatoms per mm^2 and by considering area coverage of algae growth in percent.

3.8.1 Investigation of fouling species

The adhesion of various marine species on the submerged samples were investigated. *Alicona Infinite Focus SL* optical microscope was used to captured images of each sample, with a magnification lens of 10X. The various marine species present on the sample surfaces were determined by distinguishing dissimilar morphology and size. The dominating diatom specie, with greatest homogeneous distribution, was chosen for diatom quantification in the direct count method.

3.8.2 Quantification of fouling growth

The growth of marine species on all submerged samples, including E1, E2, G125, G250, G500, GO125, GO250 and GO500 coatings and reference samples, were imaged in an *Alicona Infinite Focus SL* optical microscope, with a magnification of 10X and 50X. The algae growth was quantified by two approaches; by manually counting the number of diatoms on each sample and by estimating the area coverage of algae growth in percent.

Direct count method

Images of the diatom growth was captured by the *Alicona* microscope by using a magnification lens of 50X. Images were obtained at ten middle positions of each sample, as illustrated in Figure 3.5. A total area of 1.66 mm^2 was investigated on each sample, as one middle position corresponds to an area of 0.166 mm^2. The number of the dominating diatom growth specie (see Section 3.8.1) was counted manually for each middle position, and summarized. Subsequently, diatom growth was expressed as diatoms per mm^2. The direct count method was performed on two samples of each sample type, and the uncertainty was measured as a standard deviation of the counted numbers of the two sample types.

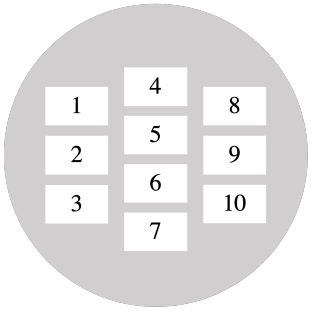

Figure 3.5: Illustrative representation of ten middle positions on a sample. Diatom growth was estimated by the direct count method at each middle position of each sample after the biofilm reactor experiment was performed.

Estimation of area coverage of algae growth in percent

Images of the algae growth was captured by the *Alicona* microscope. The algae growth was investigated at three middle positions of each sample using a magnification lens of 10X. An illustration of the three middle positions at which an image was captured is given in Figure 3.6. A total area of 12.48 mm^2 was investigated on each sample, as one middle position corresponds to an area of 4.16 mm^2.

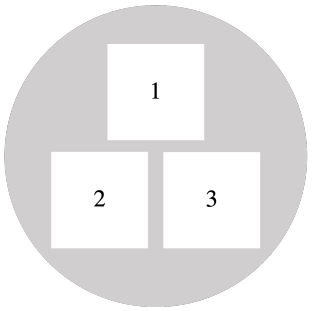

Figure 3.6: Illustrative representation of three middle positions on a sample. An estimation of the diatom covered area was performed at each middle position of each sample after the biofilm reactor experiment was performed.

The *Image J* software was used to estimate the algae growth by means of area coverage for each middle position for each sample. A detailed procedure for the area estimation is attached in Appendix C. Two area estimations were performed for each middle position to minimize measuring errors, and the average value was applied. The uncertainty considered the difference of the two area estimations.

3.8.3 Estimation of biofilm thickness

The biofilm thickness was attempted measured on the submerged samples, including epoxy coatings, G and GO coatings, and on uncoated PE substrates. Depth range measurements were performed in the *Leica SP8* Confocal Microscope with a Plan-Achromat 20x/07 objective. The thickness was investigated in z-stack mode with fluorescence light, by a blue laser (488 nm), with a scan speed of seven seconds. The z-stacks were captured with a tile size of 582.4 μm x 582.4 μm, and eight bits were considered per pixel.

The "begin point" of the z-stack was defined at the interface between the biofilm and the coating. The "end point" was defined at the interface between the biofilm and the atmosphere. The interfaces were found at the depths at which the fluorescent signal from the diatom adhesion faded. This method was also utilized to characterize the layered growth of the diatom species.

4 Results

4.1 Properties of sols and slurries

The stability, rheology properties and composition by means of functional groups of sols and slurries are all significant factors to consider in coating application as they may affect final coating qualities. These properties were investigated for the prepared sols and slurries, and the obtained results are presented in this section.

4.1.1 Sol and slurry stability

The sol and slurry stability of the prepared coating systems are visualized in Figure 4.1, measured over a period of three weeks.

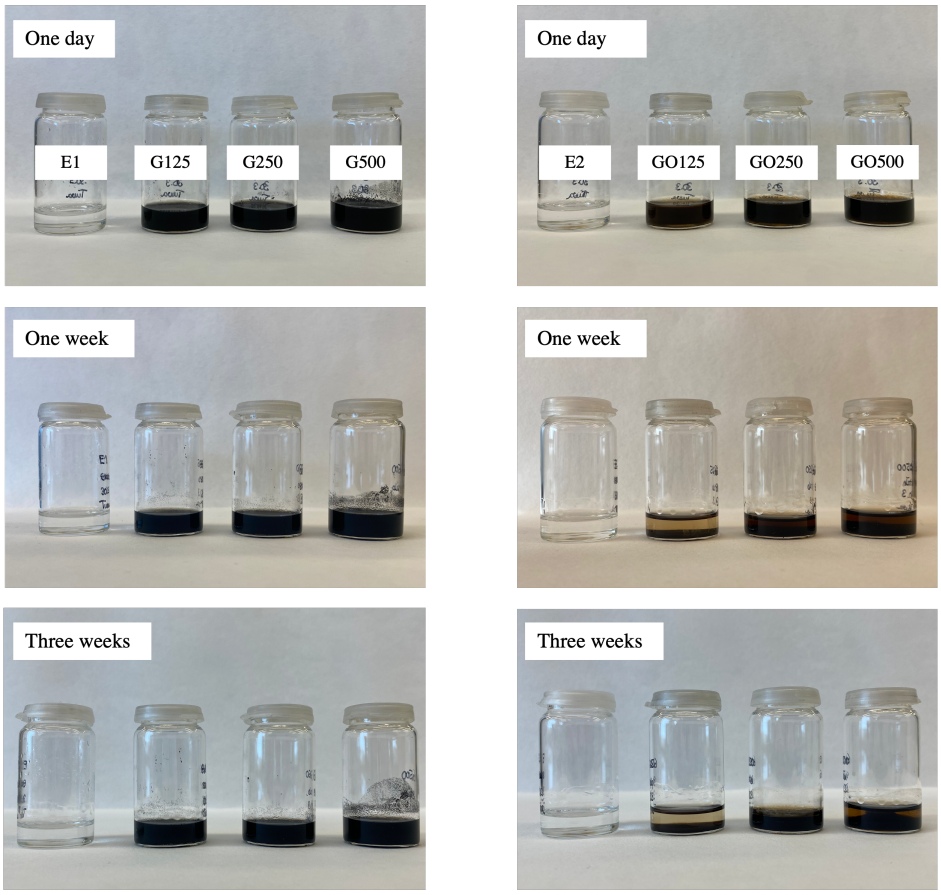

(a) **(b)**

Figure 4.1: Image analysis of sol and slurry stability of (a) E1 sol and G125, G250 and G500 slurries, and (b) E2 sol and GO125, GO250 and GO500 slurries, obtained one day, one week and three weeks after sol and slurry preparation. E1: pure epoxy with acetone. E2: pure epoxy with acetone and ethanol. GXXX: samples with 0.XXX wt% G. GOXXX: samples with 0.XXX wt% GO. XXX = 125, 250, 500.

Both sols, including E1 and E2 sols, appeared stable for the three weeks period with no visible fluid separations within the solutions. The G slurries, including G125, G250, and G500, appeared stable for the three weeks period with no visible sedimentation within the dispersions. The GO slurries, including GO125 and GO500, appeared partly stable as no sedimentation was observed one day after preparation. However, clear sedimentation was observed for the GO slurries after one and three weeks. A damaged lid resulted in solvent evaporation of the GO250 slurry, so the stability analysis was not reflective of this sample.

4.1.2 Rheology properties

Figure 4.2 shows the viscosity as a function of shear rate for all prepared sols and slurries. The E1 and E2 sols, and the GO slurries expressed an overall low dependency of shear rate, and behaved nearly Newtonian. An exception occurred for the GO500 slurry, which experienced a small decrease in viscosity at increasing shear rates. The viscosity of G slurries changed with shear rate, making them non-Newtonian fluids with an increased dependency of shear rate at increasing wt% of G. The viscosity of the G slurries decreased with increasing shear rate, indicating that the slurries behaved shear thinning.

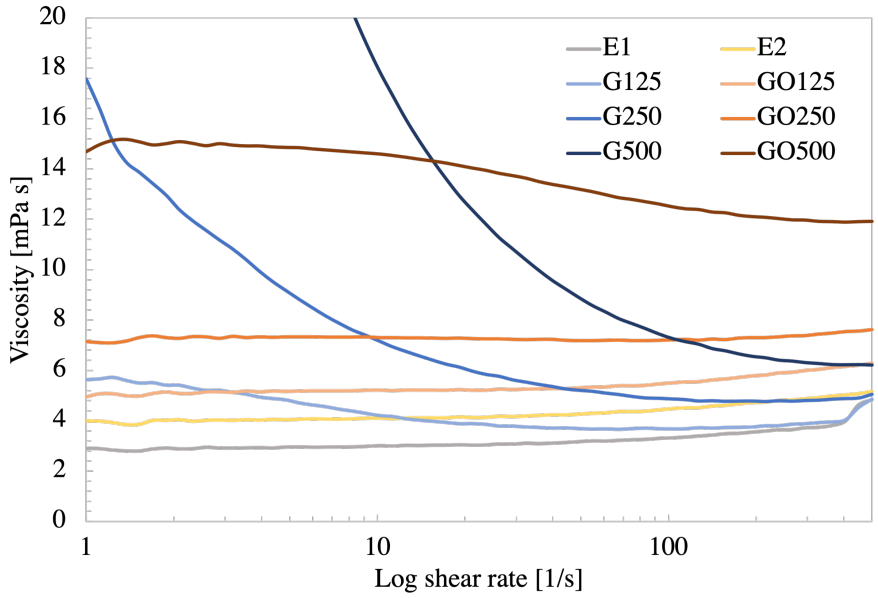

Figure 4.2: Viscosity as a function of logarithmic increasing shear rate measured for prepared E1 and E2 sols and for G and GO slurries. The measurements were performed one week after sol and slurry preparation. E1: pure epoxy with acetone. E2: pure epoxy with acetone and ethanol. GXXX: samples with 0.XXX wt% G. GOXXX: samples with 0.XXX wt% GO. XXX = 125, 250, 500.

Figure 4.3 shows a scatter plot of the obtained viscosities of the prepared sols and slurries, estimated by linear regression of shear stress as a function of decreasing shear rate in logarithmic scale (see Appendix D). Precise values of the obtained viscosity of all samples are attached in Appendix I.1.

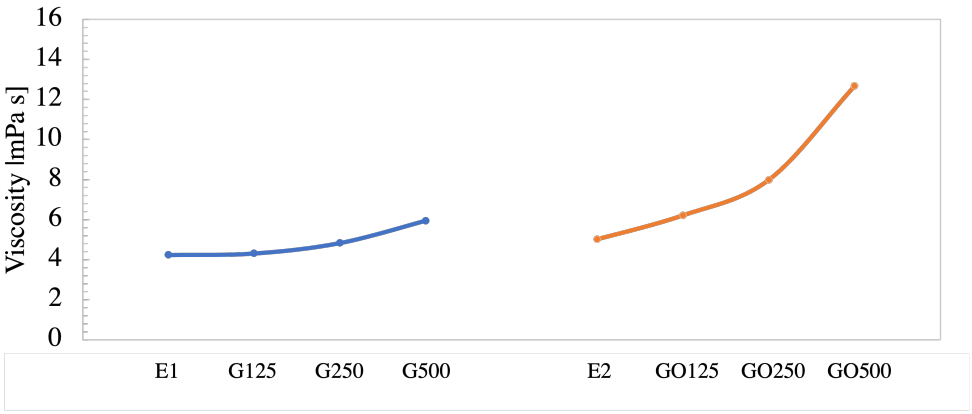

Figure 4.3: A scatter plot of estimated viscosity of prepared sols and slurries calculated by linear regression of increasing shear rate as a function of shear stress (logarithmic scale). E1: pure epoxy with acetone. E2: pure epoxy with acetone and ethanol. GXXX: samples with 0.XXX wt% G. GOXXX: samples with 0.XXX wt% GO. XXX = 125, 250, 500.

The E2 sol and the GO slurries exhibited a higher viscosity compared to the E1 sol and G slurries, respectively. In general, the viscosity of both slurries increased with increasing concentration of antifouling agent. The GO slurries expressed the greatest difference in viscosity with respect to increased concentration of the antifouling agent compared to the G slurries. The GO500 slurry expressed a significantly higher viscosity compared to the other sols and slurries.

4.1.3 Characterization of functional groups

Transmittance spectra obtained from ATR-FTIR analysis will be presented in this section, investigating the composition of each sol and slurry by means of functional groups. All spectra showed a small variation in baseline. This is a result of background noise and instrumental variation, and does not affect the obtained band positions. Figure 4.4 displays the transmittance spectrum of a three weeks old E1 sol and G125, G250, and G500 slurries. The bands with notable intensities are marked in the spectra, and the corresponding functional groups are presented in Table 4.1.

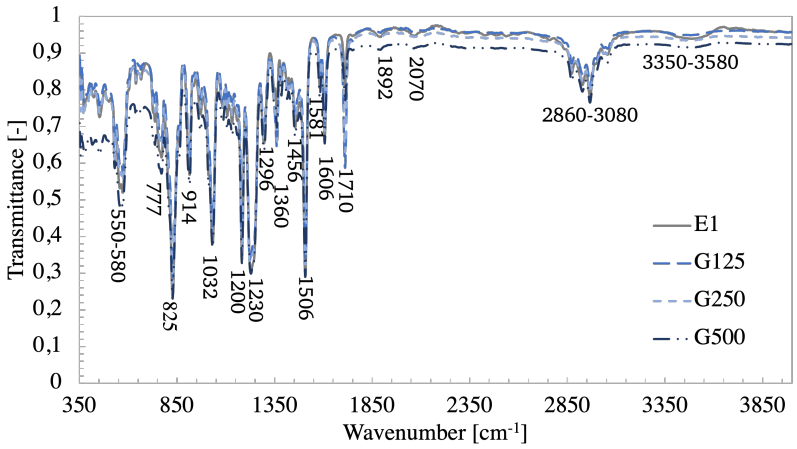

Figure 4.4: Transmittance spectrum acquired from ATR-FTIR analysis of three weeks old E1 sol and G125, G250 and G500 slurries. E1: pure epoxy with acetone. GXXX: samples with 0.XXX wt% G. XXX = 125, 250, 500.

Table 4.1: The wavenumber found in literature [256, 257] and corresponding functional groups presented with experimental wavenumber observed in the spectra for the prepared sols and slurries.

Wavenumber [cm^{-1}]		**Functional group**	**Chemical compound**
Exp.	Lit.		
777	780 $\pm$ 20	C-H bending	-
825	790-840 (medium)	C=C bending	alkene
914	914	C-O stretching	epoxide
1032	1032	C-H stretching	-
1200, 1230	1200-1275 (strong)	C-O stretching	-
1296	1250-1310 (strong)	C-O stretching	aromatic ester
1360	1330-1420 (medium)	O-H bending	alcohol
1456	1450-1465 (medium)	C-H bending	alkane
1506	1500-1550 (strong)	N-O stretching	nitro compound
1581	1580-1650 (medium)	N-H bending	amine
	1566-1650 (medium)	C=C stretching	cyclic alkene
1606	1608	C-C stretching	-
1710	1700-1725 (strong)	C=O stretching	carboxylic acid
1892	1650-2000	C-H bending	aromatic compound
2860-3080	2850-2950	C-H stretching	alkane
	2800-3000 (strong, broad)	N-H stretching	amine
	3020-3080	vinyl =C-H stretching	-
3350-3580	3200-3550 (strong, broad)	O-H stretching	alcohol
	3300-3500 (medium)	N-H stretching	amine

A similar transmittance spectrum is found for E2 sol and GO slurries in Appendix E, in Figure E.1. In general, both spectra showed great overlap between the sols and the different slurries. The strongest difference in band intensity for all spectra are found at wavenumbers

of 1710 cm^{-1}, corresponding to the vibration of carboxylic groups (-COOH), and at 3350-3580 cm^{-1}, corresponding to the vibration of hydroxide groups (-OH). No significant change in composition was found for band intensities lower than 1710 cm^{-1} for all sols and slurries.

The band intensities at 1710 cm^{-1} and at 3350-3580 cm^{-1} are presented in Figure 4.5 and 4.6 respectively, visualizing the change in -COOH and -OH as a function of wt% G and GO and of time (one day, one week and three weeks after preparation). Figure 4.5 (a) shows that the band intensity of 1710 cm^{-1} increased with increasing G content, for a one-day-old slurry. After one week, the band intensity of E1 sol and G125 slurry had increased with respect to time, indicating that the -COOH concentration in these samples had increased. On the contrary, G250 and G500 slurries experienced a decrease in -COOH concentration after one week. Overall, the band intensity at 1710 cm^{-1} was noticeable stronger for E1 and G slurries compared to E2 and GO slurries. Hence, the concentration of carboxylic groups in E1 and G slurries was higher than in E2 and GO slurries. Figure 4.5 (b) shows that there was only a small increase in the 1710 cm^{-1} intensity with increasing GO concentration.

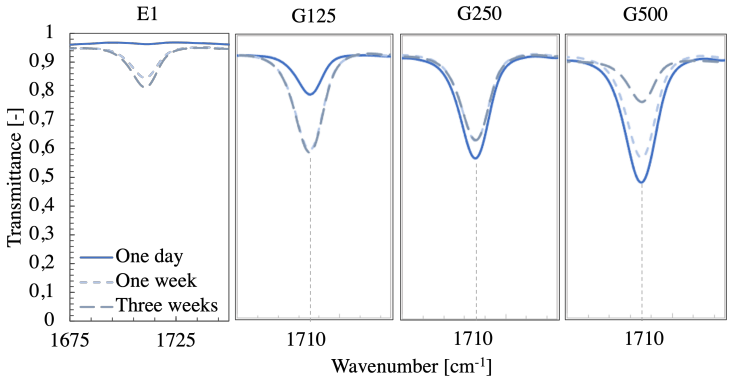

(a)

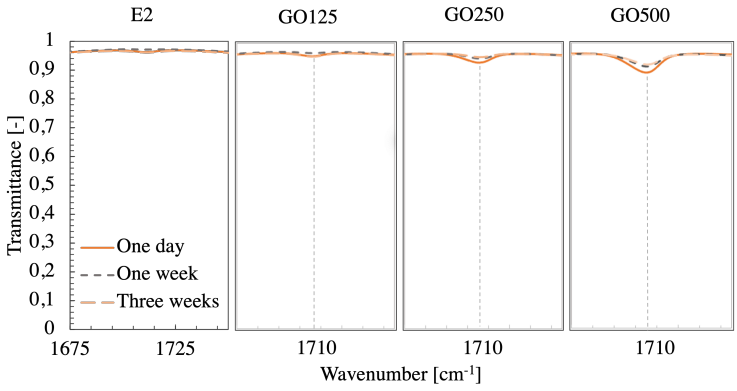

(b)

Figure 4.5: FTIR analysis of (a) E1 sol and G slurries and of (b) E2 sol and GO slurries displaying a section of the transmittance spectra corresponding to the band position of 1710 cm^{-1} (-COOH) for one day old, one week old and three weeks old sols and slurries. E1: pure epoxy with acetone. E2: pure epoxy with acetone and ethanol. GXXX: samples with 0.XXX wt% G. GOXXX: samples with 0.XXX wt% GO. XXX = 125, 250, 500.

Figure 4.6 (a) shows that the E1 sol contained -OH contribution, but that the contribution was absent when G was present in the dispersion. E2 sol showed a similar band intensity as E1 sol at 3350-3580 cm^{-1} (see Figure 4.6 (b)), and stronger bands was observed for increasing GO content. With respect to time, the band intensity of -OH did not show significant time dependency for any of the sols and slurries, and seemed to be unchanged after three weeks.

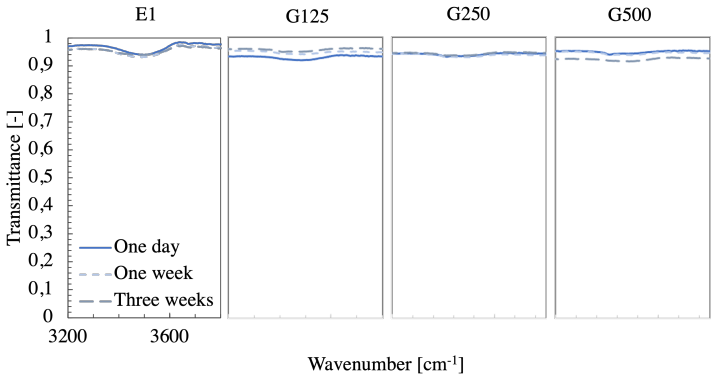

(a)

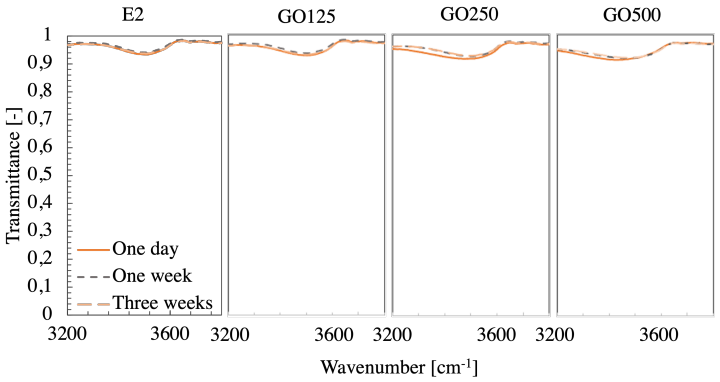

(b)

Figure 4.6: FTIR analysis of (a) E1 sol and G slurries and of (b) E2 sol and GO slurries displaying a section of the transmittance spectra corresponding to the band positions of 3350-3580 cm^{-1} (-OH) for one day old, one week old and three weeks old sols and slurries. E1: pure epoxy with acetone. E2: pure epoxy with acetone and ethanol. GXXX: samples with 0.XXX wt% G. GOXXX: samples with 0.XXX wt% GO. XXX = 125, 250, 500.

The original transmittance spectra for all sols and slurries plotted with respect to time are attached in Appendix E, displayed in Figure E.2. The band intensity of 914 cm^{-1} is identified in each spectra, corresponding to the epoxide group of the epikote epoxy. No significant change was observed for this band intensity in any sol or slurry with respect to time and G and GO concentration. This indicates that the number of epoxide groups, necessary for achieving high degree of cross-linking, was not affected by the addition of G and GO and that no cross-linking took place prior to the addition of curing agent.

4.2 Characterization of cured coating properties

Coating properties were investigated to evaluate the coating quality, antifouling behaviour and mechanical performance relevant for marine applications. This section will investigate sheet distribution of G and GO, coating weight and thickness, surface roughness, wetting properties and mechanical properties including hardness, Young's modulus and scratch resistance.

4.2.1 Sheet distribution of G and GO

The sheet distribution of G and GO within the prepared coatings were investigated, and the obtained distribution within G125 and GO125 coatings prepared on PE substrates are presented in Figure 4.7. The green squares identify G and GO sheets, showing that G and GO appeared evenly distributed within the coatings. The sheet distribution of GO250 and GO500 coatings appeared equally distributed (see Appendix F). The average cluster size of G was estimated to a size less than 8 μm, while the cluster size of GO ranged from 10-30 μm. It was observed that the sheet density increased with increasing GO content.

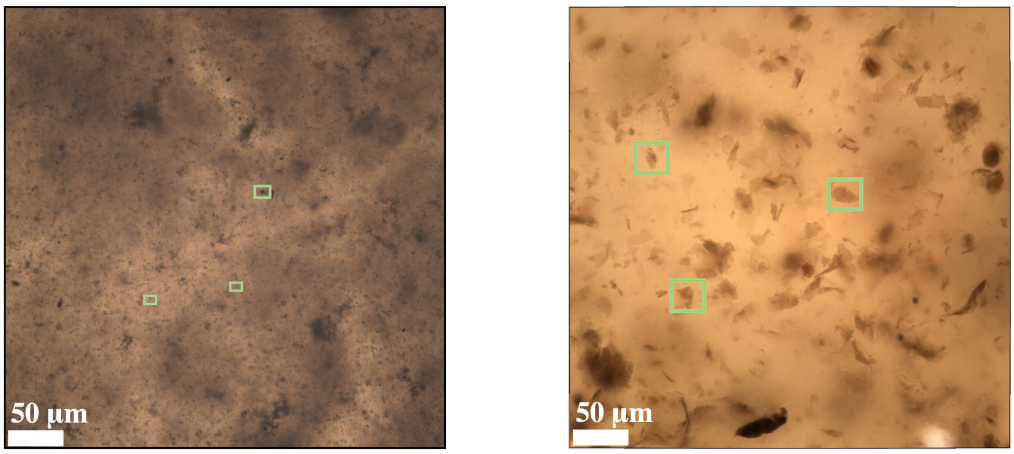

(a) **(b)**

Figure 4.7: Sheet distribution of graphene (G) and graphene oxide (GO) observed in prepared coatings, displayed for coatings containing (a) 0.125 wt% G and (b) 0.125 wt% GO respectively.

The surface of G250 and G500 coatings appeared opaque due to the development of an additional surface film, as shown in Figure F.2. The G coating can be seen in parts of the images, indicating that the observed film is thin. The coating procedure of G slurries was repeated, as described in Section 3.4.5, but similar films were likewise observed for these surfaces. Therefore, the sheet distribution within G250 and G500 coatings were not attainable.

4.2.2 Coating thickness and weight

Coating weight

The estimated coating weight of all prepared coatings prepared on PE substrate are listed in Table 4.2, displayed as an average of nine weighted samples per coating type. The error is a standard deviation of the nine measurements. The measurements show that the coating weight decreased for increasing concentration of antifouling agents. In addition, the pure epoxy coatings, E1 and E2, showed lower coating weight compared to G125 and GO125 coatings, respectively.

Table 4.2: Coating weight of all coatings prepared on polyethylene substrate measured by weighing samples prior to and after coating deposition. E1: pure epoxy with acetone. E2: pure epoxy with acetone and ethanol. GXXX: samples with 0.XXX wt% G. GOXXX: samples with 0.XXX wt% GO. XXX = 125, 250, 500.

Sample	Coating weight [g]
E1	0.059 ± 0.002
G125	0.061 ± 0.004
G250	0.056 ± 0.004
G500	0.053 ± 0.003
E2	0.069 ± 0.008
GO125	0.077 ± 0.005
GO250	0.073 ± 0.005
GO500	0.064 ± 0.005

Coating thickness

The coating thickness of all coatings investigated by depth range measurements and by cross-section analysis are presented in the following section.

Depth range measurement

The thickness of GO coatings prepared on PE substrates is presented in Table 4.3. The thickness of GO coatings varied from 310-480 μm. Overall, the thickness of GO coatings decreased with increasing weight percentage of GO.

Table 4.3: Depth range measurement on GO coatings prepared on polyethylene (PE) substrates for estimation of coating thickness. GOXXX: samples with 0.XXX wt% GO. XXX = 125, 250, 500.

Sample	Coating thickness [μm]
GO125	472 ± 15
GO250	438 ± 13
GO500	311 ± 32

It was not possible to perform depth range measurements on G coatings as the coating surface was not transparent. In addition, depth range measurement was inappropriate for E1 and E2 coatings as these coatings do not contain dyed fillers necessary for reference during measurements.

Cross-section analysis

The coating thickness of coatings prepared on steel substrates, estimated by cross-section analysis, are investigated in the following section. Figure 4.8 displays the cross-section obtained for the G500 and GO500 coatings, showing the measured coating thickness and the three coating layers from the three respective coating depositions. Generally for the E2, G and GO coating systems, it was observed that each coating layer was evenly deposited. In addition, no air pockets were observed on the interface between the first coating layer and the substrate surface. Cross-section analysis of the E1 coating (see Appendix G.1) showed that the first deposition layer was significantly small compared to the second and third layer.

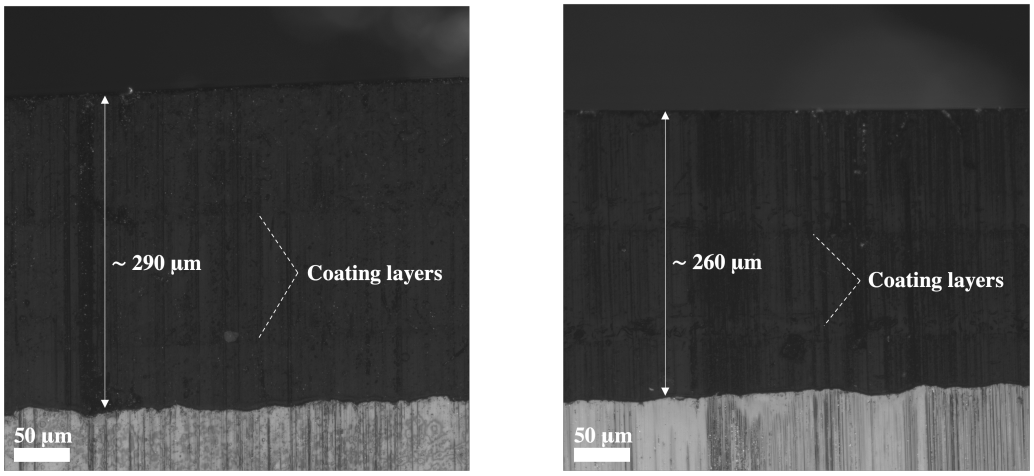

(a) **(b)**

Figure 4.8: Cross-section of (a) G500 and (b) GO500 coatings prepared on steel substrate, showing the estimated coating thickness and the respective coating layers. G500 and GO500 corresponds to epoxy coatings with 0.500 wt% graphene (G) and graphene oxide (GO) respectively.

The thickness of the epoxy coatings and the G and GO coatings prepared on steel substrates are presented in Table 4.4. Overall, the pure epoxy coatings, E1 and E2, showed smaller thickness compared to G125 and GO125 coatings, respectively. The thickness of G coatings showed small variations in thickness with increasing wt% of G. In addition, it was observed that the GO coating with highest GO concentration showed a significant decrease in coating thickness compared to its respective coatings. This effect was not observed for G coatings.

Table 4.4: Estimation of coating thickness of all coating systems prepared on steel substrate based on cross-section analysis. E1: pure epoxy with acetone. E2: pure epoxy with acetone and ethanol. GXXX: samples with 0.XXX wt% G. GOXXX: samples with 0.XXX wt% GO. XXX = 125, 250, 500.

Sample	Coating thickness [μm]
E1	187 ± 6
G125	267 ± 6
G250	290 ± 10
G500	277 ± 23
E2	303 ± 6
GO125	410 ± 1
GO250	400 ± 10
GO500	257 ± 6

There is a significant difference in coating thickness between G and GO coatings, assumed to be a results of changing to a new spray coater for application of E2 and GO coatings. This was clearly visible when comparing E1 and E2 coatings with image analysis, attached in Appendix G.

4.2.3 Estimation of surface roughness

Table 4.5 shows the estimated surface roughness of all coatings and of uncoated PE and steel substrates displayed as a Ra value, measured over a sample length of 100 μm.

Table 4.5: Estimated surface roughness of all samples including uncoated polyethylene (PE) and steel substrates, measured at a sample length of 100 μm. E1: pure epoxy with acetone. E2: pure epoxy with acetone and ethanol. GXXX: samples with 0.XXX wt% G. GOXXX: samples with 0.XXX wt% GO. XXX = 125, 250, 500.

Sample	Surface roughness, Ra [nm]
E1	8 ± 3
G125	2 ± 1
G250	9 ± 4
G500	4 ± 1
E2	7 ± 1
GO125	12 ± 5
GO250	21 ± 5
GO500	39 ± 18
PE	1263 ± 672
Steel	776 ± 291

Overall, the coated samples expressed significantly lower roughness compared to uncoated substrates, ranging from 1-60 nm. The uncoated substrates expressed surface roughness of

about 1 μm. The addition of G in epoxy coatings did not seem to affect the surface roughness, as similar values were estimated for pure epoxy coatings and for G coatings. The addition of GO in epoxy coatings showed a significant effect on surface roughness, where GO coatings exhibited a higher roughness compared to the other coatings. In addition, the Ra value of GO coatings seemed to increase with increasing wt% of GO.

4.2.4 Wetting properties

The estimated wetting properties of prepared coatings and of uncoated substrates, including contact angles, surface free energies and contact angle hysteresis, are presented in the following section.

Mean water contact angle

The mean water contact angles measured for all prepared coatings and uncoated PE and steel substrates are displayed as a bar chart in Figure 4.9, presenting the water CA as a function of G and GO content. Exact values are presented in Table 4.6. All of the coatings, as well as the uncoated steel substrate, expressed water contact angles lower than 90° and were hydrophilic. On the contrary, the uncoated PE substrate expressed a water contact angle higher than 90° and was hydrophobic. Overall, only small changes in CA were visible with respect to wt% G and GO, showing a tendency of increasing water contact angles for increasing wt% of G and GO. An exception was found for the GO500 coating, showing a decrease in CA compared to the GO250 coating. All coatings expressed water CA in the range of 58-63 °.

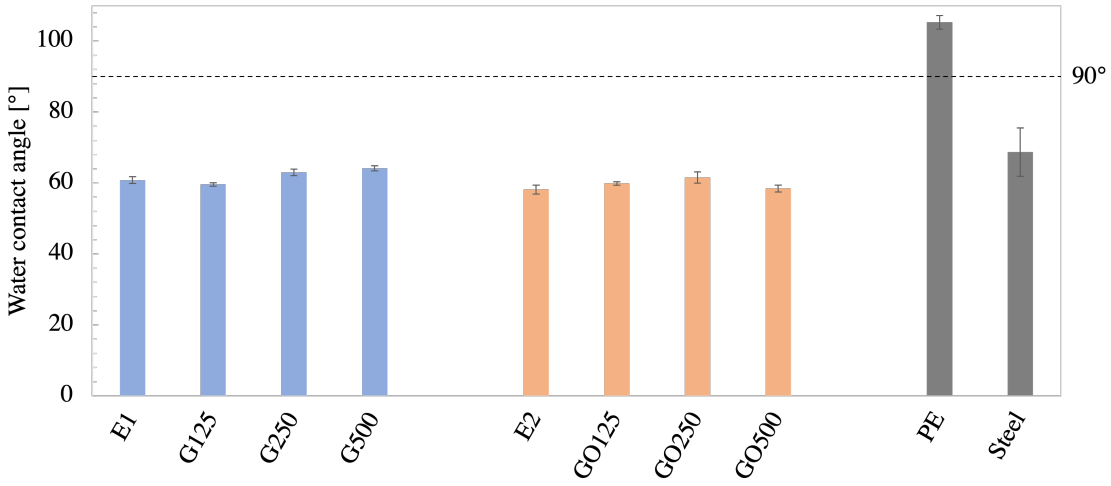

Figure 4.9: Bar chart of the mean water contact angles all prepared coatings and of uncoated polyethylene (PE) and steel substrates. E1: pure epoxy with acetone. E2: pure epoxy with acetone and ethanol. GXXX: samples with 0.XXX wt% G. GOXXX: samples with 0.XXX wt% GO. XXX = 125, 250, 500.

Surface free energy

The surface free energies (SFE) of the all coatings prepared on PE substrate and of uncoated PE and steel substrate are shown in Figure 4.10, measured with water and diiodomethane as liquids. The SFE consists of a polar part, displayed as striped line bars, and a disperse part, displayed as continuous bars. In general, all coatings showed higher SFE compared to the uncoated substrates. Uncoated PE substrate expressed the lowest SFE, with no significant contribution from the polar part. SFE did not express a consistent trend with increasing G and GO content.

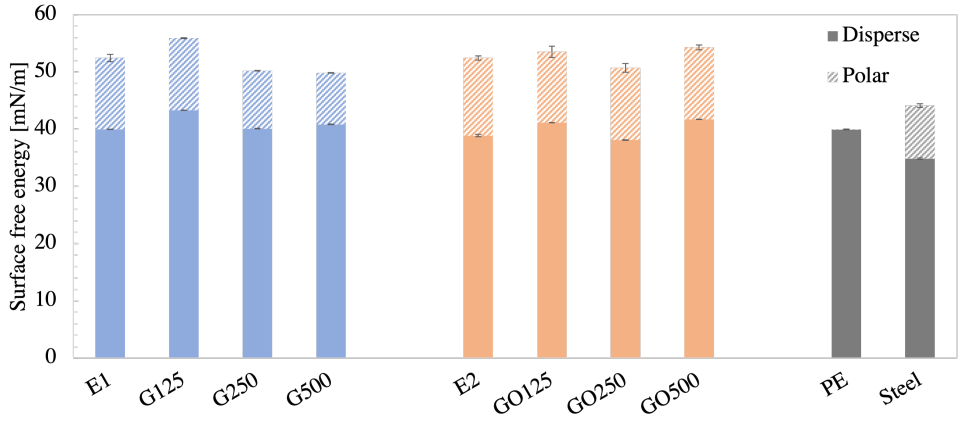

Figure 4.10: Bar chart of the surface free energy of all prepared coatings and of uncoated polyethylene (PE) and steel substrates, measured with water and diiodomethane as liquids. E1: pure epoxy with acetone. E2: pure epoxy with acetone and ethanol. GXXX: samples with 0.XXX wt% G. GOXXX: samples with 0.XXX wt% GO. XXX = 125, 250, 500.

Table 4.6 gives an overview of the measured contact angles of water and diiodomethane and the calculated surface free energy of prepared coatings and on uncoated substrates. All coatings express SFE of about 50-56 mN/m. As expected from literature [227], the sample with highest CA, being the uncoated PE substrate, showed the lowest SFE. This trend is not observed within the prepared coatings.

Table 4.6: The contact angles of water and diiodomethane and corresponding total surface free energies (SFE) estimated for all coatings and polyethylene (PE) and steel substrates. E1: pure epoxy with acetone. E2: pure epoxy with acetone and ethanol. GXXX: samples with 0.XXX wt% G. GOXXX: samples with 0.XXX wt% GO. XXX = 125, 250, 500.

Sample	Water CA [°]	Diiodomethane CA [°]	SFE [mN/m]
E1	60.8 ± 1.0	39.2 ± 0.1	52.5 ± 0.7
G125	59.6 ± 0.5	32.1 ± 0.1	55.9 ± 0.1
G250	63.0 ± 0.9	39.0 ± 0.1	50.2 ± 0.1
G500	64.2 ± 0.8	37.5 ± 0.1	49.9 ± 0.1
E2	58.2 ± 1.2	41.4 ± 1.3	52.6 ± 0.6
GO125	59.9 ± 0.5	36.9 ± 0.1	53.5 ± 1.0
GO250	61.6 ± 1.2	42.9 ± 0.1	50.7 ± 0.8
GO500	58.4 ± 1.0	35.6 ± 0.1	54.3 ± 0.5
PE	105.3 ± 2.0	38.3 ± 0.3	40.0 ± 0.1
Steel	68.7 ± 6.8	48.6 ± 0.3	44.1 ± 0.4

Contact angle hysteresis

The water contact angle hysteresis (CAH) was measured for all prepared coatings and for uncoated PE and steel substrates. The roll-off angle, which normally illustrates the CAH, was not attainable as the droplet did not roll off during measurements. Instead, the CAH was obtained by measuring the advancing and receding contact angle at 45° and 90°, as presented in Figure 4.11. All samples expressed CAH from 10-14° at 90° tilt angle. Generally, the E2 coating showed a significantly higher CAH compared to the E1 coating. No obvious trends regarding CAH was observed with respect to content of G and GO, when uncertainties were considered. However, GO coatings show a tendency of reduced CAH at increasing GO content.

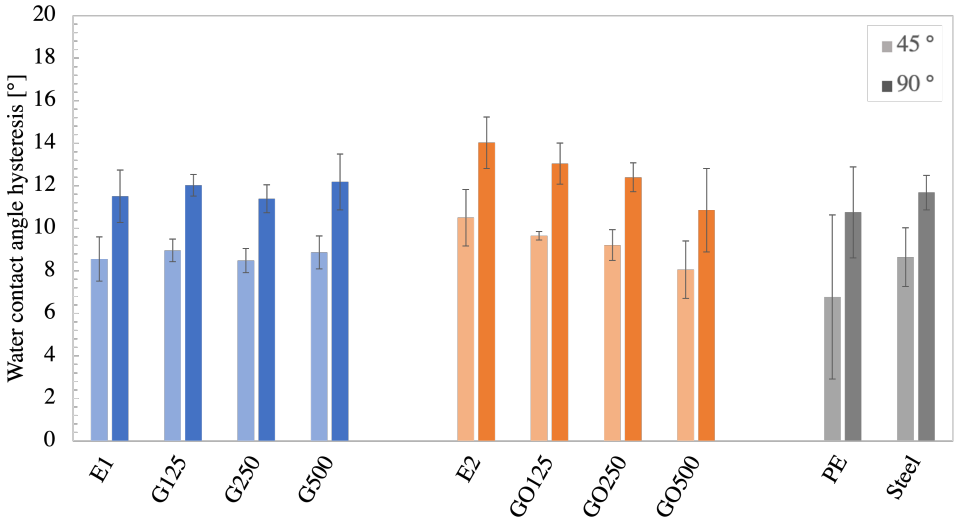

Figure 4.11: Bar chart of the water contact angle hysteresis of all prepared coatings. E1: pure epoxy with acetone. E2: pure epoxy with acetone and ethanol. GXXX: samples with 0.XXX wt% G. GOXXX: samples with 0.XXX wt% GO. XXX = 125, 250, 500.

4.2.5 Coating hardness and Young's modulus

The estimated value of coating hardness and Young's modulus of epoxy coatings and of G and GO coatings are presented in Figure 4.12. Exact values are attached in Appendix I.2, in Table I.2. The nanoindentations were performed with penetration depths ranging from 900-1000 nm. All coatings expressed hardness values ranging from about 190-215 MPa and Young's modulus from 3600-4250 MPa, similar to other nanoindentation studies of bisphenol A based epoxy coatings [191]. GO250 and GO500 coatings showed higher hardness values compared to E2 and GO125 coatings, indicating that GO have an enhancing effect on hardness. An initial increase in hardness and decrease in Young's modulus were observed for G125 coatings with respect to pure epoxy coatings. For higher weight ratios of G, the hardness and Young's modulus appeared unchanged. No significant trend was observed for the estimated Young's modulus of GO coatings with respect to wt% GO. However, GO500 coatings expressed a higher Young's modulus compared to pure epoxy coatings, of about 4150 MPa. Overall, GO coatings expressed a higher Young's modulus compared to G coatings.

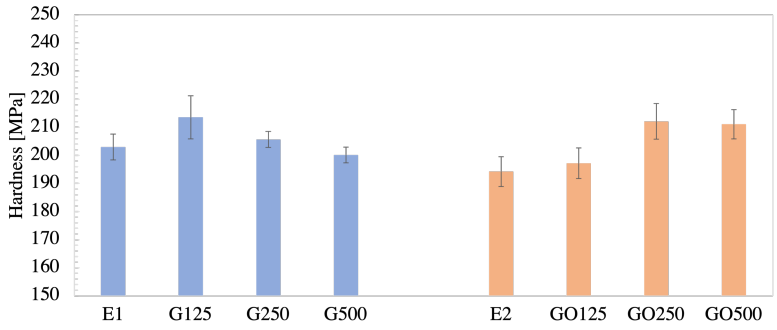

(a)

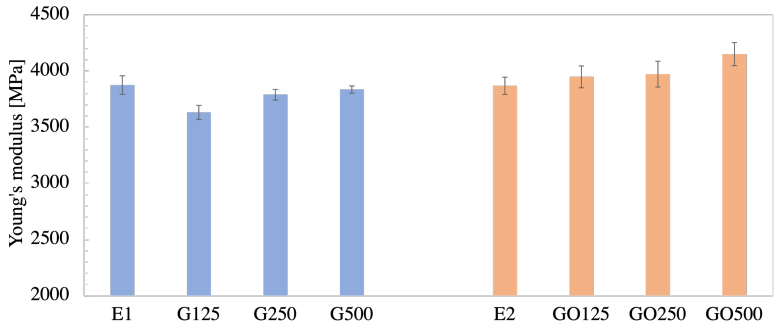

(b)

Figure 4.12: Bar chart of obtained values of (a) hardness and (b) Young's modulus of all coating systems prepared on steel substrates, estimated by nanoindentation measurements in a *Hysitron Triboscan* nanoindenter. E1: pure epoxy with acetone. E2: pure epoxy with acetone and ethanol. GXXX: samples with 0.XXX wt% G. GOXXX: samples with 0.XXX wt% GO. XXX = 125, 250, 500.

4.2.6 Scratch resistance

A nanoscratch test was performed on all coatings prepared on steel substrate, and the obtained output values of lateral force as a function of scratch time are given in Figure 4.13. Two measurements were performed on each sample, and the presented curves are an average of these two measurements. No disruption in the lateral force curve was observed for any of the coatings, indicating that no coating failure occurred during scratching [187].

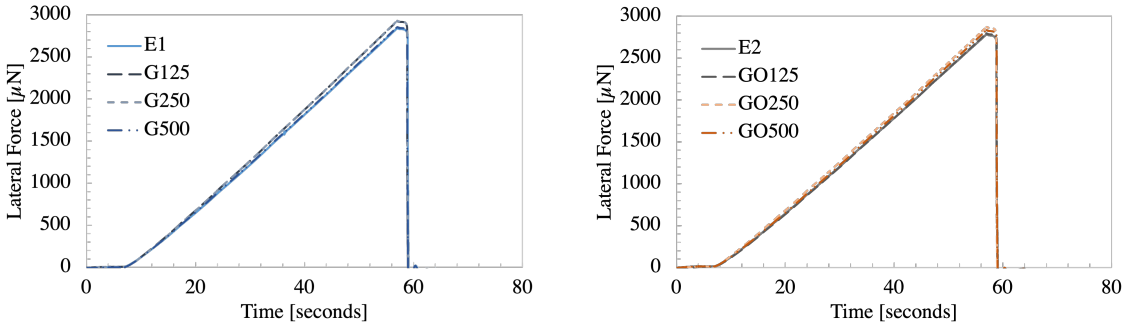

Figure 4.13: Lateral force as a function of time measured from a nanoscratch test with progressively increasing normal force. The test was performed over a scratch length of 10 μm with maximum normal force of 8000 μN. The figure shows (a) lateral force versus time for E1 and G coatings and (b) lateral force versus time for E2 and GO coatings. E1: pure epoxy with acetone. E2: pure epoxy with acetone and ethanol. GXXX: samples with 0.XXX wt% G. GOXXX: samples with 0.XXX wt% GO. XXX = 125, 250, 500.

An average coefficient of friction (COF) was estimated from the scratch tests of each coating. The COF was estimated as an average over steady state, ranging from 30 seconds to 50 seconds (see Appendix H for substantiation). The average COF estimated for each coating type is presented in Figure 4.14.

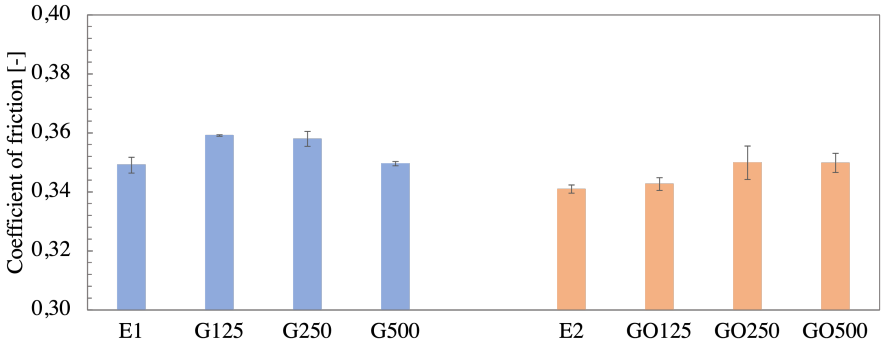

Figure 4.14: The coefficient of friction (COF) estimated for all coatings prepared on steel substrate. COF was estimated as normal force over lateral force of a nanoscratch test performed in the *Hysitron* Nanoindenter. E1: pure epoxy with acetone. E2: pure epoxy with acetone and ethanol. GXXX: samples with 0.XXX wt% G. GOXXX: samples with 0.XXX wt% GO. XXX = 125, 250, 500.

Overall, a small increase in average COF was observed for coatings with antifouling agents compared to pure epoxy coatings. However, the G coatings showed a tendency of exhibiting a reduced average COF with increasing content of G. GO coatings showed an overall tendency of exhibiting a higher average COF for increasing content of GO.

4.3 Investigation of antifouling properties

The antifouling behaviour of G and GO in epoxy-based coatings is investigated in the following section. First, the different fouling species present on the immersed samples was characterized with respect to the two biofilm reactor experiments. Second, algae growth on immersed samples was quantified by two approaches. The direct count method counted the number of diatoms, of one specific specie, present on all samples. The area estimation method estimated the area coverage of algae growth in percent, including all diatom species, present on the samples. Biofilm reactor experiments performed with algae culture 1 and 2 are presented consecutively in each subsection.

The direct count method was performed over a total area of 1.66 mm^2 per sample, corresponding to a coverage of 2% with respect to total measurable area of the sample, eliminating edge defects. The quantification of algae growth performed by area estimation considered a total area of 12.5 mm^2 per sample, corresponding to a coverage of 14% with respect to the total measurable area of the sample, eliminating edge defects.

4.3.1 Characterization of algae growth on immersed samples

Algae culture 1

Figure 4.15 shows the observed algae growth from the biofilm reactor experiment performed with algae culture 1, exemplified on an E1 coating sample. Three different diatom species were found on all coating systems, marked with numbers (1, 2 and 3) in the figure. Marine organic matter, appearing as white material, was also observed on all coatings. Accumulation of diatoms were enhanced in these regions.

It was observed that the diatom species marked in square 1 and 3 showed a great tendency to grow in clusters on all samples. The diatom specie marked in square 2 was the dominant specie on all samples, and showed highest tendency of a homogeneous distribution. Hence, this specie was chosen for application in the direct count method. The dominant diatom specie (no. 2) appeared oval with a slight variation in size. The diatom length and width varied from 8-15 μm and 5-7 μm respectively. The size appeared to be independent with respect to type of growth surface. The diatoms primarily occurred homogeneously distributed

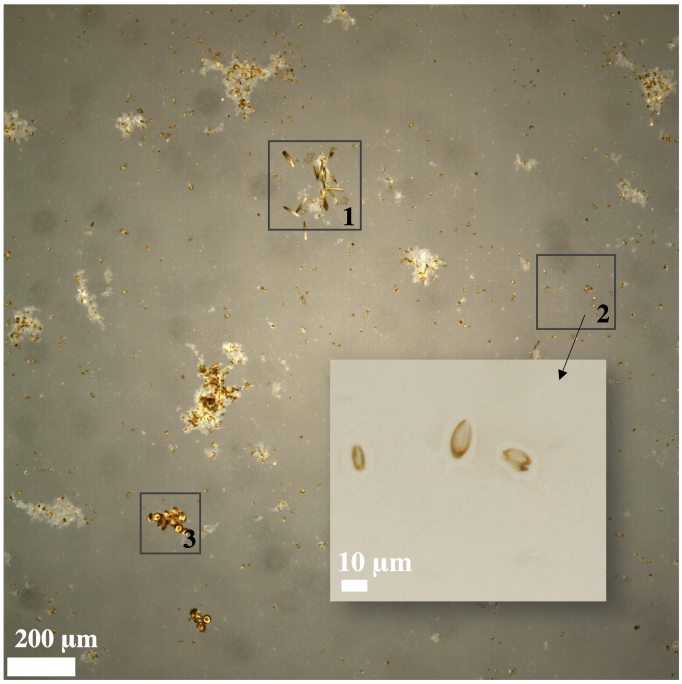

Figure 4.15: Algae growth from algae culture 1 observed on an E1 coating after submersion. The different diatom species observed on the coating surface are marked in numbered squares. Square 2 marks the diatom specie used for quantification in the direct count method. E1: pure epoxy with acetone.

as singles, but did also appear in clusters on all sample surfaces. The growth of diatom clusters were observed to be independent of the type of sample surface.

Algae culture 2

Figure 4.16 shows the observed algae growth from algae culture 2, exemplified on an E1 coating sample. Overall, two diatom species were observed on all submerged samples as illustrated by the numbered squares (1 and 2) in Figure 4.16. Marine organic matter appearing as white material was barely present on the immersed samples. It was observed that the diatom specie marked in square 2 was dominant on all submerged samples, and this specie was therefore chosen for application in the direct count method.

The diatom specie of square 2 occurred homogeneously distributed as singles on all submerged coatings, with minimal cluster growth. The reference sample showed a significantly higher degree of cluster growth. The diatom morphology appeared oval with an average length of 10 μm and width of 3 μm, which appeared to be independent with respect to type of sample surface.

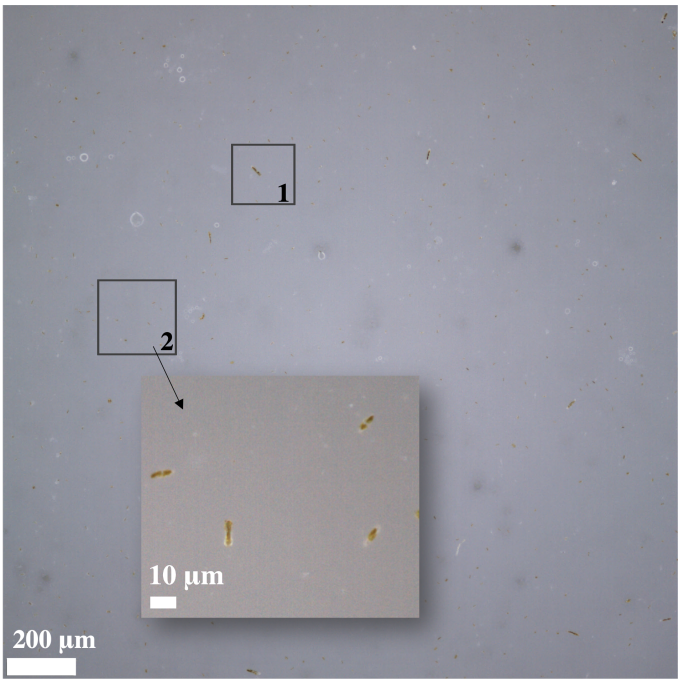

Figure 4.16: Algae growth from algae culture 2 observed on an E1 coating after submersion. The different diatom species observed on the coating surface are marked in numbered squares. Square 2 marks the diatom specie used for quantification in the direct count method. E1: pure epoxy with acetone.

4.3.2 Quantification of marine growth

The quantification of marine growth on submerged samples is presented below, with respect to number of diatoms per mm^2 and the area coverage of total algae growth. Exact values related to the bar charts displayed in this section are attached in Table I.5 in Appendix I.4.

Algae culture 1

Figure 4.17 shows the number of diatoms per mm^2 observed on each sample type estimated by the direct count method for the biofilm reactor experiment performed with algae culture 1. The counted diatom specie was determined in Section 4.3.1 under **Algae culture 1**, and recognized based on size evaluation and diatom morphology. E1 and E2 coatings exhibited similar diatom growth as the reference sample. The coatings containing G and GO experienced significantly less diatom adhesion compared to uncoated PE substrates and pure epoxy coatings. For both G and GO systems, G500 and GO500 coatings express better antifouling performance with respect to diatom adhesion compared to G125 and GO125 coatings, respectively. Overall, the direct count method for the experiment with algae culture 1 showed a tendency of increased antifouling performance of G and GO coatings for increasing wt% of G and GO. However, the presence of overlapping uncertainties between G125 and G250 and between GO125 and GO250 makes this indication weak.

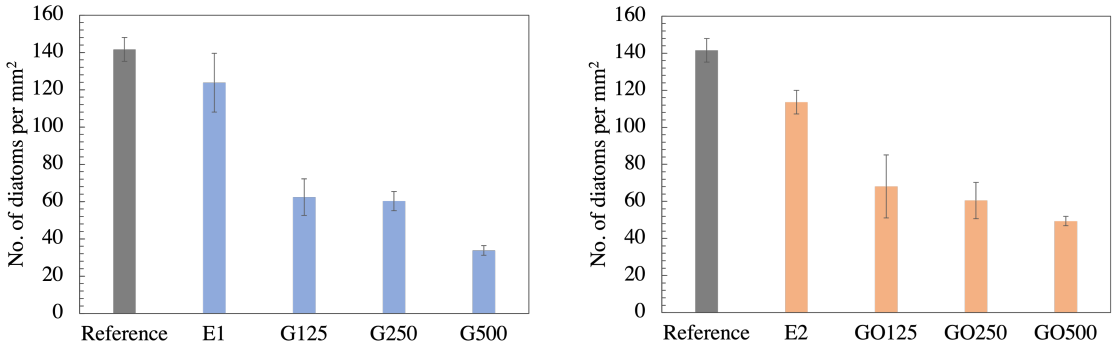

Figure 4.17: Bar chart showing number of adhered diatoms per mm^2 of (a) E1, G125, G250 and G500 coatings and of (b) E2, GO125, GO250 and GO500 for Experiment 1. The reference is an uncoated polyethylene substrates. E1: pure epoxy with acetone. E2: pure epoxy with acetone and ethanol. GXXX: samples with 0.XXX wt% G. GOXXX: samples with 0.XXX wt% GO. XXX = 125, 250, 500.

Figure 4.18 displays the estimated area coverage of algae growth measured in percent with respect to total measured area of each sample. All coating samples showed less algae growth compared to the reference sample. The degree of fouling on E1 and E2 was similar when considering the uncertainty. It was observed that all coatings containing G and GO expressed a growth inhibiting behaviour when compared to E1 and E2 coatings respectively. No significant trend regarding growth inhibiting behaviour with respect to increasing wt% of G and GO was observed.

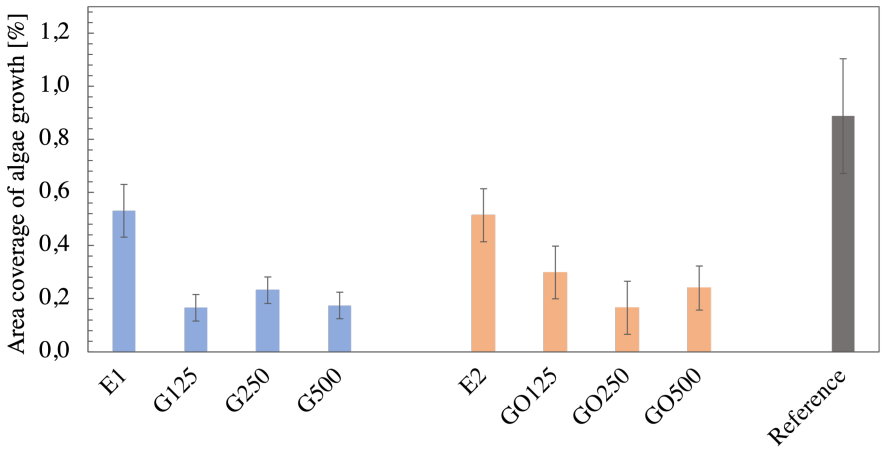

Figure 4.18: Bar chart showing estimated area of algae growth on prepared coatings and on uncoated polyethylene substrates (reference) in percent with respect to total measured area. E1: pure epoxy with acetone. E2: pure epoxy with acetone and ethanol. GXXX: samples with 0.XXX wt% G. GOXXX: samples with 0.XXX wt% GO. XXX = 125, 250, 500.

Algae culture 2

The number of diatoms per mm^2 present on all immersed samples after the performance of the biofilm reactor experiment with algae culture 2 are visually displayed in Figure 4.19. The diatom specie used for quantification by the direct count method was determined in Section 4.3.1 under **Algae culture 2**. All coatings showed significantly less diatom adhesion compared to reference samples. In addition, similar diatom growth was observed on E1 and E2 coatings. A growth inhibiting behaviour was observed for all G coatings when compared to E1 coatings. The experiment indicated that the diatom adhesion increased with increasing content of G, but the uncertainty in G250 makes this indication weak. For GO coatings, no growth inhibiting behaviour was observed for GO125 compared to E2. GO250 and GO500 experienced less diatom adhesion compared to E2.

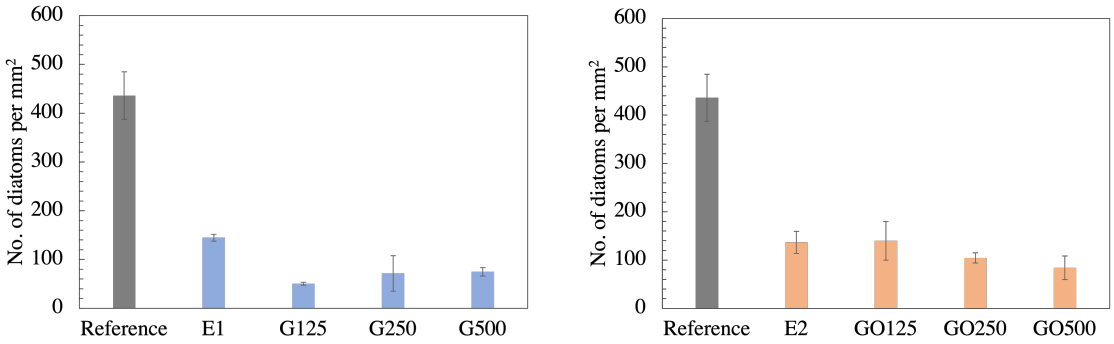

Figure 4.19: Bar chart showing number of adhered diatoms per mm^2 of (a) E1, G125, G250 and G500 coatings and of (b) E2, GO125, GO250 and GO500 for Experiment 2. The reference is an uncoated polyethylene substrates. E1: pure epoxy with acetone. E2: pure epoxy with acetone and ethanol. GXXX: samples with 0.XXX wt% G. GOXXX: samples with 0.XXX wt% GO. XXX = 125, 250, 500.

Figure 4.20 displays the estimated area coverage of algae growth measured in percent with respect to total measured area for each sample. All coatings experienced less algae growth compared to the reference sample. E1 and E2 coatings showed similar algae growth when considering uncertainties. The estimated algae growth was found to be significantly less on coatings containing G and GO compared to pure epoxy coatings. Within G and GO coatings, no dependency of fouling was found with respect to increasing wt% of G and GO.

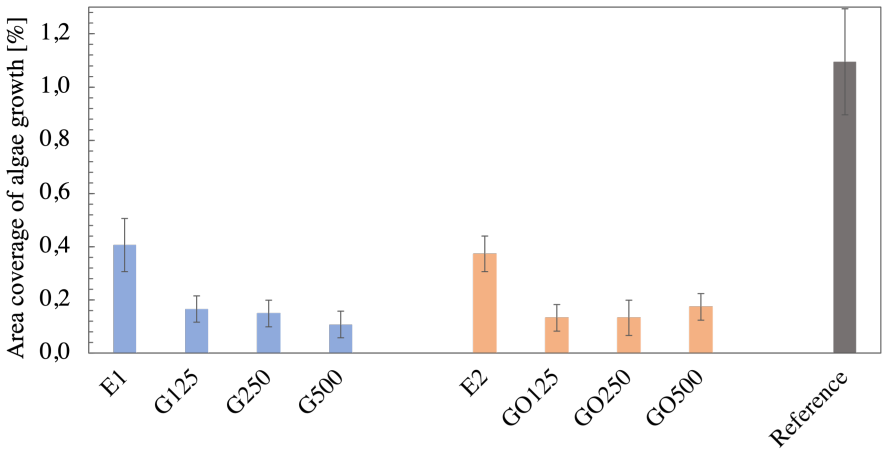

Figure 4.20: Bar chart showing estimated area of algae growth on prepared coatings and on uncoated polyethylene substrates (reference) in percent with respect to total measured area. E1: pure epoxy with acetone. E2: pure epoxy with acetone and ethanol. GXXX: samples with 0.XXX wt% G. GOXXX: samples with 0.XXX wt% GO. XXX = 125, 250, 500.

The growth inhibiting effect of G and GO

The growth inhibiting effect of G and GO in pure epoxy coatings submerged in algae culture 1 and algae culture 2 is displayed in Figure 4.21 (a) and (b) respectively. The figure shows the percent of algae growth on nanocomposite coatings compared to respective pure epoxy coatings, calculated from the direct count method (DCM) and the area estimation (AE). Generally, all nanocomposites experienced 40% less algae growth compared to pure epoxy coatings. An exception occurred for the number of adhered diatoms per mm^2 on GO coatings from algae culture 2, exceeding 60% algae growth for all concentrations. Overall, G coatings exhibited the best growth-inhibiting behaviour as all coatings experienced 50% less algae growth compared to their respective pure epoxy coating.

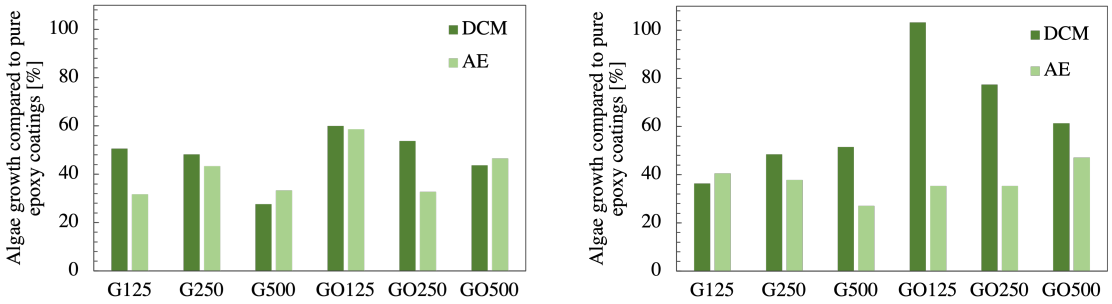

(a) **(b)**

Figure 4.21: Percent algae growth on G and GO coatings compared to respective pure epoxy coatings estimated by the direct count method (DCM) and by area estimation (AE) for (a) algae culture 1 and (b) algae culture 2. GXXX: samples with 0.XXX wt% G. GOXXX: samples with 0.XXX wt% GO. XXX = 125, 250, 500.

Estimation of biofilm thickness

The biofilm thickness of the submerged samples, including epoxy coatings, G and GO coatings and uncoated PE substrate, was attempted measured and the results is presented below. Figure 4.22 shows the obtained "begin point" and "end point" of the z-stack for an E1 coating from the biofilm experiment with algae culture 1. The contour of the same diatoms was observed at each point of the measurement, marked out for one example in the images. This indicated that the biofilm consisted only of one diatom layer. That is, no diatom species had grown on top of each other. This observation was done for all samples, for algae culture 1 and algae culture 2. The biofilm thickness was not measurable for any of the immersed samples.

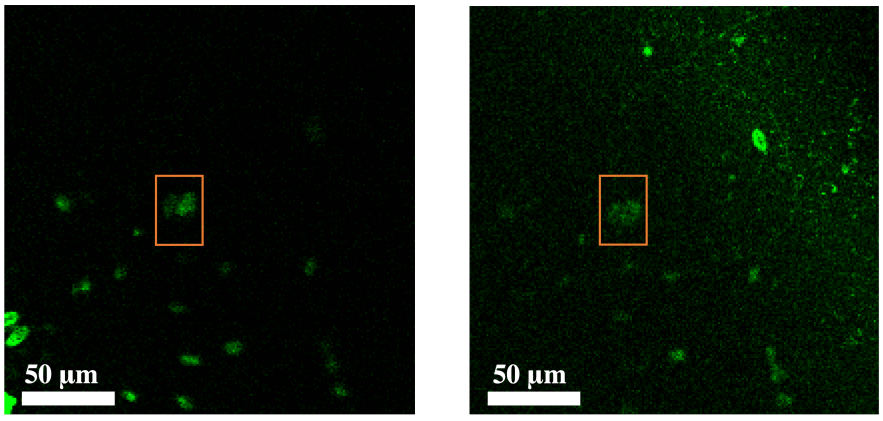

(a) **(b)**

Figure 4.22: The (a) "begin point" and (b) "end point" of a z-stack captured by confocal microscopy, defining the fluorescent biofilm layer obtained on an E1 coating. Similar images were obtained for all coating systems, including G125, G250, G500, E2, GO125, GO250 and GO500 coatings. E1: pure epoxy with acetone. E2: pure epoxy with acetone and ethanol. GXXX: samples with 0.XXX wt% G. GOXXX: samples with 0.XXX wt% GO. XXX = 125, 250, 500.

5 Discussion

The overall aim of this master's thesis has been to evaluate the antifouling performance of graphene and graphene oxide in epoxy-based coatings, suitable for marine applications. The first part considers the quantitative methods of identifying antifouling, followed by an assessment of the evident outcome of the biofilm reactor experiments. Thereafter, the possible antifouling behaviour of G and GO coatings is evaluated in relation to coating characteristics relevant to antifouling performance. Based on this, the antifouling mechanism of G and GO is suggested. Further discussion includes an assessment of the biofilm reactor experiment. Then, the coating quality is evaluated concerning mechanical performance and coating deposition technique. Finally, the chosen synthesis method for the production of G and GO nanocomposites is reviewed to evaluate the efficiency and success of the process.

5.1 Identifying biofouling

Diatoms were found as the dominating fouling specie on all samples and were chosen as the measure of antifouling. Diatoms dominate the initial stage of biofouling and will provide essential information for the subsequent macrofouling [31]. The growth of diatoms was estimated with regards to the number of diatoms per mm^2 and covered area of algae growth in percent, by considering two-dimensional growth. The z-stack measurement of the biofilms confirmed that all samples experienced only one layer of diatom growth (see Figure 4.22), which substantiated the outcome of the chosen quantification methods.

5.1.1 The combined effect of the applied quantification method and algae culture

The direct count method quantified the number of single, non-clustered, diatoms of a certain specie. Manual counting enabled controlled selection of the desired fouling specie, which served useful with respect to limiting the uncertainty of the method. The area estimation quantified diatom growth by utilizing color contrasts in transmittance mode, and the diatom growth was easily distinguished as it generally appeared at a common contrast. This technique also considered various fouling species, like green algae or accumulation of bacteria and organic material, when present on the immersed sample.

Algae culture 1 consisted of various fouling species, of unknown composition. As shown in Figure 4.15, attachment of bacterial matter appeared frequently on all coatings in addition to diatom growth. The adhesion of bacterial matter seemed to facilitate a heavy accumulation of diatoms. As a consequence, appropriate counting was at times difficult for samples immersed in algae culture 1 when considering the number of diatoms. The area estimation generated an

understanding of the total algae growth, including diatom clustering, instead of the adhesion of single diatoms.

Algae culture 2 consisted of a clean algae culture of one single diatom specie, most likely a Grammonema specie, with small contamination of an additional diatom specie (see Figure 4.15). This second specie may be contamination from the sea pump system which was utilized in other biofilm reactor experiments, even though proper cleaning was performed between each experiment. Applying a culture of one single diatom composition was beneficial to obtain diatom growth without significant clustering, facilitating the counting process. As no additional bacterial matter or significant diatom clustering was observed on samples immersed in algae culture 2, both the direct count method and the area estimation generated an understanding of the single diatom growth on these samples.

5.1.2 Test validity

A way to evaluate the validity of the measurements was by comparing the algae growth on E1 and E2 coatings. Their growth inhibiting behavior was expected to be similar as their coating compositions in cured state are assumed equal, by assuming complete solvent evaporation. Generally, it was found that the pure epoxy coatings (E1 and E2) appeared equally fouled within each biofilm reactor experiment (see Section 4.3.2). This observation substantiates the validity of the biofilm reactor experiments and the subsequent characterizations.

To minimize the uncertainty of the diatom identification, it was desired to examine a major part of each sample. The total area analyzed in each quantification method was a compromise with respect to the measurement time. Overall, the area estimation may have obtained a higher accuracy as it considered a larger part of the immersed samples compared to the direct count method. On the contrary, the direct count method may have benefited from considering the algae growth at a higher magnification, enabling controlled characterization of the specific foulants. Further analysis may benefit from implementing automatic counting of diatoms to cover greater surface areas and streamline the quantification process.

5.2 Evaluation of the antifouling performance of G and GO

A total evaluation of the two biofilm reactor experiments indicated that an additional growth-inhibiting behavior was observed for G and GO coatings with respect to pure epoxy coatings. Of all coatings, G coatings seemed to experience the best antifouling behavior. Consistently, G coatings experienced 50% less algae growth compared to pure epoxy coatings, while GO coatings showed inconsistent behavior. The antifouling performance of the nanocomposite coatings appeared to be dependent on the type of algae culture and the specie being analyzed, i.e. single diatoms or diatom clustering and bacterial attachment. Similar experiments have been reported to evaluate both the fundamental adhesion of certain marine microorganisms and the antifouling behavior of specific materials [247]. Further assessment of the effect of the specific fouling species was not feasible, as the types of species were unknown.

Regarding antifouling behavior as a function of the weight ratio of antifouling agents up to 0.500 wt% G and GO, it was difficult to extract one definite trend as the applied quantification methods were not in agreement (see Figure 4.21). The measured algae growth on samples of algae culture 1 indicated that the amount of G and GO within the epoxy coatings will influence the single diatom adhesion, providing better growth resistance with increasing nanoparticle content. Further, it implied that the adhesion of other marine microorganisms, like bacteria and organic material, will not be influenced by an increasing G and GO content. The diatom growth measured on samples immersed in algae culture 2 substantiated that an increasing weight ratio of G and GO did not improve the antifouling behavior of these coatings. It should be mentioned that the GO125 coating expressed no growth inhibiting behavior compared to pure epoxy coatings when considering the number of diatoms per mm^2. However, this effect was not observed by the area estimation and may be a result of the uncertainty associated with the direct count method. Further work should consider strategies for optimizing the quantification methods to enhance the comparability of the results.

5.3 Evaluation of surface properties relevant for antifouling performance

Literature implies that certain surface properties, like surface roughness, wettability and surface free energy, can influence the antifouling performance of coatings. These properties have been characterized for the prepared coatings, and the following section will combine obtained results with literature to evaluate the antifouling potential of G and GO coatings.

5.3.1 Effect of surface roughness

It is generally agreed that a rougher surface will promote marine biofouling [215]. All coated samples had significantly less roughness compared to the uncoated substrate (reference sample), as shown in Table 4.5. This implies that the reference sample exhibited more surface irregularities. That is, it contained more anchoring sites for algae species to attach. Hence, more biofouling was expected on the reference samples. The biofilm reactor experiments confirmed that the uncoated substrates appeared significantly more fouled compared to all coatings. From the total evaluation of the diatom count and the area estimations, the average difference in algae growth between the uncoated substrates and the coatings appeared more distinct from samples of algae culture 2 compared to algae culture 1. This was most likely an effect of the smaller diatom size observed for the dominant specie of algae culture 2 compared to algae culture 1. The rough substrate surface seemed to enable easier adhesion of smaller diatoms, while larger diatoms struggle to exploit anchoring sites of the substrate.

All coatings exhibited nanoscale roughness, where GO coatings (GO250 and GO500) showed a slight increase in roughness compared to the other coatings. Generally, bacterial attachment is found to be independent of nanoscale roughness [216], indicating that no additional antifouling performance is expected for GO coatings in relation to surface roughness. However, the increase in surface roughness at nanoscale may also be a result of GO sheets on the coating surface. The sheet distribution measurements of GO coatings indicate that GO sheets were homogeneously distributed within the coatings with a variation in sheet size (10-30 μm), significantly larger than G sheets (8 μm). Cell disruption and pore formation in bacteria and cells due to sharp edges and large basal planes of GMs are suggested as one of the predominant antifouling mechanism of these materials [100, 101]. For this reason, GO coatings (GO250 and GO500) may experience better antifouling behavior compared to pure epoxy coatings and GO125 and G coatings when surface roughness is considered. This claim was only observed for GO500 coatings immersed in algae culture 1 when considering number of diatoms per mm^2. In addition, no enhanced antifouling performance was observed for GO coatings compared to G coatings. Presumably, the increased nanoscale roughness of GO coatings was not an effect of GO sheets on the coating surface, rather an effect of increased slurry viscosity for GO250 and GO500 coatings (further discussed in Section 5.6.3).

5.3.2 Effect of wettability

All coatings were of hydrophilic character, which in literature has shown to suppress adhesion of diatom species [238], while favouring adhesion of the green algae *Ulva* [237]. Primarily, algae growth from the performed biofilm reactor experiments was quantified by considering diatom adhesion. Hence, it is believed that the hydrophilic character of the

coatings will contribute to a growth inhibiting behavior of diatoms. On the contrary, the hydrophobic PE substrate may be more prone to diatom fouling.

Generally, an uncertainty of $\pm$ 1-2° is considered for contact angle measurements [225]. Additional error may have occurred as the baseline was set manually for each measurement. The maximum difference observed within the coatings with respect to wt% G and GO, was found to be no more than 5° (see Figure 4.9). Hence, the small increase in CA with increasing wt% G and GO is considered insignificant when measurement errors are considered. Therefore, additional antifouling performance of G and GO compared to pure epoxy coatings as a function of CA measurements was not expected. This was confirmed from the biofilm reactor experiments, showing no connected trend regarding fouling on submerged coatings with respect to contact angle measurements.

The Wenzel equation implies that hydrophilic surfaces will enhance their wettability at increased surface roughness [234]. This correlation was not observed within the prepared coatings. It is generally agreed that surface roughness less than 0.5 μm will have insignificant impact on wettability. All coatings expressed roughness lower than 60 nm, which is likely why the Wenzel correlation was not observed for GO coatings ($\geq$ 0.250 wt%).

Studies of contact angle hysteresis (CAH) indicate that better fouling release properties are observed on surfaces of low hysteresis [258]. All surfaces expressed relatively similar hysteresis at 45° and 90°, including surfaces of relatively low and high degree of fouling (see Figure 4.11). These observations indicate that the effect of CAH was likely insignificant with respect to antifouling behavior of the immersed samples.

5.3.3 Effect of surface free energy

The surface free energy (SFE) of the PE substrate was found to be 40 mN/m, being significantly less than that of the prepared coatings in the range $\sim$ 50-56 mN/m. Fouling release properties are found favorable at surfaces of low SFE, at a minimum of 25 mN/m. From 25 mN/m to 60 mN/m, biofouling adhesion increases with surface energy [60]. This indicates that the coatings should experience stronger diatom adhesion compared to the PE substrate. However, Jimenez *et al.* [259] suggests that surface roughness is preponderant on the influence of fouling compared to SFE at roughness over 400 nm, indicating that the low SFE of the PE substrate (Ra >1μm) will be insignificant for its fouling performance. No significant relation for SFE was observed with wt% of G and GO within the prepared coatings, indicating no additional antifouling performance of G and GO compared to pure epoxy coatings as a function of SFE. This was confirmed by the biofilm reactor experiments, showing no common trend for fouling on submerged coatings for surface free energy.

The low SFE of the PE substrate was mainly a consequence of the absence of polar contribution (see Figure 4.10), indeed reflected in the hydrophobic character of the substrate. The polar contribution of the coatings, reflecting their hydrophilic character, was likely occurring due to the presence of polar functional groups on the coating surface. ATR-FTIR analysis implied the presence of carboxyl groups (-COOH) in pure epikote and G coatings and hydroxyl groups (-OH) in pure epikote and GO coatings, as displayed in Figure 4.5 and 4.6.

5.4 Antifouling mechanism

In the end, the growth inhibiting behavior observed for G and GO coatings did not appear to be an effect of the preliminary measures. From Section 5.3 it was determined that surface roughness, wettability and surface free energy had insignificant influence on the antifouling behavior of G and GO coatings. If any effect was present it was likely shadowed by the uncertainty of the quantification methods, indicating that another mechanism was the cause for the observed antifouling performance.

Oxidative stress was likely a dominating mechanism for the antifouling behavior of G and GO, indicated by similar studies in literature [105, 106]. G and GO have shown the ability to regulate the lipid peroxidation of micro-organisms [99] by generation of reactive oxygen species (ROS) through a non-contact interaction [108]. Hence, the generation of oxidative stress within the fouling species in the proximity of the coating surface may have prevented proper adhesion of foulants. For future work, a method to measure oxidative stress of fouling species on the surface of G and GO coatings should be constructed. Oxidative stress have previously been determined in planktonic crustacean by quantifying labeled ROS in fluorescence microscope, by measuring the generation of an enzymatic antioxidant by spectrophotometry and by detecting the lipid peroxidation [260].

Physical interactions of G and GO sheets may have facilitated cell disruption, pore formation and lipid extraction of the fouling species [99, 104]. However, the adhered diatoms observed on the immersed samples did not appear physically damaged from light microscope images with a 50X objective. It would be beneficial to examine the diatoms at a higher magnification to better visualize the physical structure of the fouling species after adhesion. Scanning electron microscopy could have been utilized to indicate incisions in algal cells caused by GO sheets [261]. The effect of physical interactions could have been improved by concentrating G and GO sheets on the coating surface. Verma *et al.* [98] used in-situ preparation to functionalize GO sheets and prepared well-dispersed GO nanocomposites with improved exposure of GO edges on the surface. A combination of exposed GO and inherent matrix properties resulted in an improved antifouling performance.

5.5 Evaluation of the biofilm reactor experiment

The implemented biofilm reactor experiment, constructed based on previous work by former master students, literature, and advice from experts in the related fields, appeared convenient for investigation and evaluation of the antifouling performance of prepared samples. It was ensured that the diatom growth occurred at appropriate salinity levels. The salinity never exceeded 4% during submersion, indicating that minimal seawater evaporation occurred. f/2-Si medium appeared to be efficient as a nutrition supply, facilitating the reproduction rate of diatoms within the algae cultures.

5.5.1 Immersion time

The samples were submerged for a period of two weeks, which appeared to be sufficient to obtain adequate algae growth on the sample surfaces. Literature suggests optimal immersion time for biofilm formation experiments to vary from 4 to 16 days [245]. For research purposes, the diatom growth on the prepared samples could potentially be better distinguished at shorter immersion time, avoiding significant diatom accumulation. Indeed, Balqadi *et al.* [262] reported a well-established biofilm community of bacteria and diatom as primary colonizers after only 24 hours immersion. At the same time, longer immersion periods would better reflect the realistic environment applicable in marine industries.

5.5.2 Light exposure

The light exposure for the biofilm reactor experiment was applied by a single light with a chosen light/dark cycle, enabling specific oriented exposure. However, the experiment was performed in a common laboratory with other students, which made the overall light exposure from other sources uncontrollable. Literature states that continuous light exposure to marine species can suppress the reproduction rate of diatoms [263]. However, sufficient diatom adhesion on the immersed samples indicated that the cell division was unaffected by the given exposure. Regardless, it would be beneficial to perform the biofilm reactor experiments in a delimited space to gain complete control of the light exposure to optimize growth conditions.

5.5.3 Seawater temperature

The biofilm reactor experiments were performed with two different algae cultures, with different demands with respect to optimal living conditions. NTNU Sealab proposed a seawater

temperature ranging from 15-20 °C to be optimal for the mixed algae culture, while the polar algae from CCAP thrived in cold waters from 2-6 °C. Both algae cultures were maintained in the same water bath with the same temperature and light exposure prior to, during and after the implementation of the biofilm experiments. Diatom reproduction rates have generally shown to increase with increasing seawater temperature [264]. Hence, the temperature of 14.5 °C was chosen as a compromise to avoid suppressed diatom growth. It appeared as if the chosen temperature served useful with respect to diatom growth, as sufficient growth was observed on the immersed samples. Ideally, the two algae cultures should have been maintained in separate water baths to optimize the growth conditions with respect to demanded needs. However, this was not feasible as the required equipment supply was not attainable.

5.5.4 Seawater pump

The seawater pump, with a pump speed of 1 L/min, ensured a dynamic flow of seawater within the biofilm reactor. The water flow served useful to obtain a homogeneous distribution of diatoms, oxygen, and nutrition, to avoid dominant or suppressed algae growth in different areas of the reactor. Studies report that high flow rates can inhibit the reproduction of algae species [265]. It appeared as if the chosen pump speed was convenient and did not suppress the reproduction of diatoms, as sufficient algae growth was observed on the reference samples. In addition, a more realistic marine environment was insinuated with the use of proper water flow, which was beneficial to evaluate the antifouling behavior of the coatings with respect to future marine applications.

5.5.5 Biofilm reactor set-up

Diatoms can divide into two new cells at most once every day [266], indicating that the algae culture composition and diatom concentration varied significantly with respect to time. In addition, the reproduction rate of diatoms will be affected by light, salinity, and temperature. For comparison research of the growth inhibiting behavior of the immersed samples, it was beneficial to perform each biofilm reactor experiment in one single reactor to ensure equal exposure to the given fouling environment for all samples. The hydrophilic nature of GO sheets makes GO significantly more soluble in water compared to hydrophobic G sheets [87]. This indicates that GO-release in the biofilm reactor may have occurred, which might have reduced the overall fouling growth on the submerged samples. This effect was considered insignificant for comparison research as all samples were equally exposed to the release of GO.

5.6 Assessment of coating performance and quality

In addition to exhibiting good antifouling behavior, the prepared coatings should also meet the requirements of coating performance and quality for application in harsh marine environments. Therefore, the mechanical influence of G and GO in the epoxy matrices was evaluated, the degree of coating adhesion relative to the applied substrate material was considered and the efficiency of the applied coating deposition technique was assessed.

5.6.1 Evaluation of mechanical properties

It was assumed that the nanoindentation measurements characterized the hardness and the elastic behavior of the prepared coatings with success. Any influence from the substrate was neglected as the 10% rule was not exceeded [188]. I.e. the penetration depth did not exceed 10% of the coating thickness. Indeed, non of the measurements exceeded 1 μm in penetration depth, corresponding to less than 0.5% of the average coating thickness (> 200 μm). The measured values of friction coefficient were only applied for comparative testing, as the nanoscratch test has been reported to heavily rely on instrument parameters [193].

Hardness and Young's modulus

The nanoindentation measurements indicated that GO ($\geq$ 0.250 wt%) successfully implemented the coating matrices. A significant increase in hardness was observed for GO coatings at 0.250 and 0.500 wt%, with respect to their respective pure epoxy coating. Oxygenated functional groups present on the GO sheets, like carboxyl and hydroxides, have probably reacted with epoxy groups and improved the interfacial bonding strength between GO and epoxy resin, forming a dense and strong polymer network. This is in agreement with literature, reporting that GO is suitable as filler in epoxy matrices with excellent interfacial adhesion due to the presence of functional groups [127], forming rigid hydrogen bonds [267]. This effect was further enhanced by the homogeneous sheet distribution observed for GO coatings (see Figure F.1b and F.1). As a consequence, the cross-linked density of the coating may have increased, thus increasing the coating hardness [268]. The measured Young's modulus of GO500 further implies the successful implementation of GO, as GO500 expresses a more elastic behavior compared to pure epoxy coatings. An increased Young's modulus indicates a higher degree of stress transfer within the epoxy matrix [127], presumably a result of good mechanical interlocking of GO sheets due to their wrinkled rough surface. Similar discoveries have also been reported in other studies [269]. To better understand the degree of cross-linking between the epoxies and the G- and GO fillers, performing an ATR-FTIR analysis of the epoxy coatings with and without fillers could be useful [185].

The same successful implementation was not equally expected for G sheets due to the absence of functional groups. Only G coatings of low G concentrations (0.125 wt%) seemed to influence mechanical properties, indicating that G sheets fail to properly disperse into the epoxy matrix at high concentrations. G125 coatings showed an increased hardness and decreased Young's modulus with respect to pure epoxy coatings. By assuming that the G sheets supplied by CealTech AS were free of functional groups, the observed increase in hardness is likely not a consequence of interfacial bonding between the G and epoxy. The G sheets may have added a reinforcing effect due to their natural strength [83] and good dispersion (see Figure F.1a). G coatings did not experience an enhanced elastic behavior. This was likely due to the significantly smaller sheet size observed for G compared to GO, which made stress transfer through mechanical interlocking insignificant. Strong interfacial adhesion between the G sheets and the epoxy matrix could be achieved by functionalizing G, e.g. with polyoxyalkyleneamine [130].

Scratch resistance

Nanoscratch tests can indicate the adhesion strength and scratch resistance of coatings by observing a sudden change in measured lateral force, as a result of cracking or delamination of the coating [193]. No disruption was observed for any of the coatings with the applied maximum load of 8000 μN, indicating that no failure occurred during scratching. The nanoscratch test was not performed at higher loads as the applied load was the maximum of the *Hysitron* nanoindenter.

Studies report that the lubrication property of GMs, at good sheet distributions, can reduce the COF in epoxy matrices [200–202]. This was not observed in the frictional resistance extracted from the nanoscratch test of the G and GO nanocomposites. Despite the homogeneous multi-layered sheet distribution observed within the epoxy coatings, the number of nanosheets in the multi-layered G and GO particles were not characterized. Indeed, the observed G and GO sheets showed a small tendency of sheet agglomeration (see Figure 4.7). As a consequence, the effect of sheet morphology and specific surface area, to facilitate stress transfers, may have been suppressed, which might have contributed to a small increase in friction coefficient (see Figure 4.14). However, this is slightly contradicting the observed effect of GO sheets on hardness and Young's modulus. Advantageously, future analyses could extend the length of the nanoscratch and the number of parallels of the nanoscratch test to reduce the uncertainty of the test.

5.6.2 Degree of coating adhesion

Measures were done to optimize coating adhesion, including pre-treatment and proper substrate cleaning prior to coating deposition. Mechanical interlocking is an essential adhesion

force, dependent on surface roughness. The polyethylene and steel substrates were glass-blasted to obtain desired roughness. Both substrates obtained surface roughness of around 1 μm, presumably giving the applied coating the ability to anchor and crimp around surface irregularities. An increased contact area between the substrate and the coating is considered an effect of mechanical interlocking, increasing the bond density and thus the adhesion strength [203]. The hydrophilic character of steel makes it susceptible to a high degree of wetting, enabling a high contact area with the coating. This was confirmed by visually inspecting the cross-section of prepared coatings on steel substrates (see Figure 4.8), showing no air pockets or cavities on the substrate interface. Based on literature, it is likely that the steel surface consists of hydroxyl groups from the hydration of metal oxides which will bind to epoxy groups and further enhance chemical adhesion strength [204]. The hydrophobic nature of the PE substrate may lead to insufficient wetting of the coating, indicating that a poorer adhesion strength can be observed for coatings on PE substrates compared to steel. No adhesion tests were performed, but the indication of successful coating adhesion for coatings prepared on both steel and PE were physical and visually observed as no coating delamination or failure were observed prior to, or after any measurements. Preferably, the adhesion of the nanocomposite coatings should be measured by the tape test or the cross hatch test [211].

5.6.3 Effect of coating deposition technique

Spray coating was applied as the coating technique in this thesis as the method is extensively utilized in the coating industry, yielding low cost, high efficiency and versatility with the ability to coat large and complex offshore constructions, e.g. large vessels and fish nets [139]. Applying the coating in three layers served useful to prepare coatings of even surfaces, achieving complete substrate coverage. Indeed, the cross-section analyses (see Figure 4.8) indicated that a two-layered coating would be sufficient. This could with an advantage reduce material consumption and emission of volatile organic compounds (VOCs).

During spray coating, the fluid will experience shear rates ranging from 1000-4000 s^{-1} when forced through the small nozzle head. G slurries expressed a shear thinning behavior at high shear rates, enabling low viscosity during spraying, similar to that of pure epoxy sols (see Figure 4.2). Similar surface properties were therefore expected from the G slurries and epoxy sols, as confirmed by surface roughness measurements of E1 and G coatings. In addition, minimal variation was observed for the coating thickness of G coatings (see Table 4.4). The significant reduction in thickness of E1 coatings is believed to be caused by human inaccuracy, as cross-section analysis confirms that the first deposition layer was significantly thinner compared to the second and last layers (see Figure G.1). This indicated the limitation of reproducibility for hand-held spray coaters.

GO slurries behaved nearly Newtonian, with no significant dependency on shear rate. Generally, the viscosity of GO slurries increased with increasing GO content. As a consequence, high viscosities occurred during coating deposition. The increased surface roughness of GO coatings may originate from the increased viscosity observed for the GO slurries, see Figure 4.2. During spray coating, the droplet size tends to increase with increased viscosity causing uneven coating layers of higher roughness [270]. This effect is most significant for fluids with viscosities over $\sim$10 mPa·s, which agrees with the increased roughness observed for GO250 and GO500 coatings with slurry viscosities of 8 and 13 mPa·s respectively. In addition, the high viscosity observed for GO500 slurries may have led to the strong reduction in coating thickness observed for the GO500 coating compared to respective coatings. This does not seem to be a result of human inaccuracy, as the cross-section analysis (see Figure 4.8) verifies that a constant layer thickness was observed for all three deposition layers.

Overall, the spray coating technique appeared partly suitable for the production of the nanocomposites of this thesis. Limitations were observed in relation to viscosity and reproducibility. Sufficient viscosity at high nanoparticle concentrations can be achieved by adapting the solvent content for specific concentrations. This should not influence final coating properties as the solvent is expected to fully evaporate during curing. However, it raises further concern regarding the emission of VOCs, being considered an important issue in the coating industry [145]. In addition, the spray coater was replaced two times due to clogging. Although thorough cleaning of the equipment was applied, coating residue blocked the nozzle opening. The coater was changed before coating application of E2 sol and GO slurries. As a consequence, a significant difference in coating thickness and weight is observed for the E1 and G system and the E2 and GO system (see Figure 4.4). Dip coating is an easy and low-cost technique, which may be beneficial in regards to reproducibility with the ability to control coating thickness [271]. In relation to marine applications, dip coating has shown limitations for coating application of large and complex structures [139].

5.6.4 Performance of G250 and G500 coatings

Inspections of the G250 and G500 coating surfaces indicated that an additional surface film had developed (see Figure F.2). Coating characteristics, like analysis of slurry compositions, surface roughness and wettability, and the cross-section analysis showed no significant deviation with respect to other coatings. Therefore, it was assumed that the film had minimal effect on the antifouling and mechanical performance of G250 and G500 coatings. Further analysis could with advantage implement a proper composition analysis of the film to better understand its effect on surface performance. Surface contamination of coatings can be performed by element analysis in SEM using energy dispersive spectroscopy (EDS) [254] and by using grazing-angle reflection absorption of a FTIR spectroscopy [272].

5.7 Evaluation of the sol-gel process

The sol-gel process was chosen as the synthesis route for the production of G and GO nanocomposites. Former studies have found the process efficient for the production of nanocomposites, with the ability to obtain a homogeneous particle distribution with chemical coupling between nanoparticles [118]. The stability of the prepared sols and slurries was evaluated as a function of time to optimize the sol-gel process, monitoring changes in composition and the matter of particle agglomeration or sedimentation.

5.7.1 Sol and slurry composition

The characterization of functional groups within the prepared sols and slurries were evaluated with respect to G and GO content and with respect to time (see Section 4.1.3). Overall, a great overlap in composition was observed for all sols and slurries, with minimal changes over time. The transmittance band at 914 cm^{-1} corresponds to the epoxide group of the epoxy, essential in the formation of cross-linked networks of epoxy coatings [184]. The epoxide concentration appeared to be constant over the three weeks period with no evident changes with respect to G and GO content. This indicated that the polymerization process was time-independent and that the prepared sols and slurries possessed the same basis to develop the required degree of cross-linking within epoxy coatings.

The strongest changes in sol and slurry composition were observed for carboxylic groups (-COOH) and hydroxide groups (-OH), at 1710 cm^{-1} and 3350-3580 cm^{-1} respectively, as shown in Figure 4.5 and 4.6. The concentration of these functional groups seemed to change as a function of time and nanoparticle content. This could indicate that the coating process was time-dependent with respect to the composition, and that a slight variation in coating composition was expected within the prepared coatings. The ATR-FTIR analysis was performed prior to the addition of the curing agent. The curing agent will facilitate the polymerization process by reacting with epoxide groups, which will increase the final -OH content (see Figure 2.6). Hence, it is believed that the observed differences in sol and slurry composition had minimal influence on the cured coating compositions.

5.7.2 Stability of sols and slurries over time

The evaluation of sol and slurry stability (see Figure 4.1) indicated that the epoxy sols and G slurries appeared stable over the three weeks, with no visible fluid separation or sedimentation respectively. Epikote 828 resin appeared to be compatible with acetone and with a solvent weight ratio of 1:1 of acetone and ethanol, and it was concluded that the two ba-

sis systems for coating preparation were successful. It is claimed that stable dispersion of G is difficult to achieve due to strong Van der Waals (VdW) attraction forces between the nanoparticles. G was dispersed with acetone as a solvent, which in literature has shown to stabilize G [164]. It is believed that G will possess a surface charge when disperse in organic solvents, as a result of charge transfer between the solvent molecules and the G sheets. Accordingly, it is believed that a zeta potential was established between the G sheets and that electrostatic stabilization was the main contribution to the stabilized G slurries. It should be noted that G was supplied by CealTech AS, in pre-made stable G-Epikote dispersions. The synthesis route was confidential, and the stability mechanism is not defined. The stable G-Epikote dispersion could have been achieved by chemical functionalization of G sheets, making steric stabilization a contribution to stability.

The GO slurries appeared partly stable, experiencing sedimentation one week after preparation. The GO system consisted of Epikote resin in mix with a solvent weight ratio of 1:1 of acetone and ethanol. Studies report GO to be stable in ethanol due to high zeta potentials, suggesting electrostatic stabilization to be the main stabilization mechanism. On the contrary, poor GO dispersions have been obtained with acetone due to low zeta potentials [168]. Presumably, acetone and ethanol counteract each other in the GO slurries, resulting in poorly dispersed GO sheets due to insufficient zeta potential. Ethanol was not chosen as a single solvent in GO slurries as previous work has documented bisphenol A epoxies to be unstable in ethanol [255]. Prior to coating deposition, GO slurries were sonicated to re-disperse the GO sheets. The GO sheets were found evenly distributed within the prepared coatings (see Figure 4.7), indicating that GO sheets were easily re-separated. Easy re-separation is likely arising from the presence of functional groups on GO sheets, facilitating higher repulsion forces and less VdW attraction forces [273]. However, to avoid damaging GO sheets, i.e. size reduction, ultrasonic treatments should be minimized or avoided. The effect can potentially suppress antifouling performance, as sharp edges and larger lateral size of GO sheets are reported beneficial [21]. Tetrahydrofuran (THF) can potentially function as a replacement of acetone in GO slurries, expressing similar properties to that of acetone. The compound is reported relatively non-toxic and volatile with a long-term stability of GO [170, 274], appropriate for spray coating application. Implementation of this compound, or other appropriate solvents, for nanocomposite synthesis of GO can potentially prevent the use of ultrasonic treatment.

5.8 Complete assessment of the coating performance

The following part gives a short summary of the coating performance of G and GO nanocomposites, including their antifouling and mechanical behavior.

- An antifouling behavior was observed for G and GO coatings; G and GO coatings appeared less fouled compared to pure epoxy coatings.
- G coatings experienced slightly better antifouling properties compared to GO coatings; all G coatings experienced 50% less algae growth compared to pure epoxy coatings.
- G and GO did not show a definite influence on antifouling performance as a function of increasing wt%. This was likely a result of the accuracy of the quantification methods; small differences were shadowed by uncertainties.
- The generation of oxidative stress was presumably the dominating antifouling mechanisms of G and GO coatings, possibly assisted by physical interactions between the foulant species and the G and GO nanosheets.
- All coatings experienced less algae growth compared to uncoated substrates, likely due to the rough substrate surface. The hydrophilic nature of the coatings opposed to the hydrophobic nature of the uncoated PE substrate may have further encouraged the difference in diatom growth.
- Oxygenated functional groups of GO sheets contributed to proper chemical linkage with the epoxy network, resulting in an increased coating hardness. Mechanical interlocking by the large basal planes of GO facilitated stress transfers within the cross-linked epoxy network, which enhanced the elastic behavior of epoxy coatings.
- G did not seem to enhance the mechanical performance of epoxy coatings. Presumably, the small basal planes of G did not facilitate additional stress transfers, and the lack of functional groups led to poor chemical coupling between G sheets and the epoxy network. Improved hardness of G coatings at low concentration was likely a result of the good G dispersion and the natural strength of G.

6 Conclusion

In this master's thesis, it has been demonstrated that addition of graphene and graphene oxide increases the antifouling properties of epoxy-based coatings. G showed the best antifouling properties, with each G coating experiencing 50% less algae growth compared to pure epoxy coatings. Further, the algae growth appeared to be independent of the increasing weight ratio of G and GO. Preliminary measures, including estimation of surface roughness, wettability, and surface free energy, did not substantiate the antifouling behavior of G and GO. Hence, the generation of oxidative stress was considered the predominant mechanism for the antifouling performance of G and GO coatings, possibly with assistance from physical interactions of G and GO sheets. The reduced fouling observed for all coatings compared to uncoated substrates was most likely encouraged by the significantly rougher substrate surface. In addition, the hydrophilic nature of all coatings may have further suppressed diatom adhesion.

The biofilm reactor experiment was successfully implemented to evaluate the antifouling performance of prepared samples. Combining all samples in one reactor served useful to compare samples with equal environmental exposure, including light cycles and algae cultures of the same composition and age. Using an algae culture of mixed composition demonstrated a realistic marine environment, but complicated the subsequent characterization. A clean algae culture of one diatom specie still encouraged fouling and served useful to obtain diatom growth without clustering, which made characterization easier. According to the findings, fouling on submerged samples depended on algae species, size, and morphology.

Substrate pre-treatment, including glass-blasting, and proper cleaning contributed to good coating adhesion for steel and PE substrates. Presumably, steel obtained better coating adhesion compared to the PE substrate. Likely, hydroxyl groups of the steel substrate encouraged chemical adhesion with the coating. In addition, the hydrophilic character of steel facilitated high wetting, which may have encouraged stronger adhesion as a function of mechanical interlocking. Further, nanoindentation measurements indicated that GO sheets were successfully incorporated into the epoxy network. Most likely, functional groups of GO sheets encouraged additional cross-linking within the epoxy network, which enhanced the coating hardness. In addition, the wrapped structure and large basal planes of GO sheets ensured mechanical interlocking which facilitated stress transfers, enhancing the elastic behavior of GO coatings. The reduced sheet size and lack of functional groups on G sheets discouraged proper incorporation of G into the epoxy network. Likely, G sheets did not facilitate stress transfers due to their small basal planes. The good sheet distribution and the natural strength of G were presumably the reason for an increased hardness at low concentrations of G.

The sol-gel process was implemented for the preparation of epoxy nanocomposite coatings of G and GO. Electrostatic stabilization was proposed as the main stabilization mechanism

of stable G dispersions. GO dispersions experienced sedimentation, but easy re-separation of GO sheets was likely facilitated by the presence of oxygenated functional groups. Accordingly, the G and GO nanocomposites experienced homogeneous sheet distributions. Further analysis of sol and slurry composition indicated that the polymerization process was time-independent and that the final coating compositions would exhibit insignificant variations with respect to functional groups. Spray coating appeared partly suitable for the preparation of G and GO nanocomposites, with limitations regarding viscosity and reproducibility. The shear thinning behavior of G slurries enabled easy deposition of high-concentration slurries, while the shear independent behavior of GO slurries resulted in increased surface roughness and reduced coating thickness at high concentrations of GO. In addition, the manual spray coating procedure and the partially clogged coaters were likely contributing causes to the observed variations in coating thickness.

7 Further Work

To substantiate the findings of the antifouling performance of graphene and graphene oxide coatings, additional biofilm reactor experiments should be performed. Future experiments would benefit from optimizing temperatures for relevant fouling species, and from being performed in delimited areas to control light cycles. The antifouling performance of G and GO could be further understood by performing experiments with a commercial and efficient antifouling agent for comparison, e.g. cuprous oxide [69]. In addition, it was observed that the fouling growth depended on the type of fouling specie. Hence, future investigation should include several biofilm experiments with known fouling species to further understand the antifouling performance of G and GO.

To reduce the uncertainty of the antifouling measurements, it would be beneficial to examine a larger area of the submerged samples. The small size of fouling species makes the quantification process time-consuming, as measurements should be performed at high magnification to minimize counting errors. Using an algae culture of one fouling specie served useful to obtain homogeneously distributed diatoms, which would be beneficial if automatic counting is to be implemented. Further, the estimation of biofilm thickness, including attachment of diatoms, bacteria, and proteins, should be improved to better understand the antifouling behavior of G and GO coatings. Staining the biofilms, e.g. with crystal violet [252], could encourage the fluorescent response of the films, facilitating the detection of certain marine organisms, like bacteria and protein. Sufficient z-stack resolution of the chosen instrument should be considered as biofilm thickness has been reported less than 2 μm [275].

Oxidative stress and physical disruption were suggested as contributions to the antifouling mechanisms of epoxy-based coatings with G and GO addition. The generation of oxidative stress on fouling species in the proximity of the coating surface can potentially be measured by utilizing fluorescence microscopy or spectrophotometry to detect the presence of reactive oxygen species, enzymatic antioxidants, or lipid peroxidation [260]. Physical disruption on fouling species from G and GO sheets on the coating surface can potentially be characterized by detecting incisions and cuts on fouling species through scanning electron microscopy. The antifouling effect of G and GO coatings from physical interactions, such as nanoknife disruptions, could be further increased by improving the exposure of G and GO sheets on the coating surface. This might be accomplished by combining in-situ synthesis of G and GO nanocomposites with polydimethylsiloxane functionalization of GMs [98].

To extend the shelf life of GO slurries, proper stability should be considered. The acetone-ethanol ratio could be changed in favor of ethanol to obtain a higher zeta potential of GO, which would potentially increase the electrostatic stabilization within the slurry. Another option is to employ other solvents that have induced long-term stability of GO, such as

THF. In this case, proper toxicity and emission studies should be conducted. Stable GO slurries would reduce the need of ultrasonic treatments, potentially improving the antifouling properties of GO by avoiding damage and reduction in sheet size.

Nanoindentation measurements indicated that GO increased the cross-linked density of the epoxy network. This could be further confirmed by utilizing ATR-FTIR measurements. The degree of cross-linking within the cured coatings can be measured by performing ATR-FTIR on the coating surface. Complete contact between the coating and the ATR diamond is required for the procedure, which is normally achieved by curing the coating directly on the diamond surface. Mechanical measures of G coatings indicated that G did not have the same successful incorporation within the epoxy network. G could potentially be functionalized to allow for proper incorporation. Furthermore, the influence of G and GO on scratch resistance of epoxy coatings may be further evaluated with higher loads and longer scratch lengths. However, too high startup loads should be avoided to prevent complete coating penetration. The coating performance could be further understood by evaluating the coating adhesion, by the cross-hatch test, or the pull-off test. It would also be useful to evaluate the mechanical performance of coatings prior to and after submersion in seawater.

The spray coating procedure showed limitations regarding viscosity and reproducibility. Future spray coating applications could benefit from utilizing one general viscosity for all coating slurries, by optimizing the solvent content with respect to the weight ratio of G and GO. However, caution should be considered regarding the increased emission of VOC. Uneven coating deposition from partly clogged spray coaters could be avoided by using dip coating, which promotes controllable coating thickness and appears less dependent on coating viscosity. Research analysis could benefit from this application method. However, it is not considered suitable for large-scale applications, e.g. ship hulls.

References

[1] Y. Li and C. Ning, "Latest research progress of marine microbiological corrosion and bio-fouling, and new approaches of marine anti-corrosion and anti-fouling," *Bioactive Materials*, vol. 4, pp. 189–195, 2019.

[2] "Why oceans are key to the global economy." *Reuters*, `https://www.reuters.com/article/us-oceans-economy-idUSTRE81N09Z20120224`, 2012, Accessed: 21/02/2022.

[3] L. Hammar, M. Gullström, T. G. Dahlgren, M. E. Asplund, I. B. Goncalves, and S. Molander, "Introducing ocean energy industries to a busy marine environment," *Renewable and Sustainable Energy Reviews*, vol. 74, pp. 178–185, 2017.

[4] R. Pelc and R. M. Fujita, "Renewable energy from the ocean," *Marine Policy*, vol. 26, no. 6, pp. 471–479, 2002.

[5] C. Bressy and M. Lejars, "Marine Fouling: An Overview," *Journal of Ocean Technology*, vol. 9, pp. 19–28, 2014.

[6] R. Braithwaite and L. McEvoy, "Marine Biofouling on Fish Farms and Its Remediation," pp. 215–252, 2004.

[7] M. E. Callow and J. E. Callow, "Marine biofouling: a sticky problem.," *Biologist (London, England)*, vol. 49, no. 1, pp. 10–4, 2002.

[8] J. Lin, "Initial corrosion behavior under biofilms of metal material in sea water," *Harbin Engineering University, Harbin*, 2006.

[9] G. R. Weisman, D. C. Sundberg, R. A. Cimini, M. G. Brown, B. R. Beno, and T. T. Eighmy, "Controlled release antifouling coatings. i. approaches for controlled release of 2, 4-dinitrophenolate and benzoate into seawater," *Biofouling*, vol. 6, no. 2, pp. 123–146, 1992.

[10] U. S. N. Institute, "Chapter 1: The effects of fouling," *Marine Fouling and Its Prevention*, 1952.

[11] G. Jones, "The battle against marine biofouling: A historical review," *Advances in Marine Antifouling Coatings and Technologies*, pp. 19–45, 2009.

[12] M. P. Schultz, "Frictional resistance of antifouling coating systems," *J. Fluids Eng.*, vol. 126, no. 6, pp. 1039–1047, 2004.

[13] M. Stanczak, "Biofouling: It's not just barnacles anymore," *Dostęp on-line*, vol. 10, p. 2013, 2004.

[14] K. Z. Hunsucker, C. Braga, H. Gardner, M. Jongerius, R. Hietbrink, B. Salters, and G. Swain, "Using ultraviolet light for improved antifouling performance on ship hull coatings," *Biofouling*, vol. 35, no. 6, pp. 658–668, 2019.

[15] A. C. Sousa, S. Tanabe, and M. R. Pastorinho, "Organotins: Sources and impacts on health and environment," *Encyclopedia of the Anthropocene*, vol. 1-5, pp. 133–139, 2017.

[16] C. Hellio and D. Yebra, "1 - introduction," in *Advances in Marine Antifouling Coatings and Technologies*, Woodhead Publishing Series in Metals and Surface Engineering, pp. 1–15, 2009.

[17] J.-P. Maréchal and C. Hellio, "Challenges for the development of new non-toxic antifouling solutions," *International Journal of Molecular Sciences*, vol. 10, no. 11, pp. 4623–4637, 2009.

[18] M. Srinivasan and G. W. Swain, "Managing the use of copper-based antifouling paints," *Environmental Management*, vol. 39, no. 3, pp. 423–41, 2007.

[19] Y. Tu, M. Lv, P. Xiu, T. Huynh, M. Zhang, M. Castelli, Z. Liu, Q. Huang, C. Fan, H. Fang, *et al.*, "Destructive extraction of phospholipids from escherichia coli membranes by graphene nanosheets," *Nature nanotechnology*, vol. 8, no. 8, pp. 594–601, 2013.

[20] P. Kumar, P. Huo, R. Zhang, and B. Liu, "Antibacterial properties of graphene-based nanomaterials," *Nanomaterials*, vol. 9, no. 5, 2019.

[21] S. Liu, M. Hu, T. H. Zeng, R. Wu, R. Jiang, J. Wei, L. Wang, J. Kong, and Y. Chen, "Lateral dimension-dependent antibacterial activity of graphene oxide sheets," *Langmuir*, vol. 28, no. 33, pp. 12364–12372, 2012.

[22] H. Jin, L. Tian, W. Bing, J. Zhao, and L. Ren, "Toward the application of graphene for combating marine biofouling," *Advanced Sustainable Systems*, vol. 5, no. 1, pp. 20–76, 2021.

[23] W. Zheng, W. G. Chen, Q. zhao, S. X. Ren, and Y. Q. Fu, "Interfacial structures and mechanisms for strengthening and enhanced conductivity of graphene/epoxy nanocomposites," *Polymer*, vol. 163, pp. 171–177, 2019.

[24] D. Galpaya, M. Wang, G. George, N. Motta, E. Waclawik, and C. Yan, "Preparation of graphene oxide/epoxy nanocomposites with significantly improved mechanical properties," *Journal of Applied Physics*, vol. 116, no. 5, 2014.

[25] T. J. Bjaanes, "Application of graphene and graphene oxide as antifouling agents in epoxy based coatings," *Specialization project, Norwegian University of Science and Technology*, 2021.

[26] F. Zhou, *Antifouling Surfaces and Materials: from land to marine environment*. Springer, 2014.

[27] L. Engelhardt, "Antifouling your boat, club marine volume 33 issue 3." `https://www.clubmarine.com.au/exploreboating/articles/32-3-Keeping-A-Clean-Bottom`, , Accessed: 23/02/2022.

[28] P. A. Azis, I. Al-Tisan, M. Al-Daili, T. N. Green, K. Ba-Mardouf, S. A. Al-Qahtani, and K. Al-Sabai, "Marine macrofouling: a review of control technology in the context of an on-line experiment in the turbine condenser water box of al-jubail phase-1 power/msf plants," *Desalination*, vol. 154, no. 3, pp. 277–290, 2003.

[29] A. J. Martín-Rodríguez, J. M. Babarro, F. Lahoz, M. Sansón, V. S. Martin, M. Norte, and J. J. Fernandez, "From broad-spectrum biocides to quorum sensing disruptors and mussel repellents: Antifouling profile of alkyl triphenylphosphonium salts," *PLoS One*, vol. 10, no. 4, 2015.

[30] M. A. Miller, J. C. Rapean, and W. F. Whedon, "The role of slime film in the attachment of fouling organisms," *The Biological bulletin (Lancaster)*, vol. 94, no. 2, pp. 143–157, 1948.

[31] N. Poulsen, N. Kröger, M. J. Harrington, E. Brunner, S. Paasch, and M. T. Buhmann, "Isolation and biochemical characterization of underwater adhesives from diatoms," *Biofouling*, vol. 30, no. 4, pp. 513–523, 2014.

[32] W. e. a. Müller, "Principles of biofouling protection in marine sponges: A model for the design of novel biomimetic and bio-inspired coatings in the marine environment?," *Marine biotechnology (New York, N.Y.)*, vol. 15, no. 4, pp. 375–398, 2013.

[33] G. Smedes, "Seasonal changes and fouling community interactions," *Marine biodeterioration: an interdisciplinary study*, pp. 155–160, 1984.

[34] K. P. Sebens, "Spatial relationships among encrusting marine organisms in the new england subtidal zone," *Ecological Monographs*, vol. 56, no. 1, pp. 73–96, 1986.

[35] K. Nandakumar, "Importance of timing of panel exposure on the competitive outcome and succession of sessile organisms," *Marine Ecology Progress Series*, vol. 131, pp. 191–203, 1996.

[36] K. Nandakumar, M. Tanaka, and T. Kikuchi, "Interspecific competition among fouling organisms in tomioka bay, japan," *Marine Ecology-Progress Series*, vol. 94, pp. 43–43, 1993.

[37] H. Arndt, K. Schmidt-Denter, B. Auer, and M. Weitere, "Protozoans and biofilms," in *Fossil and recent biofilms*, pp. 161–179, Springer, 2003.

[38] J. Lawrence and R. Snyder, "Feeding behaviour and grazing impacts of a euplotes sp. on attached bacteria," *Canadian Journal of Microbiology*, vol. 44, no. 7, pp. 623–629, 1998.

[39] D. A. Caron, "Grazing of attached bacteria by heterotrophic microflagellates," *Microbial Ecology*, vol. 13, no. 3, pp. 203–218, 1987.

[40] D. M. Yebra, S. Kiil, and K. Dam-Johansen, "Antifouling technology—past, present and future steps towards efficient and environmentally friendly antifouling coatings," *Progress in Organic Coatings*, vol. 50, no. 2, pp. 75–104, 2004.

[41] C. Iselin, "Marine fouling and its prevention," *Woods Hole Oceanographic Institution, US Naval Institute, Annapolis, MD*, 1952.

[42] A. Kerr, C. Beveridge, M. Cowling, T. Hodgkiess, A. Parr, and M. Smith, "Some physical factors affecting the accumulation of biofouling," *Journal of the Marine Biological Association of the United Kingdom*, vol. 79, no. 2, pp. 357–359, 1999.

[43] P. Birak and C. Miller, "Dense non-aqueous phase liquids at former manufactured gas plants: Challenges to modeling and remediation," *Journal of Contaminant Hydrology*, vol. 105, no. 3, pp. 81–98, 2009.

[44] M. L. Chen, Y. Y. Qu, L. Yang, and H. Gao, "Structures and antifouling properties of low surface energy non-toxic antifouling coatings modified by nano-sio2 powder," *Science in China, Series B: Chemistry*, vol. 51, no. 9, pp. 848–852, 2008.

[45] J. Lee, H. R. Chae, Y. J. Won, K. Lee, C. H. Lee, H. H. Lee, I. C. Kim, and J. m. Lee, "Graphene oxide nanoplatelets composite membrane with hydrophilic and antifouling properties for wastewater treatment," *Journal of Membrane Science*, vol. 448, pp. 223–230, 2013.

[46] R. E. Baier, "Surface behaviour of biomaterials: the theta surface for biocompatibility," *Journal of Materials Science: Materials in Medicine*, vol. 17, no. 11, pp. 1057–1062, 2006.

[47] D. Dalaklis, E. B. Besikci, J. Larsson, A. Christodoulou, and T. M. Johansson, "The maritime commons: Digital repository of the world maritime university," pp. 1–2, 2018.

[48] M. Schultz, J. Bendick, E. Holm, and W. Hertel, "Economic impact of biofouling on a naval surface ship," *Biofouling*, vol. 27, no. 1, pp. 87–98, 2011.

[49] G. Partnership, "Impact of ships' biofouling on greenhouse gas emissions," *Biofouling control strategy*, 2020.

[50] R. Braithwaite and L. McEvoy, "Marine biofouling on fish farms and its remediation.," *Advances in marine biology*, vol. 47, pp. 215–252, 2005.

[51] H. Videla, "Metal dissolution/redox in biofilms," *Structure and function of biofilms*, pp. 301–320, 1989.

[52] H. Videla, "Corrosion inhibition in the presence of microbial corrosion," *Corrosion 96*, no. 223, 1996.

[53] Y. Li and C. Ning, "Latest research progress of marine microbiological corrosion and bio-fouling, and new approaches of marine anti-corrosion and anti-fouling," *Bioactive Materials*, vol. 4, pp. 189–195, 2019.

[54] K. Nandakumar and T. Yano, "Biofouling and its prevention: a comprehensive overview," *Biocontrol science*, vol. 8, no. 4, pp. 133–144, 2003.

[55] J. Xu, C.-Y. Chang, J. Hou, and C. Gao, "Comparison of approaches to minimize fouling of a uf ceramic membrane in filtration of seawater," *Chemical Engineering Journal*, vol. 223, pp. 722–728, 2013.

[56] J.-S. Park and J.-H. Lee, "Sea-trial verification of ultrasonic antifouling control," *Biofouling*, vol. 34, no. 1, pp. 98–110, 2018.

[57] C. Protection Co Ltd, "Electrolytic anti-fouling in industrial and marine applications," *Anti-Corrosion Methods and Materials*, vol. 34, no. 8, pp. 15–20, 1987.

[58] H. J. Polman and H. Jenner, "Pulse-chlorination, the best available technique in macrofouling mitigation using chlorine," *PowerPlant Chemistry*, vol. 4, pp. 93–100, 2002.

[59] J. A. Lewis, "Non-silicone biocide-free antifouling solutions," *Advances in Marine Antifouling Coatings and Technologies*, pp. 709–724, 2009.

[60] A. Pistone, C. Scolaro, and A. Visco, "Mechanical properties of protective coatings against marine fouling: A review," *Polymers*, vol. 13, no. 2, p. 173, 2021.

[61] A. K. Roy Choudhury, "11 - finishes for protection against microbial, insect and uv radiation," in *Principles of Textile Finishing*, Woodhead Publishing Series in Textiles, pp. 319–382, 2017.

[62] M. Warnez and O. Hansen, "Self-polishing polymers for antifouling paints," in *Federation of Scandinavian Paint and Varnish Technologists, 10th Congress, October*, pp. 11–13, 1982.

[63] S. Kiil, C. E. Weinell, M. S. Pedersen, and K. Dam-Johansen, "Analysis of self-polishing antifouling paints using rotary experiments and mathematical modeling," *Industrial & engineering chemistry research*, vol. 40, no. 18, pp. 3906–3920, 2001.

[64] S. Kiil, K. Dam-Johansen, C. E. Weinell, and M. S. Pedersen, "Seawater-soluble pigments and their potential use in self-polishing antifouling paints: simulation-based screening tool," *Progress in Organic Coatings*, vol. 45, no. 4, pp. 423–434, 2002.

[65] A. G. Nurioglu, A. C. C. Esteves, *et al.*, "Non-toxic, non-biocide-release antifouling coatings based on molecular structure design for marine applications," *Journal of Materials Chemistry B*, vol. 3, no. 32, pp. 6547–6570, 2015.

[66] I. Amara, W. Miled, R. B. Slama, and N. Ladhari, "Antifouling processes and toxicity effects of antifouling paints on marine environment. a review," *Environmental Toxicology and Pharmacology*, vol. 57, pp. 115–130, 2018.

[67] T. A. Katz and C. L. Walker, "Chapter 1-4 - implications for chromatin biology in toxicology," in *Toxicoepigenetics*, pp. 105–124, Academic Press, 2019.

[68] B. S. Smith, "Sexuality in the american mud snail, nassarius obsoletus say," *Journal of Molluscan Studies*, vol. 39, no. 5, pp. 377–378, 1971.

[69] W. H. Dresher, "Copper in third-generation antifoulants for marine coatings," 2000.

[70] C. Munari and M. Mistri, "Effect of copper on the scope for growth of clams (tapes philippinarum) from a farming area in the northern adriatic sea," *Marine environmental research*, vol. 64, no. 3, pp. 347–357, 2007.

[71] A. Lotz, "Marine coatings: making sense of us, state, and local mandates of copper-based antifouling regulations," *JCT Coatingstech*, vol. 13, no. 9, pp. 50–54, 2016.

[72] Y. Gu, L. Yu, J. Mou, D. Wu, M. Xu, P. Zhou, and Y. Ren, "Research strategies to develop environmentally friendly marine antifouling coatings," *Marine Drugs*, vol. 18, no. 7, p. 371, 2020.

[73] S. Krishnan, C. J. Weinman, and C. K. Ober, "Advances in polymers for anti-biofouling surfaces," *Journal of Materials Chemistry*, vol. 18, no. 29, pp. 3405–3413, 2008.

[74] C. M. Grozea and G. C. Walker, "Approaches in designing non-toxic polymer surfaces to deter marine biofouling," *Soft Matter*, vol. 5, no. 21, pp. 4088–4100, 2009.

[75] V. Vetere, M. Pérez, M. García, M. Deyá, M. Stupak, and B. Del Amo, "A non-toxic antifouling compound for marine paints," *Surface coatings international*, vol. 82, no. 12, pp. 586–589, 1999.

[76] F. Villa, D. Albanese, B. Giussani, P. S. Stewart, D. Daffonchio, and F. Cappitelli, "Hindering biofilm formation with zosteric acid," *Biofouling*, vol. 26, no. 6, pp. 739–752, 2010.

[77] B. Z. Newby, T. Cutright, C. A. Barrios, and Q. Xu, "Zosteric acid—an effective antifoulant for reducing fresh water bacterial attachment on coatings," *JCT research*, vol. 3, no. 1, pp. 69–76, 2006.

[78] Q. Xu, C. A. Barrios, T. Cutright, and B.-m. Zhang Newby, "Evaluation of toxicity of capsaicin and zosteric acid and their potential application as antifoulants," *Environmental Toxicology: An International Journal*, vol. 20, no. 5, pp. 467–474, 2005.

[79] "The first green, non-toxic antifouling agent for sealants, coatings and paints to transform the construction and marine industries." *European Commission; Cordis*, `https://cordis.europa.eu/project/id/958730`, 2020, Accessed: 10/03/2022.

[80] S. Szunerits and R. Boukherroub, "Antibacterial activity of graphene-based materials," *Journal of Materials Chemistry B*, vol. 4, no. 43, pp. 6892–6912, 2016.

[81] O. A. Amariutei, R. Ramsdale-Capper, M. Correa Álvarez, L. K. Chan, and J. P. Foreman, "Modelling the properties of a difunctional epoxy resin cured with aromatic diamine isomers," *Polymer*, vol. 156, pp. 203–213, 2018.

[82] A. L. Da Róz, M. Ferreira, F. de Lima Leite, and O. N. Oliveira, "9 - carbon-based nanomaterials," in *Nanostructures*, pp. 233–249, William Andrew Publishing, 2017.

[83] A. K. Geim, "Graphene: status and prospects," *science*, vol. 324, no. 5934, pp. 1530–1534, 2009.

[84] Y. Zhu, S. Murali, W. Cai, X. Li, J. W. Suk, J. R. Potts, and R. S. Ruoff, "Graphene and graphene oxide: synthesis, properties, and applications," *Advanced materials*, vol. 22, no. 35, pp. 3906–3924, 2010.

[85] C. Lee, X. Wei, J. W. Kysar, and J. Hone, "Measurement of the elastic properties and intrinsic strength of monolayer graphene," *Science*, vol. 321, no. 5887, pp. 385–388, 2008.

[86] Z. Li, Y. Wang, A. Kozbial, G. Shenoy, F. Zhou, R. McGinley, P. Ireland, B. Morganstein, A. Kunkel, S. P. Surwade, *et al.*, "Effect of airborne contaminants on the

wettability of supported graphene and graphite," *Nature Materials*, vol. 12, no. 10, pp. 925–931, 2013.

[87] J. A. Luceño-Sánchez, G. Maties, C. Gonzalez-Arellano, and A. M. Diez-Pascual, "Synthesis and characterization of graphene oxide derivatives via functionalization reaction with hexamethylene diisocyanate," *Nanomaterials*, vol. 8, no. 11, p. 870, 2018.

[88] N. Neuberger, H. Adidharma, and M. Fan, "Graphene: A review of applications in the petroleum industry," *Journal of Petroleum Science and Engineering*, vol. 167, pp. 152–159, 2018.

[89] B. H. Nguyen and V. H. Nguyen, "Promising applications of graphene and graphene-based nanostructures," *Advances in Natural Sciences: Nanoscience and Nanotechnology*, vol. 7, no. 2, p. 023002, 2016.

[90] C. K. A. Silva and A. K. Alves, "Graphene application," *Technological Applications of Nanomaterials*, pp. 195–206, 2021.

[91] A. Geim, "Graphene prehistory," *Physica Scripta*, vol. 2012, no. T146, p. 014003, 2012.

[92] S. K. Krishnan, E. Singh, P. Singh, M. Meyyappan, and H. S. Nalwa, "A review on graphene-based nanocomposites for electrochemical and fluorescent biosensors," *Rsc Advances*, vol. 9, no. 16, pp. 8778–8781, 2019.

[93] D. A. Dikin, S. Stankovich, E. J. Zimney, R. D. Piner, G. H. Dommett, G. Evmenenko, S. T. Nguyen, and R. S. Ruoff, "Preparation and characterization of graphene oxide paper," *Nature*, vol. 448, no. 7152, pp. 457–460, 2007.

[94] T. Nakajima and Y. Matsuo, "Formation process and structure of graphite oxide," *Carbon*, vol. 32, no. 3, pp. 469–475, 1994.

[95] L. Serrano-Luján, S. Víctor-Román, C. Toledo, O. Sanahuja-Parejo, A. E. Mansour, J. Abad, A. Amassian, A. M. Benito, W. K. Maser, and A. Urbina, "Environmental impact of the production of graphene oxide and reduced graphene oxide," *Sn Applied Sciences*, vol. 1, no. 2, p. 179, 2019.

[96] B. D. Malhotra, S. Srivastava, and S. Augustine, "Biosensors for food toxin detection: carbon nanotubes and graphene," *MRS Online Proceedings Library*, vol. 1725, 2015.

[97] H. Jin, W. Bing, L. Tian, P. Wang, and J. Zhao, "Combined effects of color and elastic modulus on antifouling performance: A study of graphene oxide/silicone rubber composite membranes," *Materials*, vol. 12, no. 16, p. 2608, 2019.

[98] S. Verma, S. Mohanty, and S. Nayak, "Preparation of hydrophobic epoxy–polydimethylsiloxane–graphene oxide nanocomposite coatings for antifouling application," *Soft Matter*, vol. 16, no. 5, pp. 1211–1226, 2020.

[99] W. Sun and F.-G. Wu, "Two-dimensional materials for antimicrobial applications: Graphene materials and beyond," *Chemistry–An Asian Journal*, vol. 13, no. 22, pp. 3378–3410, 2018.

[100] W. Hu, C. Peng, W. Luo, M. Lv, X. Li, D. Li, Q. Huang, and C. Fan, "Graphene-based antibacterial paper," *Acs Nano*, vol. 4, no. 7, pp. 4317–4323, 2010.

[101] V. T. Pham, V. K. Truong, M. D. Quinn, S. M. Notley, Y. Guo, V. A. Baulin, M. Al Kobaisi, R. J. Crawford, and E. P. Ivanova, "Graphene induces formation of pores that kill spherical and rod-shaped bacteria," *Acs Nano*, vol. 9, no. 8, pp. 8458–8467, 2015.

[102] X. Zou, L. Zhang, Z. Wang, and Y. Luo, "Mechanisms of the antimicrobial activities of graphene materials," *Journal of the american chemical society*, vol. 138, no. 7, pp. 2064–2077, 2016.

[103] A. áde Leon *et al.*, "On the antibacterial mechanism of graphene oxide (go) langmuir–blodgett films," *Chemical communications*, vol. 51, no. 14, pp. 2886–2889, 2015.

[104] M. Dallavalle, M. Calvaresi, A. Bottoni, M. Melle-Franco, and F. Zerbetto, "Graphene can wreak havoc with cell membranes," *ACS applied materials & interfaces*, vol. 7, no. 7, pp. 4406–4414, 2015.

[105] K. Krishnamoorthy, N. Umasuthan, R. Mohan, J. Lee, and S.-J. Kim, "Antibacterial activity of graphene oxide nanosheets," *Science of Advanced Materials*, vol. 4, no. 11, pp. 1111–1117, 2012.

[106] S. Gurunathan, J. W. Han, A. A. Dayem, V. Eppakayala, and J.-H. Kim, "Oxidative stress-mediated antibacterial activity of graphene oxide and reduced graphene oxide in pseudomonas aeruginosa," *International journal of nanomedicine*, vol. 7, p. 5901, 2012.

[107] S. Gurunathan, J. W. Han, A. A. Dayem, V. Eppakayala, M.-R. Park, D.-N. Kwon, and J.-H. Kim, "Antibacterial activity of dithiothreitol reduced graphene oxide," *Journal of Industrial and Engineering Chemistry*, vol. 19, no. 4, pp. 1280–1288, 2013.

[108] S. Romero-Vargas Castrillón, F. Perreault, A. F. De Faria, and M. Elimelech, "Interaction of graphene oxide with bacterial cell membranes: insights from force spectroscopy," *Environmental Science & Technology Letters*, vol. 2, no. 4, pp. 112–117, 2015.

[109] P. Kumar, P. Huo, R. Zhang, and B. Liu, "Antibacterial properties of graphene-based nanomaterials," *Nanomaterials*, vol. 9, no. 5, p. 737, 2019.

[110] A. B. Seabra, A. J. Paula, R. de Lima, O. L. Alves, and N. Durán, "Nanotoxicity of graphene and graphene oxide," *Chemical research in toxicology*, vol. 27, no. 2, pp. 159–168, 2014.

[111] C. Liao, Y. Li, and S. C. Tjong, "Graphene nanomaterials: Synthesis, biocompatibility, and cytotoxicity," *International journal of molecular sciences*, vol. 19, no. 11, p. 3564, 2018.

[112] G. Gollavelli and Y.-C. Ling, "Multi-functional graphene as an in vitro and in vivo imaging probe," *Biomaterials*, vol. 33, no. 8, pp. 2532–2545, 2012.

[113] Y. Zhang, S. F. Ali, E. Dervishi, Y. Xu, Z. Li, D. Casciano, and A. S. Biris, "Cytotoxicity effects of graphene and single-wall carbon nanotubes in neural phaeochromocytoma-derived pc12 cells," *ACS nano*, vol. 4, no. 6, pp. 3181–3186, 2010.

[114] K. Wang, J. Ruan, H. Song, J. Zhang, Y. Wo, S. Guo, and D. Cui, "Biocompatibility of graphene oxide," *Nanoscale Res Lett*, vol. 6, no. 1, pp. 1–8, 2011.

[115] A. Krivda, T. Tanaka, M. Frechette, J. Castellon, D. Fabiani, G. Montanari, R. Gorur, P. Morshuis, S. Gubanski, J. Kindersberger, *et al.*, "Characterization of epoxy microcomposite and nanocomposite materials for power engineering applications," *IEEE Electrical Insulation Magazine*, vol. 28, no. 2, pp. 38–51, 2012.

[116] M. Naeem, H. C. Kuan, A. Michelmore, Q. Meng, A. Qiu, M. Aakyiir, D. Losic, S. Zhu, and J. Ma, "A new method for preparation of functionalized graphene and its epoxy nanocomposites," *Composites Part B: Engineering*, vol. 196, 2020.

[117] J. Tang, H. Zhou, Y. Liang, X. Shi, X. Yang, and J. Zhang, "Properties of graphene oxide/epoxy resin composites," *Journal of Nanomaterials*, vol. 2014, p. 696859, 2014.

[118] Y. Chen, L. Jin, and Y. Xie, "Sol-gel processing of organic-inorganic nanocomposite protective coatings," *Journal of Sol-Gel Science and Technology*, vol. 13, no. 1, pp. 735–738, 1998.

[119] M. Borlaf and R. Moreno, "Colloidal sol-gel: A powerful low-temperature aqueous synthesis route of nanosized powders and suspensions," *Open Ceramics*, vol. 8, pp. 100–200, 2021.

[120] G. Cao, *Nanostructures & nanomaterials: synthesis, properties & applications*. Imperial college press, 2004.

[121] A. D. de Oliveira and C. A. G. Beatrice, "Polymer nanocomposites with different types of nanofiller," *Nanocomposites-recent evolutions*, pp. 103–104, 2018.

[122] A. Mtibe, T. H. Mokhothu, M. J. John, T. C. Mokhena, and M. J. Mochane, "Chapter 8 - fabrication and characterization of various engineered nanomaterials," in *Handbook of Nanomaterials for Industrial Applications*, Micro and Nano Technologies, pp. 151–171, Elsevier, 2018.

[123] A. Naz, A. Kausar, M. Siddiq, and M. A. Choudhary, "Comparative review on structure, properties, fabrication techniques, and relevance of polymer nanocomposites reinforced with carbon nanotube and graphite fillers," *Polymer-Plastics Technology and Engineering*, vol. 55, no. 2, pp. 171–198, 2016.

[124] D. Qi, C. Liu, Z. Chen, G. Dong, and Z. Cao, "In situ emulsion copolymerization of methyl methacrylate and butyl acrylate in the presence of sio2 with various surface coupling densities," *Colloid and Polymer Science*, vol. 293, no. 2, pp. 463–471, 2015.

[125] C. I. Jo, J. Ko, Z. Yin, Y.-J. Kim, and Y. S. Kim, "Solvent-free and highly transparent sio2 nanoparticle–polymer composite with an enhanced moisture barrier property," *Industrial & Engineering Chemistry Research*, vol. 55, no. 35, pp. 9433–9439, 2016.

[126] F. Passador, A. Ruvolo-Filho, and L. Pessan, "Nanocomposites of polymer matrices and lamellar clays," in *Nanostructures*, pp. 187–207, Elsevier, 2017.

[127] X.-J. Shen, X.-Q. Pei, S.-Y. Fu, and K. Friedrich, "Significantly modified tribological performance of epoxy nanocomposites at very low graphene oxide content," *Polymer*, vol. 54, no. 3, pp. 1234–1242, 2013.

[128] T. Kuilla, S. Bhadra, D. Yao, N. H. Kim, S. Bose, and J. H. Lee, "Recent advances in graphene based polymer composites," *Progress in polymer science*, vol. 35, no. 11, pp. 1350–1375, 2010.

[129] Y. Geng, S. J. Wang, and J.-K. Kim, "Preparation of graphite nanoplatelets and graphene sheets," *Journal of colloid and interface science*, vol. 336, no. 2, pp. 592–598, 2009.

[130] I. Zaman, H.-C. Kuan, Q. Meng, A. Michelmore, N. Kawashima, T. Pitt, L. Zhang, S. Gouda, L. Luong, and J. Ma, "A facile approach to chemically modified graphene and its polymer nanocomposites," *Advanced Functional Materials*, vol. 22, no. 13, pp. 2735–2743, 2012.

[131] H. J. Salavagione, M. A. Gomez, and G. Martinez, "Polymeric modification of graphene through esterification of graphite oxide and poly (vinyl alcohol)," *Macromolecules*, vol. 42, no. 17, pp. 6331–6334, 2009.

[132] S. Stankovich, R. D. Piner, X. Chen, N. Wu, S. T. Nguyen, and R. S. Ruoff, "Stable aqueous dispersions of graphitic nanoplatelets via the reduction of exfoliated graphite oxide in the presence of poly (sodium 4-styrenesulfonate)," *Journal of Materials Chemistry*, vol. 16, no. 2, pp. 155–158, 2006.

[133] X. Shi, T. A. Nguyen, Z. Suo, Y. Liu, and R. Avci, "Effect of nanoparticles on the anticorrosion and mechanical properties of epoxy coating," *Surface and Coatings Technology*, vol. 204, no. 3, pp. 237–245, 2009.

[134] "Epikote resin 828 product data sheet." *Hexion*, `https://www.hexion.com/CustomServices/PDFDownloader.aspx?type=tds&pid=f2b9343c-5814-6fe3-ae8a-ff0300fcd525`, Accessed: 15/03/2022.

[135] S. Ma, X. Liu, L. Fan, Y. Jiang, L. Cao, Z. Tang, and J. Zhu, "Synthesis and properties of a bio-based epoxy resin with high epoxy value and low viscosity," *Chemsuschem*, vol. 7, no. 2, pp. 555–562, 2014.

[136] "Poly(propylene glycol) bis(2-aminopropyl ether)." *Sigma Aldrich*, `https://www.sigmaaldrich.com/NO/en/product/aldrich/406694`, 2021, Accessed: 27/04/2022.

[137] N. A. St John and G. A. George, "Cure kinetics and mechanisms of a tetraglycidyl-4,4-diaminodiphenylmethane/diaminodiphenylsulphone epoxy resin using near i.r. spectroscopy," *Polymer*, vol. 33, no. 13, pp. 2679–2688, 1992.

[138] F. Torrens Zaragozá *et al.*, "Polymer bisphenol-a, the incorporation of silica nanospheres into epoxy–amine materials and polymer nanocomposites," *Nereis*, no. 3, pp. 17–23, 2011.

[139] C. Schlaich, M. Li, C. Cheng, I. S. Donskyi, L. Yu, G. Song, E. Osorio, Q. Wei, and R. Haag, "Mussel-inspired polymer-based universal spray coating for surface modification: fast fabrication of antibacterial and superhydrophobic surface coatings," *Advanced Materials Interfaces*, vol. 5, no. 5, 2018.

[140] I. Rosadi, N. F. Khusnah, and S. P. Sakti, "Real-time monitoring system for polystyrene coating material deposition onto qcm sensor using ultrasonic atomizer spray," *Journal of Physics: Conference Series*, vol. 1153, no. 1, p. 012042, 2019.

[141] S. Ebnesajjad and A. H. Landrock, "Chapter 8 - adhesive applications and bonding processes," in *Adhesives Technology Handbook (Third Edition)* (S. Ebnesajjad and A. H. Landrock, eds.), pp. 206–234, Boston: William Andrew Publishing, third edition ed., 2015.

[142] "A short round-up of the latest trends concerning marine coatings, and the most optimum spraying methods." *Graco, Industrial, Manufacturing Processing*, https://www.graco.com/gb/en/in-plant-manufacturing/solutions/articles/coatings-for-the-marine-industry.html, 2021, Accessed: 04/04/2022.

[143] C. Chet, "What are the differences between airless air sprayers?." https://www.hunker.com/13408036/what-are-the-differences-between-airless-air-sprayers, 2021, Accessed: 04/04/2022.

[144] R. Parkhill, E. Knobbe, and M. Donley, "Application and evaluation of environmentally compliant spray-coated ormosil films as corrosion resistant treatments for aluminum 2024-t3," *Progress in Organic Coatings*, vol. 41, no. 4, pp. 261–265, 2001. Keystone Special issue.

[145] A. Fridrihsone-Girone, U. Stirna, M. Misāne, B. Lazdiņa, and L. Deme, "Spray-applied 100% volatile organic compounds free two component polyurethane coatings based on rapeseed oil polyols," *Progress in Organic Coatings*, vol. 94, pp. 90–97, 2016.

[146] R. R. Matheson, "20th- to 21st-century technological challenges in soft coatings," *Science*, vol. 297, no. 5583, pp. 976–979, 2002.

[147] S. K. Sahoo, B. Manoharan, and N. Sivakumar, "Chapter 1 - introduction: Why perovskite and perovskite solar cells?," in *Perovskite Photovoltaics*, pp. 1–24, Academic Press, 2018.

[148] D. R. Ceratti, B. Louis, X. Paquez, M. Faustini, and D. Grosso, "A new dip coating method to obtain large-surface coatings with a minimum of solution," *Advanced Materials*, vol. 27, no. 34, pp. 4958–4962, 2015.

[149] V. S. Nguyen, D. Rouxel, and B. Vincent, "Dispersion of nanoparticles: From organic solvents to polymer solutions," *Ultrasonics Sonochemistry*, vol. 21, no. 1, pp. 149–153, 2014.

[150] A. Tinke, R. Govoreanu, I. Weuts, K. Vanhoutte, and D. De Smaele, "A review of underlying fundamentals in a wet dispersion size analysis of powders," *Powder technology*, vol. 196, no. 2, pp. 102–114, 2009.

[151] "The interaction of colloids zeta potential : A complete course in 5 minutes," *Zeta Meter*, 1997.

[152] T. Phenrat, P. Skácelová, E. Petala, A. Velosa, and J. Filip, "Nanoscale zero-valent iron particles for water treatment: From basic principles to field-scale applications," in *Advanced Nano-Bio Technologies for Water and Soil Treatment*, pp. 19–52, Springer, 2020.

[153] G. Cao and Y. Wang, *Nanostructures and Nanomaterials*. World Scientific, 2nd ed., 2011.

[154] F. Matter, A. L. Luna, and M. Niederberger, "From colloidal dispersions to aerogels: How to master nanoparticle gelation," *Nano Today*, vol. 30, p. 100827, 2020.

[155] B. Derjaguin and L. Landau, "Theory of the stability of strongly charged lyophobic sols and of the adhesion of strongly charged particles in solutions of electrolytes," *Progress in Surface Science*, vol. 43, no. 1-4, pp. 30–59, 1993.

[156] E. J. W. Verwey, "Theory of the stability of lyophobic colloids.," *The Journal of Physical Chemistry*, vol. 51, no. 3, pp. 631–636, 1947.

[157] A. Standard *et al.*, "Zeta potential of colloids in water and waste water," *ASTM Standard D*, vol. 1985, p. 4187, 1985.

[158] G. W. Lu and P. Gao, "Chapter 3 - emulsions and microemulsions for topical and transdermal drug delivery," in *Handbook of Non-Invasive Drug Delivery Systems* (V. S. Kulkarni, ed.), Personal Care Cosmetic Technology, pp. 59–94, Boston: William Andrew Publishing, 2010.

[159] K. Pate and P. Safier, "12 - chemical metrology methods for cmp quality," in *Advances in Chemical Mechanical Planarization*, pp. 299–325, Woodhead Publishing, 2016.

[160] L. M. Liz-Marzán, M. A. Correa-Duarte, I. Pastoriza-Santos, P. Mulvaney, T. Ung, M. Giersig, and N. A. Kotov, "Chapter 5 - core-shell nanoparticles and assemblies thereof," *Handbook of Surfaces and Interfaces of Materials*, pp. 189–237, 2001.

[161] M. Ivanov and D. Ivanov, "Nanodiamond nanoparticles as additives to lubricants," in *Ultrananocrystalline Diamond: Synthesis, Properties and Applications: Second Edition*, pp. 457–492, 2012.

[162] A. A. Iqbal, N. Sakib, A. K. Iqbal, and D. M. Nuruzzaman, "Graphene-based nanocomposites and their fabrication, mechanical properties and applications," *Materialia*, vol. 12, p. 100815, 2020.

[163] W. W. Liu, J. N. Wang, and X. X. Wang, "Charging of unfunctionalized graphene in organic solvents," *Nanoscale*, vol. 4, no. 2, pp. 425–428, 2012.

[164] H. Wang, S. Lu, Y. Zhang, F. Lan, X. Lu, and Y. Xiang, "Pristine graphene dispersion in solvents and its application as a catalyst support: a combined theoretical and experimental study," *Journal of Materials Chemistry A*, vol. 3, no. 12, pp. 6282–6285, 2015.

[165] R. Navik, Y. Gai, W. Wang, and Y. Zhao, "Curcumin-assisted ultrasound exfoliation of graphite to graphene in ethanol," *Ultrasonics Sonochemistry*, vol. 48, pp. 96–102, 2018.

[166] M. Lotya, Y. Hernandez, P. J. King, R. J. Smith, V. Nicolosi, L. S. Karlsson, F. M. Blighe, S. De, Z. Wang, I. McGovern, *et al.*, "Liquid phase production of graphene by exfoliation of graphite in surfactant/water solutions," *Journal of the American Chemical Society*, vol. 131, no. 10, pp. 3611–3620, 2009.

[167] M. Lotya, P. J. King, U. Khan, S. De, and J. N. Coleman, "High-concentration, surfactant-stabilized graphene dispersions," *ACS nano*, vol. 4, no. 6, pp. 3155–3162, 2010.

[168] A. Mehmood, N. M. Mubarak, M. Khalid, P. Jagadish, R. Walvekar, and E. C. Abdullah, "Graphene/pva buckypaper for strain sensing application," *Scientific Reports*, vol. 10, no. 1, p. 20106, 2020.

[169] M. S. Khan, A. Shakoor, G. T. Khan, S. Sultana, and A. Zia, "A study of stable graphene oxide dispersions in various solvents.," *Journal of the Chemical Society of Pakistan*, vol. 37, no. 1, 2015.

[170] J. Paredes, S. Villar-Rodil, A. Martínez-Alonso, and J. Tascon, "Graphene oxide dispersions in organic solvents," *Langmuir*, vol. 24, no. 19, pp. 10560–10564, 2008.

[171] F. Momen-Heravi, L. Balaj, S. Alian, A. J. Trachtenberg, F. H. Hochberg, J. Skog, and W. P. Kuo, "Impact of biofluid viscosity on size and sedimentation efficiency of the isolated microvesicles," *Frontiers in physiology*, vol. 3, p. 162, 2012.

[172] J. Abraham, T. Sharika, R. Mishra, and S. Thomas, "14 - rheological characteristics of nanomaterials and nanocomposites," in *Micro and Nano Fibrillar Composites from Polymer Blends*, Woodhead Publishing Series in Composites Science and Engineering, pp. 327–350, 2017.

[173] N. Phan-Thien and N. Mai-Duy, *Understanding viscoelasticity: an introduction to rheology*. Springer, 2013.

[174] I. S. Fancher and I. Levitan, "Chapter three - endothelial inwardly-rectifying k+ channels as a key component of shear stress-induced mechanotransduction," in *Ion Chan-*

nels and Calcium Signaling in the Microcirculation, vol. 85 of *Current Topics in Membranes*, pp. 59–88, Academic Press, 2020.

[175] P. Reynolds, "The chemistry and physics of coatings, ch.3 the rheology of coatings," *Royal Society of Chemistry*, p. 30, 2004.

[176] R. S. Subramanian, "Non-newtonian flows," *Department of Chemical and Biomolecular Engineering, Clarkson University*, 2002.

[177] H. J. Skadsem and A. Saasen, "Concentric cylinder viscometer flows of herschel-bulkley fluids," *Applied Rheology*, vol. 29, no. 1, pp. 173–181, 2019.

[178] C. K. Schoff, "Optimum viscosity for paint application." *American Coating Association*, `https://www.paint.org/coatingstech-magazine/articles/optimum-viscosity-paint-application/`, Accessed: 04/04/2022.

[179] W. M. Haynes, D. R. Lide, and T. J. Bruno, "Ethanol, crc handbook of chemistry and physics," *CRC press, Boca Raton*, 2016.

[180] H. HL, "Acetone, kirk-othmer encyclopedia of chemical technology," *J. Wiley & Sons: New York*, 1999-2015.

[181] B. H. Stuart, "Infrared spectroscopy: fundamentals and applications," *John Wiley & Sons*, 2004.

[182] J. Coates, "Interpretation of infrared spectra, a practical approach," *Citeseer*, 2000.

[183] S. Vahur, A. Teearu, P. Peets, L. Joosu, and I. Leito, "Atr-ft-ir spectral collection of conservation materials in the extended region of 4000-80 cm–1," *Analytical and Bioanalytical Chemistry*, vol. 408, no. 13, pp. 3373–3379, 2016.

[184] T. Winterstein, M. Staab, C. Nakic, H.-J. Feige, J. Vogel, and H. F. Schlaak, "Su-8 electrothermal actuators: Optimization of fabrication and excitation for long-term use," *Micromachines*, vol. 5, no. 4, pp. 1310–1322, 2014.

[185] K. Krishnamoorthy, K. Jeyasubramanian, M. Premanathan, G. Subbiah, H. S. Shin, and S. J. Kim, "Graphene oxide nanopaint," *Carbon*, vol. 72, pp. 328–337, 2014.

[186] K. Sato, "The hardness of coating films," *Progress in Organic Coatings*, vol. 8, no. 1, pp. 1–18, 1980.

[187] A. C. Fischer-Cripps, "Nanoindentation," *Springer*, pp. 22–140, 2004.

[188] S. Hainsworth, H. Chandler, and T. Page, "Analysis of nanoindentation load-displacement loading curves," *Journal of Materials Research*, vol. 11, no. 8, pp. 1987–1995, 1996.

[189] R. D. Dukino and M. V. Swain, "Comparative measurement of indentation fracture toughness with berkovich and vickers indenters," *Journal of the American Ceramic Society*, vol. 75, no. 12, pp. 3299–3304, 1992.

[190] I. Oral, H. Guzel, and G. Ahmetli, "Determining the mechanical properties of epoxy resin (dgeba) composites by ultrasonic velocity measurement," *Journal of Applied Polymer Science*, vol. 127, no. 3, pp. 1667–1675, 2013.

[191] E. Ivanov, R. Kotsilkova, A. Paddubskaya, A. Pliushch, S. Bellucci, A. Celzard, and V. Fierro, "Nanomechanical properties of epoxy composites with carbon fillers," 2013.

[192] J. Sekler, P. Steinmann, and H. Hintermann, "The scratch test: Different critical load determination techniques," *Surface and Coatings Technology*, vol. 36, no. 1-2, pp. 519–529, 1988.

[193] X. Wang, P. Xu, R. Han, J. Ren, L. Li, N. Han, F. Xing, and J. Zhu, "A review on the mechanical properties for thin film and block structure characterised by using nanoscratch test," *Nanotechnology Reviews*, vol. 8, no. 1, pp. 628–644, 2019.

[194] E. P. Koumoulos, P. Jagadale, A. Lorenzi, A. Tagliaferro, and C. A. Charitidis, "Evaluation of surface properties of epoxy–nanodiamonds composites," *Composites Part B: Engineering*, vol. 80, pp. 27–36, 2015.

[195] N. Tayebi, T. F. Conry, and A. A. Polycarpou, "Determination of hardness from nanoscratch experiments: Corrections for interfacial shear stress and elastic recovery," *Journal of materials research*, vol. 18, no. 9, pp. 2150–2162, 2003.

[196] P. Sampathkumaran, S. Seetharamu, S. Vynatheya, A. Murali, R. Kumar, *et al.*, "Sem observations of the effects of velocity and load on the sliding wear characteristics of glass fabric–epoxy composites with different fillers," *Wear*, vol. 237, no. 1, pp. 20–27, 2000.

[197] S. Li, J. Zhang, M. Liu, R. Wang, and L. Wu, "Influence of polyethyleneimine functionalized graphene on tribological behavior of epoxy composite," *Polymer Bulletin*, vol. 78, no. 11, pp. 6493–6515, 2021.

[198] S. W. Koh, H. J. Kim, J. D. Kim, B. T. Kim, S. O. Hwang, and W. S. Choi, "Effect of load on the abrasive wear of silica-filled epoxy resin composites," in *Materials science forum*, vol. 544, pp. 255–258, 2007.

[199] H. Zhang, X. Li, W. Qian, J. Zhu, B. Chen, J. Yang, and Y. Xia, "Characterization of mechanical properties of epoxy/nanohybrid composites by nanoindentation," *Nanotechnology Reviews*, vol. 9, no. 1, pp. 28–40, 2020.

[200] S. Zhang, J. Yang, B. Chen, S. Guo, J. Li, and C. Li, "One-step hydrothermal synthesis of reduced graphene oxide/zinc sulfide hybrids for enhanced tribological properties of epoxy coatings," *Surface and Coatings Technology*, vol. 326, pp. 87–95, 2017.

[201] N. Gafsi, R. Verdejo, M. Kharrat, M. Barletta, M. Á. López-Manchado, and M. Dammak, "Effect of filler content on scratch behavior and tribological performance of polyester/graphene oxide nanocomposite coating," *Journal of Coatings Technology and Research*, vol. 18, no. 5, pp. 1269–1280, 2021.

[202] B. Pan, S. Zhang, W. Li, J. Zhao, J. Liu, Y. Zhang, and Y. Zhang, "Tribological and mechanical investigation of mc nylon reinforced by modified graphene oxide," *Wear*, vol. 294, pp. 395–401, 2012.

[203] O. Knudsen and A. Forsgren, *Corrosion control through organic coatings, second edition*. CRC Press, 2017.

[204] J. C. Bolger, "Acid base interactions between oxide surfaces and polar organic compounds," in *Adhesion Aspects of Polymeric Coatings*, pp. 3–18, Springer, 1983.

[205] G. Tesoro and Y. Wu, "Silane coupling agents: the role of the organofunctional group," *Journal of adhesion science and technology*, vol. 5, no. 10, pp. 771–784, 1991.

[206] A. Baldan, "Adhesion phenomena in bonded joints," *International Journal of Adhesion and Adhesives*, vol. 38, pp. 95–116, 2012.

[207] M. Islam, L. Tong, and P. Falzon, "Influence of metal surface preparation on its surface profile, contact angle, surface energy and adhesion with glass fibre prepreg," *International Journal of Adhesion and Adhesives*, vol. 51, pp. 32–41, 2014.

[208] A. Grigore, S. Spallek, A. Petschelt, B. Butz, E. Spiecker, and U. Lohbauer, "Microstructure of veneered zirconia after surface treatments: A tem study," *Dental Materials*, vol. 29, no. 11, pp. 1098–1107, 2013.

[209] "Surface preparation and protective coating." *NORSOK Standard*, `https://www.standard.no/pagefiles/1164/m-cr-501r1.pdf`, 1994, Accessed: 31/03/2022.

[210] M. Charbonnier and M. Romand, "Polymer pretreatments for enhanced adhesion of metals deposited by the electroless process," *International Journal of Adhesion and Adhesives*, vol. 23, no. 4, pp. 277–285, 2003.

[211] G. Rogers, "Coating instrument series: Test instruments for coating adhesion," *Materials Performance*, vol. 42, no. 7, pp. 40–44, 2003.

[212] R. Zakaria and A. H. Ahmad, "Adhesion and hardness evaluation of modified silicone-dammar as natural coating materials," *American Journal of Applied Sciences*, vol. 9, no. 6, pp. 890–893, 2012.

[213] H. Wei and J. e. a. Xia, "Adhesion and cohesion of epoxy-based industrial composite coatings," *Composites Part B: Engineering*, vol. 193, p. 108035, 2020.

[214] E. Holm, M. Schultz, E. Haslbeck, W. Talbott, and A. Field, "Evaluation of hydrodynamic drag on experimental fouling-release surfaces, using rotating disks," *Biofouling*, vol. 20, no. 4-5, pp. 219–226, 2004.

[215] A. Scardino, H. Zhang, D. Cookson, R. Lamb, and R. d. Nys, "The role of nano-roughness in antifouling," *Biofouling*, vol. 25, no. 8, pp. 757–767, 2009.

[216] M. V. Graham, A. P. Mosier, T. R. Kiehl, A. E. Kaloyeros, and N. C. Cady, "Development of antifouling surfaces to reduce bacterial attachment," *Soft Matter*, vol. 9, no. 27, pp. 6235–6244, 2013.

[217] T. Asakura, "Surface roughness measurement," *Speckle metrology*, pp. 11–49, 1978.

[218] P. Russell, D. Batchelor, and J. Thornton, "Sem and afm: complementary techniques for high resolution surface investigations," *Veeco Metrology Group*, 2001.

[219] L. Podgorski, B. Chevet, L. Onic, and A. Merlin, "Modification of wood wettability by plasma and corona treatments," *International journal of adhesion and adhesives*, vol. 20, no. 2, pp. 103–111, 2000.

[220] S. Cao, J. Wang, H. Chen, and D. Chen, "Progress of marine biofouling and antifouling technologies," *Chinese Science Bulletin*, vol. 56, no. 7, pp. 598–612, 2011.

[221] K. M. Praveen, C. Pious, S. Thomas, and Y. Grohens, "Chapter 1 - relevance of plasma processing on polymeric materials and interfaces," in *Non-Thermal Plasma Technology for Polymeric Materials*, pp. 1–21, Elsevier, 2019.

[222] Y. Yuan and T. R. Lee, "Contact angle and wetting properties," *Springer Series in Surface Sciences*, vol. 51, no. 1, pp. 3–34, 2013.

[223] A. Lafuma and D. Quéré, "Superhydrophobic states," *Nature materials*, vol. 2, no. 7, pp. 457–460, 2003.

[224] J. Drelich, "Guidelines to measurements of reproducible contact angles using a sessile-drop technique," *Surface innovations*, vol. 1, no. 4, pp. 248–254, 2013.

[225] R. Johnson Jr and R. Dettre, "Surface colloid science," *E. Matijevic, Ed*, vol. 2, p. 85, 1969.

[226] "What is surface free energy?." *Biolin Scientific*, https://www.biolinscientific.com/blog/what-is-surface-free-energy, 2021, Accessed: 21/04/2022.

[227] A. Ranowsky, "Contact angle and surface tension - a fascinating liaison." *CSC Scientific Company*, https://www.cscscientific.com/csc-scientific-blog/how-does-contact-angle-relate-to-surface-tension, 2016, Accessed: 21/04/2022.

[228] D. K. Owens and R. Wendt, "Estimation of the surface free energy of polymers," *Journal of applied polymer science*, vol. 13, no. 8, pp. 1741–1747, 1969.

[229] M. Annamalai, K. Gopinadhan, S. A. Han, S. Saha, H. J. Park, E. B. Cho, B. Kumar, A. Patra, S.-W. Kim, and T. Venkatesan, "Surface energy and wettability of van der waals structures," *Nanoscale*, vol. 8, no. 10, pp. 5764–5770, 2016.

[230] R. Rogowska, "Surface free energy of thin-layer coatings deposited by means of the arc-vacuum method," *Problemy Eksploatacji*, pp. 193–203, 2006.

[231] E. C. Combe, B. A. Owen, and J. S. Hodges, "A protocol for determining the surface free energy of dental materials," *Dental Materials*, vol. 20, no. 3, pp. 262–268, 2004.

[232] L. Holysz, "Surface free energy components of silica gel determined by the thin layer wicking method for different layer thicknesses of gel," *Journal of materials science*, vol. 33, no. 2, pp. 445–452, 1998.

[233] G. Macdougall and C. Ockrent, "Surface energy relations in liquid/solid systems i. the adhesion of liquids to solids and a new method of determining the surface tension of liquids," *Proceedings of the Royal Society of London. Series A. Mathematical and Physical Sciences*, vol. 180, no. 981, pp. 151–173, 1942.

[234] A. Rudawska and E. Jacniacka, "Analysis for determining surface free energy uncertainty by the owen-wendt method," *International Journal of Adhesion and Adhesives*, vol. 29, no. 4, pp. 451–457, 2009.

[235] M. Chen, Y. Qu, L. Yang, and H. Gao, "Structures and antifouling properties of low surface energy non-toxic antifouling coatings modified by nano-sio2 powder," *Science in China Series B: Chemistry*, vol. 51, no. 9, pp. 848–852, 2008.

[236] X. Wang, H. Wang, and D. Liu, "Non-toxic low surface energy antifouling coatings," *Paint & Coatings Industry*, vol. 1, 2004.

[237] J. A. Finlay, M. E. Callow, L. K. Ista, G. P. Lopez, and J. A. Callow, "The influence of surface wettability on the adhesion strength of settled spores of the green alga enteromorpha and the diatom amphora," *Integrative and comparative biology*, vol. 42, no. 6, pp. 1116–1122, 2002.

[238] J. Gilron, S. Belfer, P. Väisänen, and M. Nyström, "Effects of surface modification on antifouling and performance properties of reverse osmosis membranes," *Desalination*, vol. 140, no. 2, pp. 167–179, 2001.

[239] L. Xie, F. Hong, C. He, C. Ma, J. Liu, G. Zhang, and C. Wu, "Coatings with a self-generating hydrogel surface for antifouling," *Polymer*, vol. 52, no. 17, pp. 3738–3744, 2011.

[240] I. O. Ucar, C. Elif Cansoy, H. Yildirim Erbil, M. E. Pettitt, M. E. Callow, and J. A. Callow, "Effect of contact angle hysteresis on the removal of the sporelings of the green alga ulva from the fouling-release coatings synthesized from polyolefin polymers," *Biointerphases*, vol. 5, no. 3, pp. 75–84, 2010.

[241] K. C. Anyaogu, A. V. Fedorov, and D. C. Neckers, "Synthesis, characterization, and antifouling potential of functionalized copper nanoparticles," *Langmuir*, vol. 24, no. 8, pp. 4340–4346, 2008.

[242] E. Subramanyam, S. Mohandoss, and H.-W. Shin, "Synthesis, characterization, and evaluation of antifouling polymers of 4-acryloyloxybenzaldehyde with methyl methacrylate," *Journal of applied polymer science*, vol. 112, no. 5, pp. 2741–2749, 2009.

[243] M. Lejars, A. Margaillan, and C. Bressy, "Fouling release coatings: a nontoxic alternative to biocidal antifouling coatings," *Chemical reviews*, vol. 112, no. 8, pp. 4347–4390, 2012.

[244] S. A. Kumar, T. Balakrishnan, M. Alagar, and Z. Denchev, "Development and characterization of silicone/phosphorus modified epoxy materials and their application as anticorrosion and antifouling coatings," *Progress in Organic coatings*, vol. 55, no. 3, pp. 207–217, 2006.

[245] P. J. Molino, E. Campbell, and R. Wetherbee, "Development of the initial diatom microfouling layer on antifouling and fouling-release surfaces in temperate and tropical australia," *Biofouling*, vol. 25, no. 8, pp. 685–694, 2009.

[246] F. Di Caprio, "Methods to quantify biological contaminants in microalgae cultures," *Algal Research*, vol. 49, 2020.

[247] J. S. Patil and A. C. Anil, "Quantification of diatoms in biofilms: standardisation of methods," *Biofouling*, vol. 21, no. 3-4, pp. 181–188, 2005.

[248] B. Riaño, D. Hernández, and M. García-González, "Microalgal-based systems for wastewater treatment: Effect of applied organic and nutrient loading rate on biomass composition," *Ecological Engineering*, vol. 49, pp. 112–117, 2012.

[249] P. P. Assemany, M. L. Calijuri, E. de Aguiar do Couto, M. H. B. de Souza, N. C. Silva, A. da Fonseca Santiago, and J. de Siqueira Castro, "Algae/bacteria consortium in high rate ponds: Influence of solar radiation on the phytoplankton community," *Ecological Engineering*, vol. 77, pp. 154–162, 2015.

[250] R. R. Guillard and M. S. Sieracki, "Counting cells in cultures with the light microscope," *Algal culturing techniques*, pp. 239–252, 2005.

[251] C. Suarez, M. Piculell, O. Modin, S. Langenheder, F. Persson, and M. Hermansson, "Thickness determines microbial community structure and function in nitrifying biofilms via deterministic assembly," *Scientific reports*, vol. 9, no. 1, pp. 1–10, 2019.

[252] S. K. Rajasekharan, S. Ramesh, and D. Bakkiyaraj, "Synergy of flavonoids with hdac inhibitor: new approach to target candida tropicalis biofilms," *Journal of Chemotherapy*, vol. 27, no. 4, pp. 246–249, 2015.

[253] L. E. de Bashan, X. Mayali, B. M. Bebout, P. K. Weber, A. M. Detweiler, J.-P. Hernandez, L. Prufert-Bebout, and Y. Bashan, "Establishment of stable synthetic mutualism without co-evolution between microalgae and bacteria demonstrated by mutual transfer of metabolites and persistent physical association," *Algal research*, vol. 15, pp. 179–186, 2016.

[254] Q. Xie, H. Zeng, Q. Peng, C. Bressy, C. Ma, and G. Zhang, "Self-stratifying silicone coating with nonleaching antifoulant for marine anti-biofouling," *Advanced Materials Interfaces*, vol. 6, no. 13, 2019.

[255] M. Kyllingstad, "Epoxy based coatings with graphene and graphene oxide additions for antifouling applications," *Master's thesis project, Norwegian University of Science and Technology*, 2021.

[256] "Ir spectrum table chart." *Sigma-Aldrich*, `https://www.sigmaaldrich.com/NO/en/technical-documents/technical-article/analytical-chemistry/photometry-and-reflectometry/ir-spectrum-table`, Accessed: 08/05/2022.

[257] X. Liu, "Organic chemistry i: Chapter 6.3 ir spectrum and characteristic abrosption bands," *Kwantlen Polytechnic University*, 2021.

[258] D. L. Schmidt, R. F. Brady, K. Lam, D. C. Schmidt, and M. K. Chaudhury, "Contact angle hysteresis, adhesion, and marine biofouling," *Langmuir*, vol. 20, no. 7, pp. 2830–2836, 2004.

[259] M. Jimenez, H. Hamze, A. Allion, G. Ronse, G. Delaplace, and M. Traisnel, "Antifouling stainless steel surface: competition between roughness and surface energy," in *Materials science forum*, vol. 706, pp. 2523–2528, 2012.

[260] X. Lv, Y. Yang, Y. Tao, Y. Jiang, B. Chen, X. Zhu, Z. Cai, and B. Li, "A mechanism study on toxicity of graphene oxide to daphnia magna: Direct link between bioaccumulation and oxidative stress," *Environmental pollution*, vol. 234, pp. 953–959, 2018.

[261] T. Malina, E. Maršálková, K. Holá, J. Tuček, M. Scheibe, R. Zbořil, and B. Maršálek, "Toxicity of graphene oxide against algae and cyanobacteria: Nanoblade-morphology-induced mechanical injury and self-protection mechanism," *Carbon*, vol. 155, pp. 386–396, 2019.

[262] A. A. Balqadi, A. J. Salama, and S. Satheesh, "Microfouling development on artificial substrates deployed in the central red sea," *Oceanologia*, vol. 60, no. 2, pp. 219–231, 2018.

[263] L. Brand and R. Guillard, "The effects of continuous light and light intensity on the reproduction rates of twenty-two species of marine phytoplankton," *Journal of Experimental Marine Biology and Ecology*, vol. 50, no. 2-3, pp. 119–132, 1981.

[264] D. J. Montagnes and M. Franklin, "Effect of temperature on diatom volume, growth rate, and carbon and nitrogen content: reconsidering some paradigms," *Limnology and oceanography*, vol. 46, no. 8, pp. 2008–2018, 2001.

[265] H.-p. Wang, J. Xia, P. Xie, and M. Dou, "Mechanisms for hydrological factors causing algal blooms in hanjing river- based on kinetics of algae growth," *Resources and Environment in the Yangtze Basin*, vol. 13, no. 3, pp. 282–285, 2004.

[266] S. Spaulding, "How long does a diatom cell live?." *Diatoms of North America*, `https://diatoms.org/news/how-long-does-a-diatom-cell-live`, 2015, Accessed: 28/05/2022.

[267] J. Zhang and D. Jiang, "Molecular dynamics simulation of mechanical performance of graphene/graphene oxide paper based polymer composites," *Carbon*, vol. 67, pp. 784–791, 2014.

[268] S. Bayrak, D. Paulkowski, K. W. Stöckelhuber, B. Staar, and B. Mayer, "A comprehensive study about the role of crosslink density on the tribological behavior of dlc coated rubber," *Materials*, vol. 13, no. 23, p. 5460, 2020.

[269] Z. Zhang, W. Zhang, D. Li, Y. Sun, Z. Wang, C. Hou, L. Chen, Y. Cao, and Y. Liu, "Mechanical and anticorrosive properties of graphene/epoxy resin composites coating prepared by in-situ method," *International journal of molecular sciences*, vol. 16, no. 1, pp. 2239–2251, 2015.

[270] L. Zhang, S. Song, D. Sun, X. Xue, Q. Dai, and Z. Li, "Effects of liquid viscosity on agricultural nozzle droplet parameters," *Agricultural Sciences*, vol. 10, no. 9, pp. 1217–1239, 2019.

[271] I. A. Neacşu, A. I. Nicoara, O. R. Vasile, and B. S. Vasile, "Chapter 9 - inorganic micro- and nanostructured implants for tissue engineering," in *Nanobiomaterials in Hard Tissue Engineering*, pp. 271–295, William Andrew Publishing, 2016.

[272] M. L. Hamilton, "Applications of grazing-angle reflection absorption fourier transform infrared spectroscopy to the analysis of surface contamination," *University of Canterbury, Chemistry*, 2007.

[273] U. A. Méndez-Romero, M. A. Velasco-Soto, L. Licea-Jiménez, J. González-Hernández, and S. A. Pérez-García, "Long-term evolution of the chemical and structural stability of graphene oxide after storage as solid and as aqueous dispersion," *Nano Select*, vol. 2, no. 11, pp. 2168–2175, 2021.

[274] "Pubchem annotation record for tetrahydrofuran." *National Center for Biotechnology Information*, `https://pubchem.ncbi.nlm.nih.gov/source/hsdb/125`, Hazardous Substances Data Bank (HSDB) 2022, Accessed: 26/05/2022.

[275] T. Le Norcy, F. Faÿ, C. Z. Obando, C. Hellio, K. Réhel, and I. Linossier, "A new method for evaluation of antifouling activity of molecules against microalgal biofilms using confocal laser scanning microscopy-microfluidic flow-cells," *International Biodeterioration & Biodegradation*, vol. 139, pp. 54–61, 2019.

[276] "Poly(propylene glycol) bis(2-aminopropyl ether) product specification sheet." *Sigma-Aldrich*, `https://www.sigmaaldrich.com/NO/en/product/aldrich/406651`, Accessed: 05/02/2022.

Appendix

A Calculations

This section presents the calculations relevant for coating preparation, including preparation of epoxy sols and G and GO slurries and the preparation of coating batches applied in the spray coating procedure. Material properties of relevant chemicals are listed in Table A.1.

Table A.1: Material properties of chemicals relevant for coating preparation [134, 179, 180, 276].

Chemical	**Abbreviation**	**Molar mass** Mm [g/mol]	**Density** ρ [g/mL]	**Molar ratio** mr [-]	**Purity** p [-]
Acetone	-	58.08	0.790	-	0.999
Ethanol	EtOH	46.07	0.792	-	0.990
Epikote	E	187.00	1.160	1.0	1.000
PPGBAE	CA	230.00	0.948	0.5	1.000
G-Epikote dispersion	G-E	-	-	-	0.006
GO paste	GO-P	-	-	-	0.100

A.1 Preparation of epoxy sols

The following equation will calculate the required mass of solvent in preparation of epikote sols. The epoxy sols were prepared with a requirement of using a weight ratio of 0.9 of mass solvent compared to mass epikote, wr_s. 60 g mass of epikote, m_E, was used as basis in the preparation of each epoxy sol.

The required mass of solvent, m_s, in the epoxy sol is given by Equation A.1.

$$m_s = m_E \cdot wr_s \quad \text{[g]} \quad \text{(A.1)}$$

Equation A.1 calculates the required mass of acetone in the E1 sol. For the E2 sol, required mass of acetone, $m_{acetone}$, and EtOH, m_{EtOH}, can be calculated by Equation A.2, utilizing the solvent mass ratio of 1:1.

$$m_{acetone} = m_{EtOH} = 0.5 \cdot m_s \quad \text{[g]} \quad \text{(A.2)}$$

Further, the mass percentage of epikote, mp_E, in mixture of epikote and solvent was calculated by,

$$mp_E = \frac{m_E}{m_E + m_s} \quad [-] \quad \text{(A.3)}$$

A.2 Preparations of G and GO slurry

GO slurry

The required mass of GO in the preparation of GO slurries of 0.125 wt%, 0.250 wt% and 0.500 wt% GO compared to mass epikote was calculated based on the equations presented in this section. The equations consider the use of 50 g E2 sol in the GO slurry. In addition, it is assumed that the graphene oxide paste delivered by CealTech AS contains 10 wt% GO.

The amount of epoxy in the GO slurry, $m_{E_{GOslurry}}$, was found by Equation A.4. The equation considers mass percentage of epoxy in E2 sol, found by Equation A.3, and an E2 sol weight, m_{sol} of 50 g.

$$m_{E_{GOslurry}} = mp_E \cdot m_{sol} \quad [g] \quad \text{(A.4)}$$

Equation A.5 was used to calculate the required mass of GO in the GO slurry, $m_{GO_{GOslurry}}$.

$$m_{GO_{GOslurry}} = m_{E_{GOslurry}} \cdot wr_{GO} \quad [g] \quad \text{(A.5)}$$

$m_{E_{GOslurry}}$ was found by Equation A.4 and wr_{GO} represents the chosen weight ratio of GO compared to mass epikote (0.125, 0.250 or 0.500 wt%).

Mass GO paste, m_{GO-P}, was determined by Equation A.6. The calculation considers a weight ratio of 10 wt% GO in the GO paste.

$$m_{GO-P} = \frac{1}{0.1} \cdot m_{GO_{GOslurry}} \quad [g] \quad \text{(A.6)}$$

G slurry

This section presents relevant equations for calculation of the required mass of G in G slurries of 0.125 wt%, 0.250 wt% and 0.500 wt% G compared to mass epikote. G is provided by CealTech AS in a G-Epikote dispersion of 0.6 wt% G. The equations consider mass epikote in the G slurry, $m_{E_{Gslurry}}$, to be equal to mass epikote in the GO slurry, found by Equation A.4. Required mass of acetone, m_s, was further calculated by Equation A.1.

Equation A.7 was used to calculate the required amount of G in the G slurry with appropriate wr_G.

$$m_{G_{Gslurry}} = wr_G \cdot m_{E_{Gslurry}} \quad \text{[g]} \quad \text{(A.7)}$$

Further, the weight ratio of 0.6 wt% G to mass Epikote was used to determine the required mass of G-Epikote dispersion by using Equation A.8.

$$m_{G-E} = \frac{m_{G_{Gslurry}}}{0.006} \quad \text{[g]} \quad \text{(A.8)}$$

The required mass of pure epikote, $m_{Epikote_{pure}}$, was determined by considering the mass of epikote in the G-Epikote dispersion, $m_{E_{G-Epikote}}$,

$$m_{E_{G-E}} = m_{G-E} \cdot (1 - 0.006) \quad \text{[g]} \quad \text{(A.9)}$$

The final mass of pure epikote was then calculated by Equation A.10.

$$m_{E_{pure}} = m_{E_{Gslurry}} - m_{E_{G-E}} \quad \text{[g]} \quad \text{(A.10)}$$

A.3 Preparation of coating batches

The following section will present the calculations necessary for preparation of all coating batches prior to spray coating deposition. One coating batch contains the desired mass of sol/slurry with appropriate volume of curing agent, and equals one coating deposition. The calculations consider a molar ratio of 2:1 epikote to curing agent.

Sol batch

This section determines the appropriate amount of curing agent and E1 and E2 sol for preparation of E1 and E2 batches, respectively. The calculations are done collectively as the same procedure is used for both sols.

Equation A.11 determines the mass of epikote in the epikote sol corresponding to one coating batch, $m_{E_{batch}}$. $m_{sol_{batch}}$ corresponds to mass of epikote sol considered for one coating batch, and equals 0.5 g. mp_E is previously found in Equation A.3.

$$m_{E_{batch}} = mp_E \cdot m_{sol_{batch}} \quad \text{[g]} \quad \text{(A.11)}$$

Further, the number of moles epikote in one batch was found by Equation A.12. The equation considers the molar weight of epikote, Mm_E (see Table A.1).

$$n_{E_{batch}} = \frac{m_{E_{batch}}}{Mm_E} \quad \text{[mol]} \quad \text{(A.12)}$$

The number of moles curing agent, $n_{CA_{batch}}$, was calculated by Equation A.13, considering a molar ratio of curing agent to epikote, mr_{CA}, equal to 0.5.

$$n_{CA_{batch}} = n_{E_{batch}} \cdot mr_{CA_E} \quad \text{[mol]} \quad \text{(A.13)}$$

Finally, the required volume of curing agent for preparation of one coating batch, $V_{CA_{batch}}$, was determined by Equation A.14.

$$V_{CA_{batch}} = \frac{n_{CA_{batch}} \cdot Mm_{CA}}{\rho_{CA} \cdot p_{CA}} \quad \text{[mL]} \quad \text{(A.14)}$$

Mm_{CA} corresponds to the molar weight of the curing agent, ρ_{CA} to its density and p_{CA} to its purity. These values can be found in Table A.1.

G and GO slurry batch

The slurry batches consider the same mass of epikote in each coating batch, $m_{E_{batch}}$, as for the sol batches. Hence, volume curing agent for each slurry batch can be found in Equation A.14.

The mass of G slurry, $m_{G_{slurrybatch}}$, and GO slurry, $m_{GO_{slurrybatch}}$, in one coating batch was found by Equation A.15 and A.16, respectively.

$$m_{G_{slurrybatch}} = m_{E_{batch}} + m_{s_{slurrybatch}} + m_{Gbatch} \quad \text{[g]} \quad \text{(A.15)}$$

$$m_{GO_{slurrybatch}} = m_{E_{batch}} + m_{s_{slurrybatch}} + m_{GO-P} \quad \text{[g]} \quad \text{(A.16)}$$

The mass of solvent in one batch, $m_{s_{slurrybatch}}$, was calculated by Equation A.1, by considering $m_{E_{batch}}$. $m_{G_{batch}}$ corresponds to mass G in one slurry batch, and was found by,

$$m_{G/GO_{batch}} = m_{E_{batch}} \cdot wr_{G/GO} \quad \text{[g]} \quad \text{(A.17)}$$

Equation A.18 determines mass GO paste in one slurry batch, m_{GO-P}, and considers a GO paste of 10 wt% GO.

$$m_{GO-P} = \frac{m_{GO_{batch}}}{0.1} \quad \text{[g]} \quad \text{(A.18)}$$

$m_{GO_{batch}}$ is the mass of GO in one slurry batch, and was calculated from Equation A.17.

B Bioreactor dimension

Figure B.1 shows a drawing of the dimensions of all individual parts of the biofilm reactor used for antifouling experiments. The drawing and the biofilm reactor is produced by NTNU Workshop.

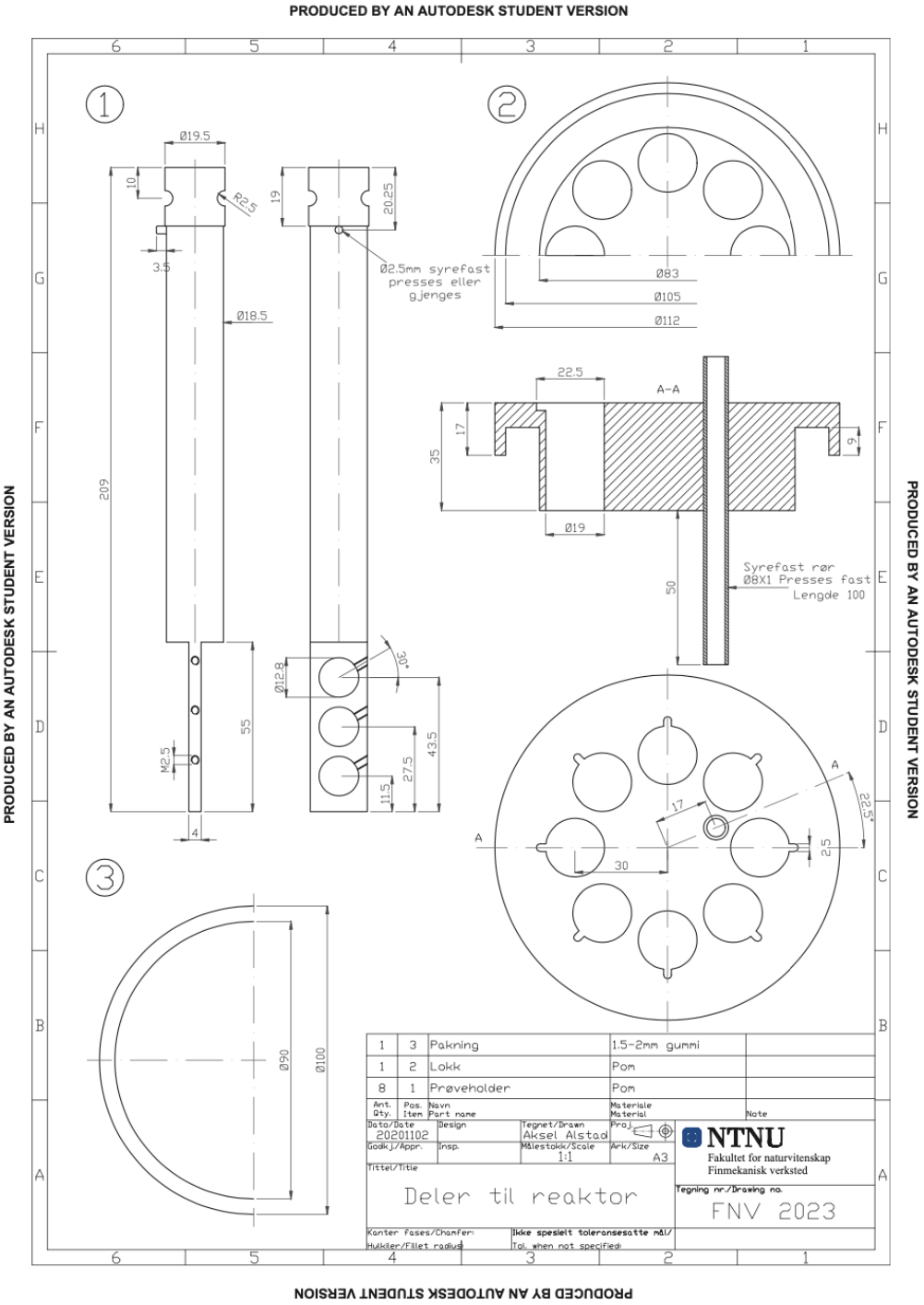

Figure B.1: Dimensions of all individual parts of the biofilm reactor produced by the fine mechanical workshop of NTNU.

C Estimation of area coverage of algae growth by *ImageJ*

The estimation of area coverage of algae growth was performed by image analysis in *ImageJ*. The procedure for estimation of area in *ImageJ* is described below.

1. Open *ImageJ*
2. Open .png file in *ImageJ*: **File** → **Open**
3. Integrate scale bar to *ImageJ*
   (a) Draw a segment over the bar scale of the image
   (b) **Analyze** → **Set scale**
4. Crop image to remove scale bar
5. Duplicate image: Right-click on image and choose **Duplicate**
6. **Image** → **Adjust** → **Color Threshold**
7. Adjust threshold so that only wanted items (diatoms) are marked (see Figure C.1) → Click **Select**
8. Calculate covered area: **Image** → **Analyze** → **Measure**
9. Save results

An example of a color threshold obtained in an image of an E1 coating with marine growth is shown in Figure C.1.

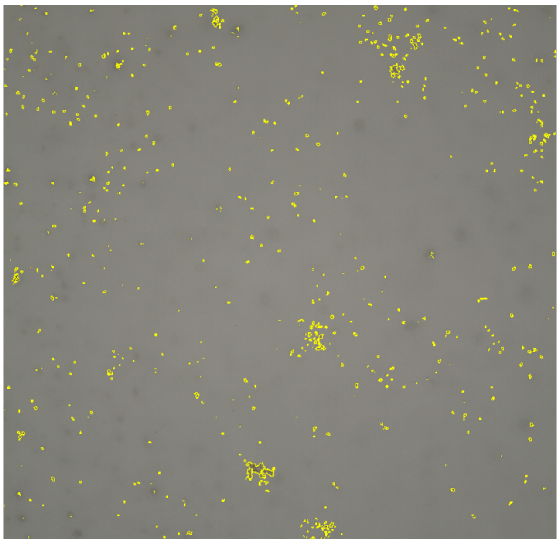

Figure C.1: An illustration of a color threshold obtained in the *ImageJ* software, covering visible marine growth of an E1 coating. The image is captured by an *Alicona Focus SL* optical microscope with a 10X magnification lens.

D Estimation of viscosity

The viscosity was estimated for sols and slurries of type E1, E2, G125, G250, G500, GO125, GO250 and GO500. Linear regression was performed of log shear stress as a function of decreasing log shear rate (from 0-500 s^{-1}) with corresponding error (R^2), as indicated in Figure D.1.

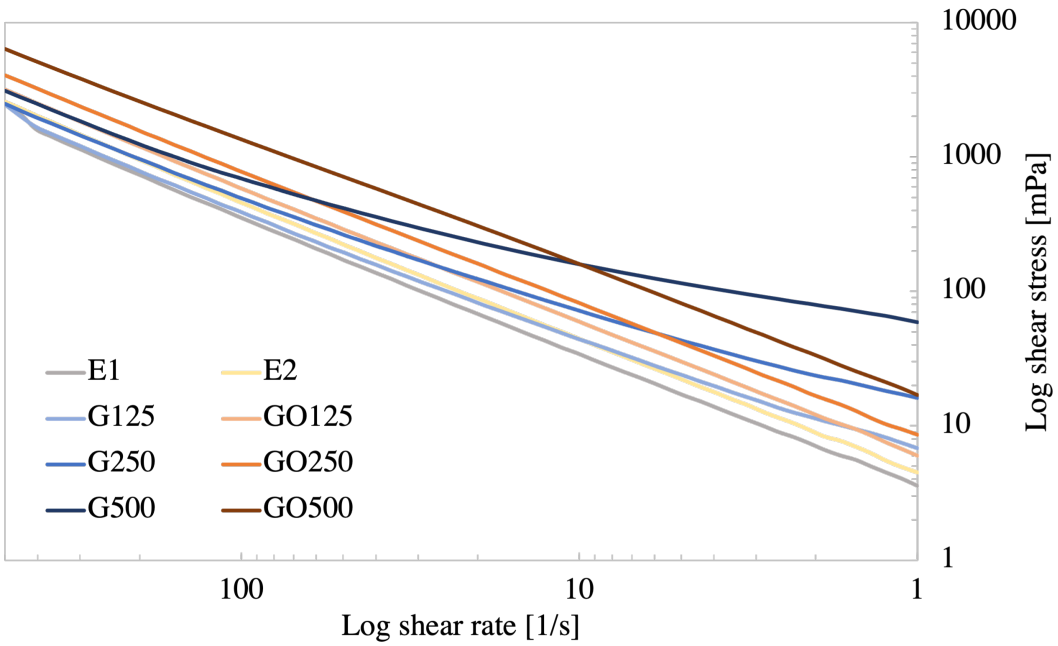

Figure D.1: Estimation of sol and slurry viscosity performed by linear regression. The viscosity of E1 and E2 sol and of G125, G250, G500, GO125, GO250 and GO500 slurries was estimated. E1: pure epoxy with acetone. E2: pure epoxy with acetone and ethanol. GXXX: samples with 0.XXX wt% G. GOXXX: samples with 0.XXX wt% GO. XXX = 125, 250, 500.

E Determination of functional groups

The transmittance spectra of E2 sol and GO slurries obtained three weeks after preparation are presented in Figure E.1. The transmittance spectra obtained for one day, one week and three weeks old sols and slurry are presented for E1 sol and G slurries and for E2 sol and GO slurries in Figure E.2.

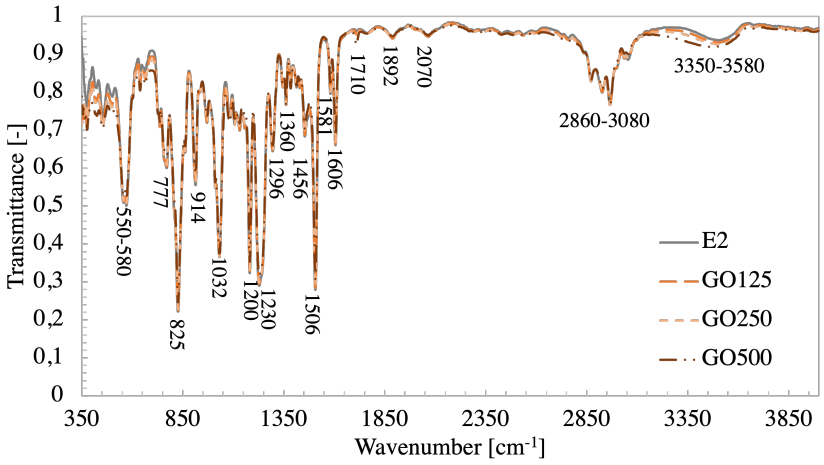

Figure E.1: Transmittance spectra of three weeks old E2 sol and G125, G250 and GO500 slurries. E2: pure epoxy with acetone and ethanol. GOXXX: samples with 0.XXX wt% GO. XXX = 125, 250, 500.

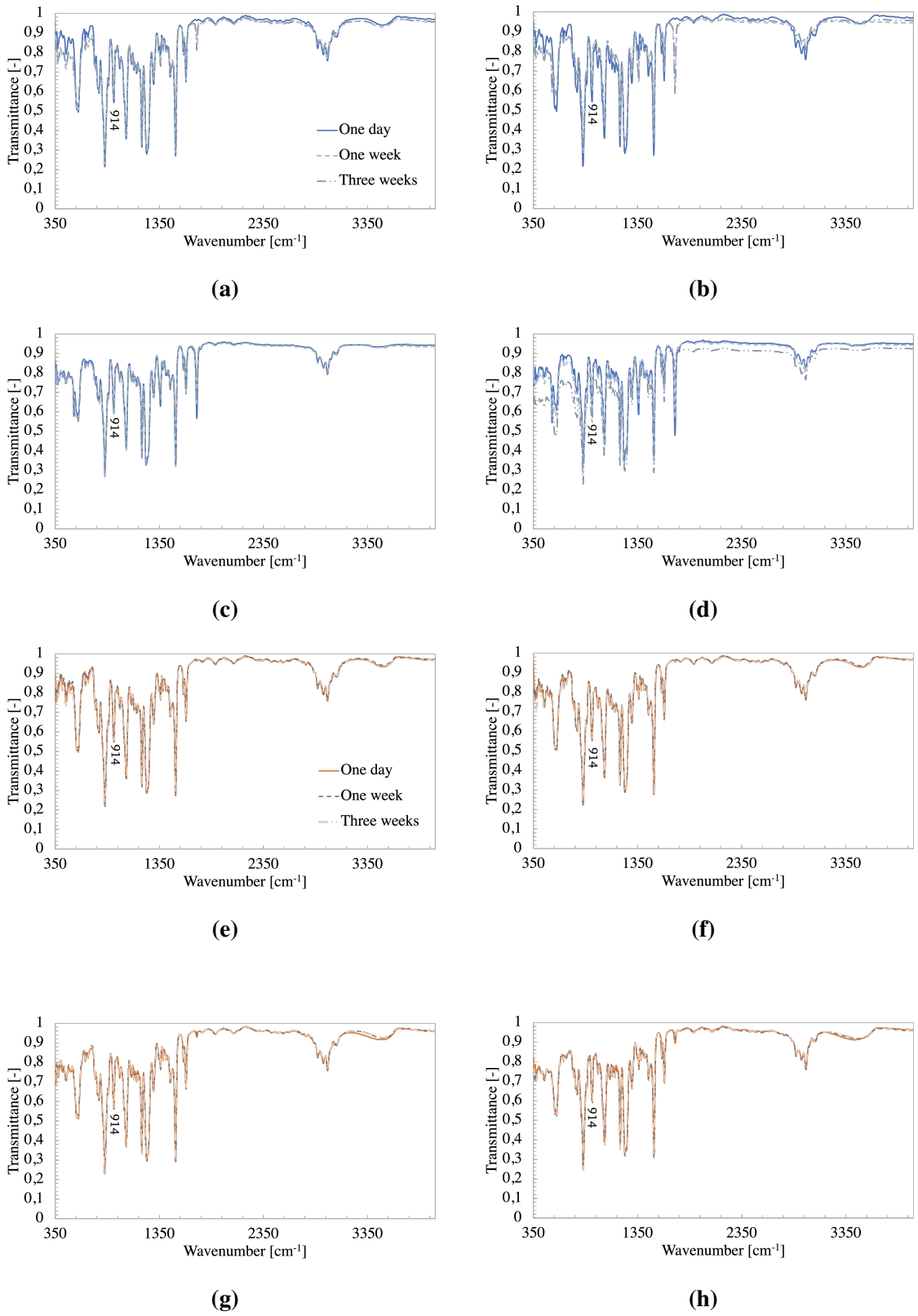

Figure E.2: Transmittance spectra of (a) E1 sol (b) G125, (c) G250 and (d) G500 slurries and (e) E1 sol, (f) GO125, (g) GO250 and (h) GO500 slurries obtained one day, one week and three weeks after preparation. The 914 cm^{-1} vibration from the epoxide functional group is highlighted. E1: pure epoxy with acetone. E2: pure epoxy with acetone and ethanol. GXXX: samples with 0.XXX wt% G. GOXXX: samples with 0.XXX wt% GO. XXX = 125, 250, 500.

F Sheet distribution analysis

Figure F.1 displays the sheet distribution of GO250 and GO500 coatings.

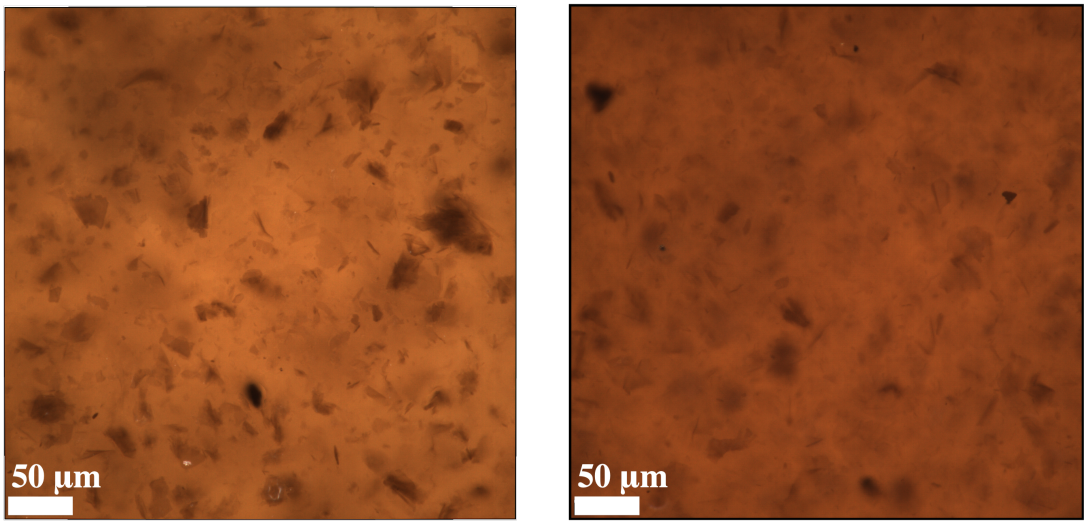

(a) **(b)**

Figure F.1: Sheet distribution of (a) GO250 and (b) GO500 coatings, containing 0.250 wt% and 0.500 wt% GO respectively.

Figure F.2 displays the surface of G250 and G500 coatings.

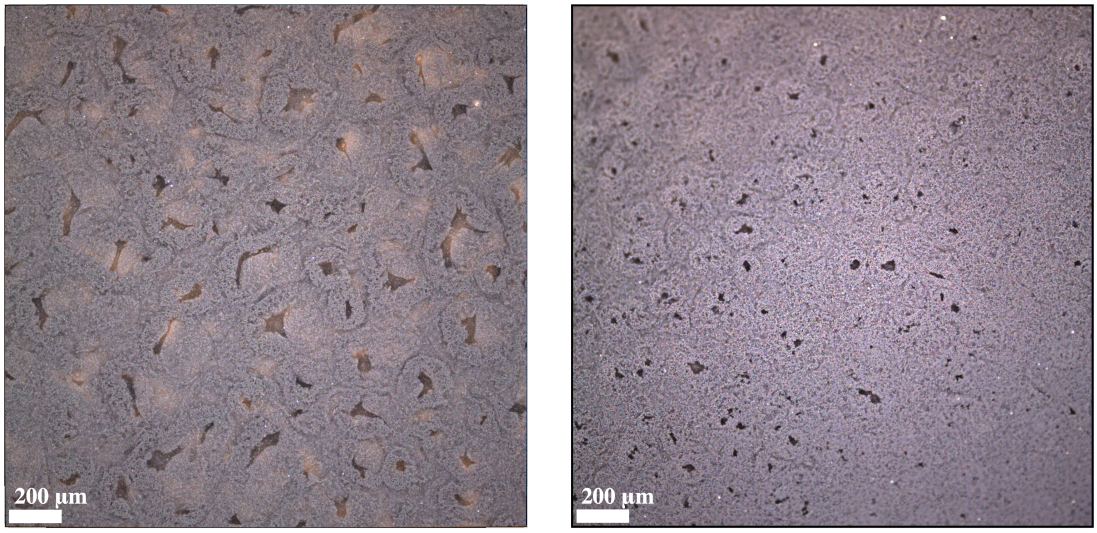

(a) **(b)**

Figure F.2: The surface of (a) G250 an (b) G500 coating containing 0.250 wt% and 0.500 wt% graphene respectively.

G Cross-section analysis of coating thickness

Figure G.1 displays the cross-section of E1 and E2 coatings, showing the measured coating thickness and the respective coating layers.

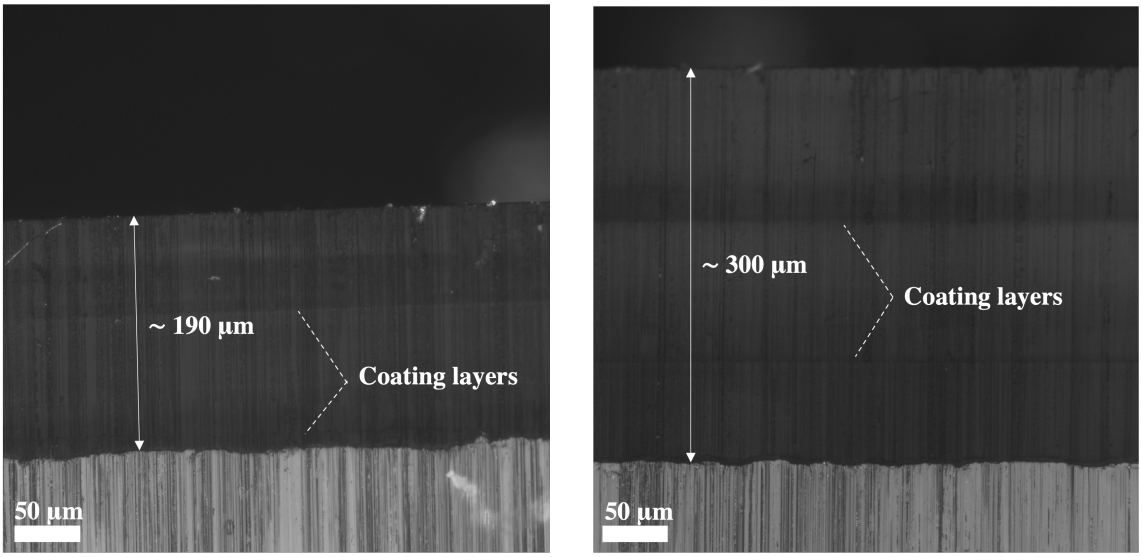

(a) **(b)**

Figure G.1: Cross-section of (a) E1 and (b) E2 coatings prepared on steel substrate, showing the estimated coating thickness and the respective coating layers. E1: pure epoxy with acetone. E2: pure epoxy with acetone and ethanol.

H Estimation of coefficient of friction

Figure H.1 shows the coefficient of friction (COF) as a function of scratch time for all coatings, obtained by performing nanoscratch tests. The graphs were used to establish a time range at which steady state was achieved for the COF. The region at which an approximate steady state was observed ranged from 30 seconds to 50 seconds for all coatings, and this region was used as the basis for calculation of an average COF for each coating.

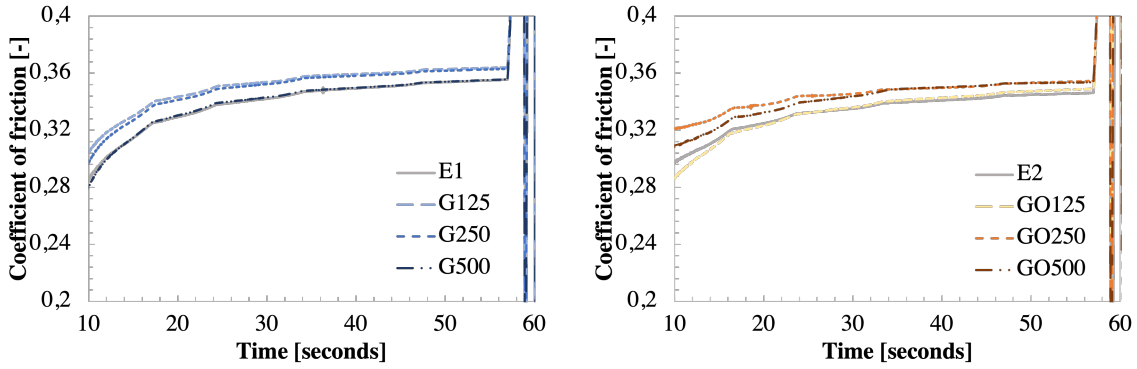

(a) **(b)**

Figure H.1: The coefficient of friction as a function of time measured from a nano scratch test with progressively increasing normal force. The test was performed over a scratch length of 10 μm with maximum normal force of 8000 μN. The figure shows coefficient of friction versus time for (a) E1 and G coatings and (b) E2 and GO coatings. E1: pure epoxy with acetone. E2: pure epoxy with acetone and ethanol. GXXX: samples with 0.XXX wt% G. GOXXX: samples with 0.XXX wt% GO. XXX = 125, 250, 500.

I Additional tables

The following section summarizes specific values obtained from various measurements performed on sols and slurries, on coatings and on uncoated PE and steel substrates. The measurements include viscosity, nanoindentation, wetting properties, surface free energy and quantification of algae growth.

I.1 Viscosity measurement

Table I.1 lists estimated values of viscosity for all prepared sols and slurries with the corresponding coefficient of determination R^2 .

Table I.1: Viscosity of prepared sols and slurries measured one week after preparation. E1: pure epoxy with acetone. E2: pure epoxy with acetone and ethanol. GXXX: samples with 0.XXX wt% G. GOXXX: samples with 0.XXX wt% GO. XXX = 125, 250, 500.

Sample	**Viscosity [mPa · s]**	R^2
E1	4.23	0.98
G125	4.31	0.99
G250	4.83	1.00
G500	5.95	1.00
E2	5.02	1.00
GO125	6.21	1.00
GO250	7.99	1.00
GO500	12.68	1.00

I.2 Nanoindentation measurements

Table I.2 gives an overview of the values of hardness and Young's modulus obtained from nanoindentation measurements performed on all prepared coatings.

Table I.2: Hardness and Young's modulus of all cured coatings prepared on steel substrate. The values are measured by nanoindentation with a Berkovich tip. E1: pure epoxy with acetone. E2: pure epoxy with acetone and ethanol. GXXX: samples with 0.XXX wt% G. GOXXX: samples with 0.XXX wt% GO. XXX = 125, 250, 500.

Sample	Hardness [MPa]	Young's modulus [MPa]
E1	203 ± 5	3876 ± 82
G125	214 ± 8	3632 ± 63
G250	206 ± 3	3791 ± 47
G500	200 ± 3	3836 ± 32
E2	194 ± 5	3870 ± 77
GO125	197 ± 5	3949 ± 97
GO250	212 ± 6	3973 ± 114
GO500	211 ± 5	4150 ± 103

Table I.3 lists the values of average coefficient of friction measured on all prepared coatings by nanoscratch testing.

Table I.3: The average coefficient of friction (COF) for all prepared coatings estimated from the region of steady state, obtained from nanoscratch testing with progressively increasing load. E1: pure epoxy with acetone. E2: pure epoxy with acetone and ethanol. GXXX: samples with 0.XXX wt% G. GOXXX: samples with 0.XXX wt% GO. XXX = 125, 250, 500.

Sample	COF [-]
E1	0.349 ± 0.003
G125	0.359 ± 0.001
G250	0.358 ± 0.003
G500	0.350 ± 0.001
E2	0.341 ± 0.001
GO125	0.343 ± 0.002
GO250	0.350 ± 0.006
GO500	0.350 ± 0.003

I.3 Wettability measurements

Table I.4 lists specific values for contact angles of water and diiodomethane, surface free energy and water contact angle hysteresis measured for all prepared coatings and on uncoated PE and steel substrates.

Table I.4: Contact angles of water and diiodomethane, surface energy and water contact angle hysteresis measured for all prepared coatings and on uncoated polyethylene (PE) and steel substrate. E1: pure epoxy with acetone. E2: pure epoxy with acetone and ethanol. GXXX: samples with 0.XXX wt% G. GOXXX: samples with 0.XXX wt% GO. XXX = 125, 250, 500.

Sample	**Contact angle** [°]		**Surface energy [mN/m]**	**Water contact angle hysteresis** [°]	
	Water	Diiodomethane		45°	90°
E1	60.8 ± 1.0	39.2 ± 0.1	52.5 ± 0.7	8.6 ± 1.0	11.5 ± 1.2
G125	59.6 ± 0.5	32.1 ± 0.1	55.9 ± 0.1	9.0 ± 0.5	12.0 ± 0.5
G250	63.0 ± 0.9	39.0 ± 0.1	50.2 ± 0.1	8.5 ± 0.6	11.4 ± 0.7
G500	64.2 ± 0.8	37.5 ± 0.1	49.9 ± 0.1	8.9 ± 0.8	12.2 ± 1.3
E2	58.2 ± 1.3	41.4 ± 1.3	52.6 ± 0.6	10.5 ± 1.3	14.0 ± 1.2
GO125	60.0 ± 0.5	36.9 ± 0.1	53.5 ± 1.0	9.7 ± 0.2	13.0 ± 1.0
GO250	61.6 ± 1.6	42.9 ± 0.1	50.7 ± 0.8	9.2 ± 0.7	12.4 ± 0.7
GO500	58.4 ± 1.0	35.6 ± 0.1	54.3 ± 0.5	8.1 ± 1.3	11 ± 2
PE	105 ± 2	38.3 ± 0.3	40.0 ± 0.1	7 ± 5	11 ± 2
Steel	69 ± 7	48.6 ± 0.3	44.1± 0.4	8.7 ± 1.4	11.7 ± 0.8

I.4 Quantification of algae growth

Table I.5 lists specific values obtained from performing the direct count method and area estimation method for quantification of algae growth (see 3.8.2) of the biofilm reactor experiments performed with algae culture 1 and algae culture 2. Number of diatoms per mm^2 and estimated area coverage of algae growth measured in percentage with respect to total measured area with corresponding uncertainties are included.

Table I.5: An overview of specific values obtained for quantification of algae growth of the biofilm reactor experiments performed with algae culture 1 and algae culture 2, analyzed on prepared coatings and on reference sample. No. of diatoms per mm^2 and estimated area coverage of algae growth measured in percentage with respect to total measured area are included. E1: pure epoxy with acetone. E2: pure epoxy with acetone and ethanol. GXXX: samples with 0.XXX wt% G. GOXXX: samples with 0.XXX wt% GO. XXX = 125, 250, 500.

Sample	**Algae culture 1**		**Algae culture 2**	
	No. of diatoms per mm^2	Area coverage [%]	No. of diatoms per mm^2	Area coverage [%]
E1	124 ± 16	0.531 ± 0.1	145 ± 7	0.406 ± 0.1
G125	62 ± 10	0.166 ± 0.05	50 ± 3	0.166 ± 0.05
G250	60 ± 5	0.232 ± 0.05	71 ± 36	0.149 ± 0.05
G500	34 ± 3	0.174 ± 0.05	75 ± 9	0.108 ± 0.05
E2	114 ± 6	0.514 ± 0.1	137 ± 23	0.373 ± 0.066
GO125	68 ± 17	0.299 ± 0.1	140 ± 40	0.133 ± 0.05
GO250	61 ± 10	0.166 ± 0.1	105 ± 11	0.133 ± 0.066
GO500	49 ± 3	0.241 ± 0.083	84 ± 24	0.174 ± 0.05
PE	142 ± 6	0.887 ± 0.216	436 ± 49	1.095 ± 0.199

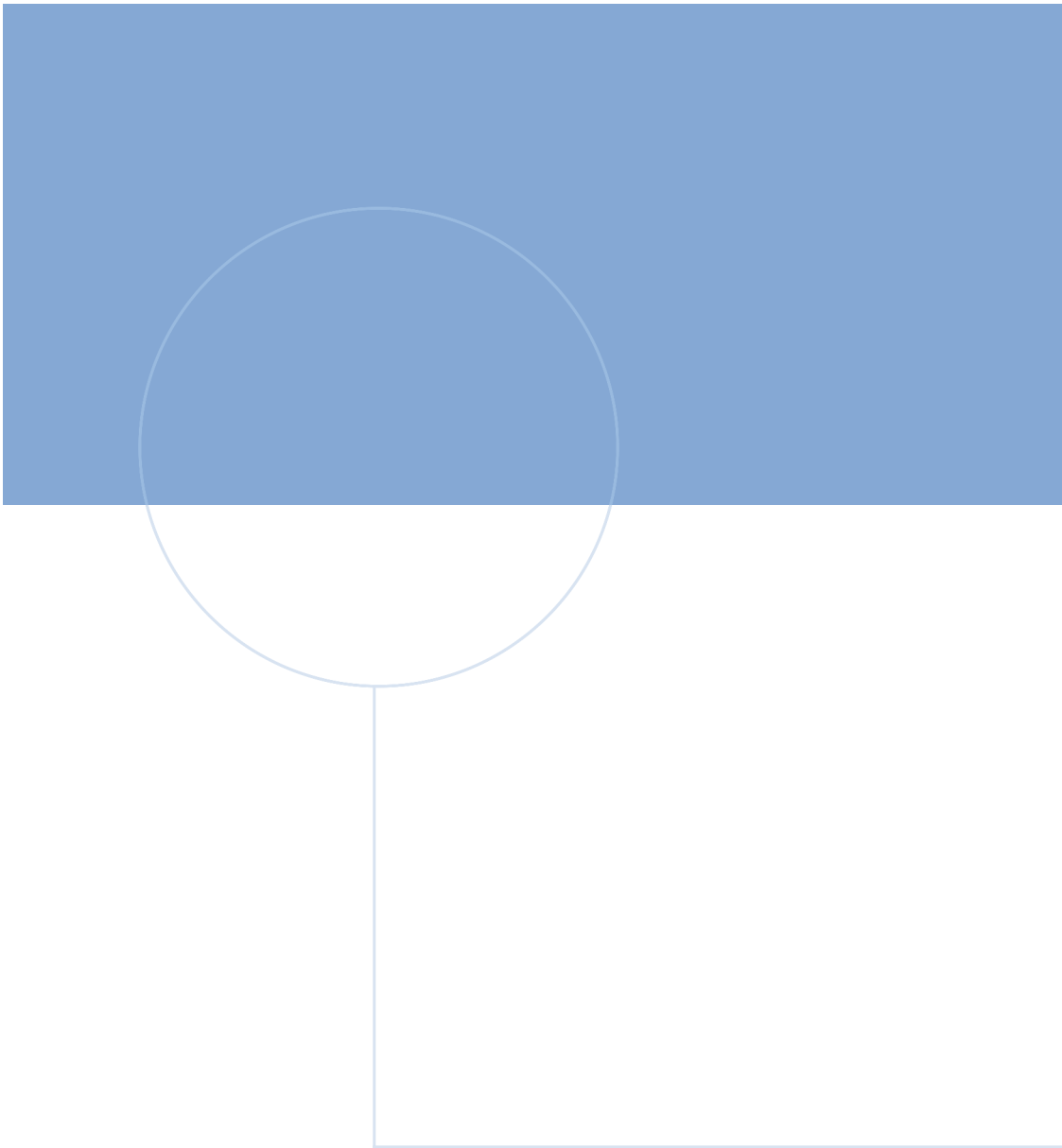

NTNU

Norwegian University of
Science and Technology